Plasmon metal nano-particles as a mechanism to suppress charge recombination and enhance photons capture in thin film polymer solar cell

by

ABDALLAH YOUSIF ADAM AHMED

A thesis submitted in fulfillment of the requirement for the degree of

Doctor of Philosophy in Physics

(Thin Film Polymer Solar cells)

School of Chemistry and Physics

University of KwaZulu-Natal

South Africa

September 2024

Preface

The research discussed in this thesis is carried out in the College of Agriculture, Engineering and Science of the University of Kwa-Zulu Natal, Pietermaritzburg, South Africa, from (January 2020 - December 2020) and (January 2022 - September 2024) by Abdallah Ahmed under the supervision of Professor Genene Tessema Mola.

As the candidate's supervisor, I, Genene Tessema Mola, agree to the submission of this dissertation.

Signed: .....[redacted].....

Date: .....02-04-2025.....

I, Abdallah Ahmed, hereby declare that all the material incorporated in this dissertation are my own original work, except where acknowledgement is made by name or in the form of a reference. The work contained in herein has not been submitted in any form for any degree or diploma to any other institution.

Signed: .....[redacted].....

Date: 30 - 03 - 2025

University of KwaZulu-Natal, March 30, 2025

Abstract

By enhancing the key processes of light absorption, charge transport, and device stability, the thesis contributes to developing sustainable, high-efficiency energy solutions. Moreover, this thesis highlights the incorporation of plasmonic nanoparticles (NPs) into the active layers of organic thin film solar cells to enhance their performance. Especially, the study focuses on the addition of the plasmonic silver magnesium (Ag/Mg) NPs, and nickel-silver (Ni/Ag) nanoclusters into the active layer of Poly(3-hexylthiophene-2,5-diyl)(P3HT):[6,6] phenyl-C61-butyric acid methyl ester ($PC_{61}BM$) polymer blend. Furthermore, we hvae investigated the incorporation of cobalt sulfide (CoS) NPs into the Poly [[4,8-bis[(2-ethylhexyl)oxy]benzo[1,2-b:4,5-b']dithiophene-2,6-diyl][3-fluoro-2-[(2-ethylhexyl)carbonyl]thieno[3,4-b]thiophenediyl]] (PTB7):[6,6]-Phenyl-C71-butyric acid methyl ester ($PC_{71}BM$) active layer. The introduction of plasmonic NPs is aimed at improving light absorption, charge carrier generation, charge recombination, and overall efficiency of thin film polymer solar cells. The occurrence of localized surface plasmonic resonance (LSPR) due to the inclusion of plasmon NPs in photo-active layer positively influenced the optical and electrical properties of the medium that leads to improved light harvesting. Through a series of experimental studies, the thesis demonstrates that the inclusion of Ag/Mg, and Ni/Ag NPs in P3HT:$PC_{61}BM$ leads to significant improvements in device performance. Each NPs system is characterized in terms of its synthesis, incorporation methods, and the resulting morphological and optoelectronic properties of the active layer. Moreover, the incorporation of CoS NPs into the PTB7:$PC_{71}BM$ blend is investigated, highlighting the positive effects of combining these materials. The results demonstrated an enhancement in both the absorption spectrum and the charge transport properties, contributing to an overall increase in device performance as the power conversion efficiency (PCE) of the optimized device was improved by 37% compared to the reference solar cell device. The research outcomes contribute to the understanding of plasmonic-enhanced organic thin film solar cells and offer new possibilities for the material combinations and mechanisms that influence performance improvements. The results presented in this thesis are supported by three peer-reviewed publications. Which details the experimental approaches, analyses, and conclusions drawn from the study. Generally, this work demonstrates the potential of plasmonic NPs and quantum confinement effect to advance

the efficiency and viability of organic thin film technologies, paving the way for future developments in sustainable energy solutions.

Dedication

This work is dedicated to the soul of my mother for her effective contributions to my academic knowledge.

Declaration 1 - Plagiarism

I, **Abdallah Ahmed**, declare that;

1. The research reported in this thesis, except where otherwise indicated, is my original research.
2. This thesis has not been submitted for any degree or examination at any other university.
3. This thesis does not contain other persons' data, pictures, graphs or other information, unless specifically acknowledged as being sourced from other persons.
4. This thesis does not contain other persons' writing, unless specifically acknowledged as being sourced from other researchers. Where other written sources have been quoted, then:
   (a) Their words have been re-written but the general information attributed to them has been referenced,
   (b) Where their exact words have been used, then their writing has been placed in italics and inside quotation marks, and referenced.
5. This thesis does not contain text, graphics or tables copied and pasted from the Internet, unless specifically acknowledged, and the source being detailed in the thesis and in the references sections.

Signed: .....  .....

Date: 30 - 03 - 2025 .....

Declaration 2 - Publications

I hereby declare that the contents of this thesis and each paper are detailed below.

1. **Ahmed, A. Y. A.**, Ike, J. N., Hamed, M. S. G. and Mola, G. T. Silver decorated magnesium doped photoactive layer for improved collection of photo-generated current in polymer solar cell, *Journal of Applied polymer Science*, (2023) *140*, e53697. DOI: 10.1002/app.53697.
2. **Ahmed, A. Y. A.**, Hamed, M. S. G., Ike, J. N., and Mola, G. T. Nickel-doped silver nanoclusters as a mechanism to capture photons. *Journal of Materials Science*, (2024) 1-14. doi.org/10.1007/s10853-024-09690-6.
3. **Ahmed, A. Y. A.**, Ogundele, A. K., Hamed, M. S.G., Tegegne, N. A., Kumar, A., Sharma G., and Mola G. T. Application of cobalt-sulfide to suppress charge recombinations in polymer solar. *Journal of Material Science in Semiconductor Processing*, (2024) **185**, 108917. .

Publication has not been included in the thesis

1. Mola, G. T., **Ahmed, A. Y. A.**, Ike, J. N., Liu, M., Hamed, M. S. G., and Zhang, Y. Engineering Non-fullerene Acceptors as a Mechanism to Control Film Morphology and Energy Loss in Organic Solar Cells. *Energy & Fuel*, (2022), **36**, 4691-4707. doi.org/10.1021/acs.energyfuels.2c00462.

2. Hamed, M. S. G., **Ahmed, A. Y. A.**, and Mola, G. T. Suppressing charge recombination in disordered polymers blend medium. *Journal of Physics D: Applied Physics*, (2023) **56**, 405101, 405101. doi.org/10.1088/1361 6463/ace1ff.

Signed: ..... 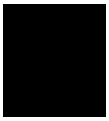 .....

Acknowledgements

This Ph.D. thesis would not have been possible without the support and encouragement of many individuals. and I am deeply grateful to everyone who has supported me along the way.

My heartfelt thanks go to my supervisor, Professor Genene Tessema Mola, whose guidance and encouragement have been invaluable. His visions and advice have directed me through every stage of this research.

Special thanks to my family including My wife Safia Yahya, my son Refat Adam, and my daughter Retal Adam for their love and sacrifices. To the soul of my mother, my father, brothers, sisters, and friends. Their faith in me has been my greatest source of strength.

I also want to acknowledge the support of my friends and colleagues at the University of KwaZulu Natal, Pietermaritzburg Campus, School of Chemistry and Physics. The interesting discussions and collaborative environment have been essential to my academic growth. Special thanks to Dr. Mohammed S G Hamad, Dr. Saheed Oseni, Dr. Michael Adedeji, Dr. Mpilo Wiseman Dlamini, Dr. Xolani Mbuyise, Mr. Abiodun Ogundele, and Ncedo Jili. for their technical support and friendship.

Lastly, I acknowledge the financial support provided by the National Research Foundation (NRF), the Ministry of Higher Education and Scientific Research Sudan for their financial assistance, and Elgeneina University, Sudan for providing me with this opportunity to study for this doctoral degree.

Thank you all for your support and encouragement.

List of Abbreviations

NPs	Nanoparticles
P3HT	Poly(3-hexylthiophene-2,5-diyl)
$PC_{61}BM$	[6,6] phenyl-C61-butyric acid methyl ester
PTB7	Poly(thieno[3,4-b]thiophene benzodithiophene)
$PC_{71}BM$	[6,6]-Phenyl-C71-butyric acid methyl ester
LSPR	Localized surface plasmonic resonance
PCE	Power conversion efficiency
PV	Photovoltaic
CIS	Copper indium diselenide
CdTe	Cadmium telluride
GaAs	Gallium arsenide
LUMO	Lowest unoccupied molecular orbital
HOMO	Highest occupied molecular orbital
BHJ	Bulkheterojunction
SPR	Surface plasmonic resonance
OSCs	Organic solar cells
D	Donor
A	Acceptor
HRTEM	High-resolution transmission electron microscopy
HRSEM	High-resolution scanning electron microscopy
XRD	X-ray diffraction
EDX	Energy-dispersive X-rays spectroscopy
FTIR	Fourier Transform Infra-red Spectroscopy
Ag	Silver
Mg	Magnesium

Cu	Copper
Ni	Nickel
NCs	Nanoclusters
Ag.Mg	Silver magnesium
Cu/Ni/Ag	Copper/Nickel/Silver
Ni/Ag	Nickel-doped Silver
OPV	Organic photovoltaic
ITO	Indium Tin Oxide
CoS	Cobalt Sulfide
HTL	Hole transport layer
ETL	Electron transport layer
PEDOT:PSS	poly(3,4-ethylene dioxythiophene)polystyrene sulfonate
MoO3	Molybdenum trioxide
PSCs	Polymer solar cells
MEH-PPV	poly(2-methoxy-5-(2'-ethyl-hexyloxy)-1,4-phenylenevinylene)
FCs	Free charges
SCLC	Space charge limited current
V_{oc}	Open circuit voltage
ZnO	Zinc oxide
LiF	Lithium fluoride
CTSs	Charge transfer states
J-V	Current-Voltage
J_{sc}	Short circuit current density
P_{MPP}	Maximum power point
FF	Fill Factor
AM	Air Mass
Au	Gold
Cu	Copper
Ag	Silver
MNP	Metal nanoparticle
LEFE	Localized electromagnetic field enhancement
PIRET	Plasmon-induced resonance energy transfer
BMNPs	Bimetallic nanoparticles
TFOSCs	Thin-filmorganicsolarcell

CB	Conduction Band
GR	Geminate recombination
NGR	Non-geminate recombination
SCT	Singlet charge transfer
TCTS	Triplet charge transfer state
R_{sh}	Shunt resistance
R_s	Series resistance
TFPCs	Thin film polymer solar cells
E_g	Energy band gap
E_{CT}	Energy of charge transfer state
E_{LOSS}	Energy loss
SEM	Scanning electron microscopy
TEM	Transmission electron microscopy
UV–Vis	Ultraviolet-visible
FWHM	Full width at half maximum
TMCs	Transition metal chalcogenides
PQ	Plasmonic-Quantum Dots

Contents

List of Figures

List of Tables

Chapter 1

The Need For Transformation To Sustainable Energy

1.1 Introduction

The rapidly increasing global population and prospering civilizations have given rise to an exponential increase on the energy demand. However, despite their unsustainable nature, severe environmental degradation, and adverse effects on health, fossil fuels remain currently as the dominant energy source today. The massive amounts of greenhouse gases, including methane, carbon dioxide, and nitrous oxide released by the combustion of fossil fuels are expected to grow in the future due to fast urbanization and industrialization globally. The present and predictable levels of greenhouse gases present various consequences, including extreme weather patterns, growing health issues, rising sea levels, and environmental disruptions. These climate changes and health hazards from fossil fuel consumption pose imminent threats to human existence through their disruption of the nine planetary boundaries [1]. Furthermore, the challenges posed by energy production and consumption extend beyond global warming to encompass a broader spectrum of environmental concerns. These include air pollution, acid rain, ozone depletion, deforestation, and the release of radioactive substances. Addressing these issues simultaneously is crucial for sustainable energy in the future that minimizes environmental harm. In this context, sufficient evidence suggests that continued degradation of the environment will have reflective and unfavorable consequences for our collective future [2]. Therefore, transitioning to renewable energy in all technological aspects of modern living, buildings, industrial, and power sectors is one of the possible solutions to mitigate climate change and ensure a sustainable future. This can be achieved by focusing on a strategy that permits the deployment of a mixed suite of such as solar, wind, hydro, geothermal, and biomass, which are clean, abundant, and renewable, offering a promising solution to

our global energy crisis. In this concern, previous studies have shown that we can use different resources, technologies, and policies to improve energy access, air quality, and energy security, and avoid climate change [3].

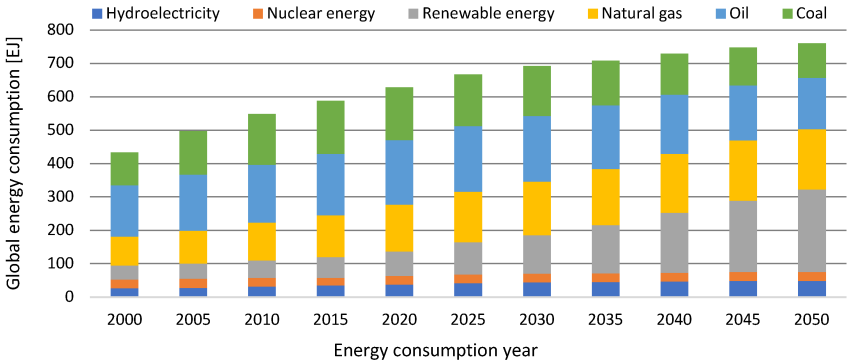

Figure 1.1: The global energy consumption and the need for renewable energy by 2050 [6].

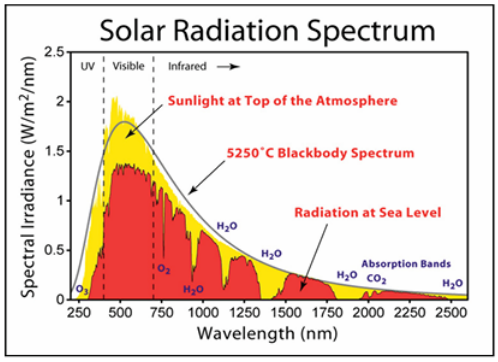

Figure 1.2: Illustrate the amount of solar irradiation at the earth's surface and atmosphere [1].

Figure. 1.1. Displays the current level of renewable energy consumption among other resources such as hydroelectricity, nuclear, natural gas, oil, and coal which still require further growth. Renewable energies are sources of energy that are constantly replaced by nature and come from the sun, either directly (solar thermal, photochemical, and photovoltaic), indirectly (wind, hydropower, and biomass), or from other natural processes (geothermal and tidal) [4]. As shown in Figure 1.2, One of the most available renewable energy resource today today is solar energy, which includes solar photovoltaic, grid-connected, solar photovoltaic isolated, and thermal solar energy. This is based on the fact that the sun emits 3.8 x 10^{23} kW per second which is greater than the annual global energy consumption of 1.8 x 10^{14} kW. The solar energy is clean and free of emissions, which makes it an essential solution to the climate change crisis. Solar energy has been effectively exploited as a method of light and heat since early human history. For example, in the 5th century B.C., the ancient Greeks designed their homes to capture the sun's heat during the winter. Later, the Romans improved solar architecture by covering south-facing windows with clear materials such as mica or glass, preventing the escape of

solar heat captured during the day. Despite efforts of harnessing solar energy for thermal applications, the brain child on the conversion of solar energy to electricity was due to Edmund Becquerel who in 1839 discovered the photovoltaic effect while experimenting with an electrolytic cell made up of two metal electrodes. Becquerel found that certain materials would produce small amounts of electric current when exposed to light [7]. Using the solar energy through photovoltaic (PV) technologies is considered one of the most promising approaches for generating clean and sustainable electricity. The PV effect was first studied in solids, such as selenium in the 1870s. In the 1880s, selenium PV cells were built and produced 1%-2% efficiency in converting light to electricity. Selenium converts light in the visible part of the sun's spectrum; for this reason, it was quickly adopted by the then-emerging field of photography for photometric (light-measuring) devices [9, 8]. Nowadays the developments in solar energy conversion systems have led to the conversion of sunlight directly to the electricity by using simple design and efficient handling devices. These devices can be employed in various applications globally to generate electricity for homes, businesses, and utilities, in addition to the power of electric vehicles and other transportation systems. The working principle of PV devices is based on photoabsorption in semiconductor materials to generate electron hole pairs (excitons) at the conduction - valence band edges. The electron - hole pairs can be strongly (frenkel excitons) and weakly (Wannier excitons) bound depending on the optical properties of the semiconductor. Since the excitons determine the generation rate, the can be dissociated to form electrons and holes which are collected at the electrode to generate current or voltage and used to generate electricity [10, 11]. Based on material composition solar cell technology generally is classified into three generations. The first generation consists of conventional crystalline silicon-based solar cells, including monocrystalline and polycrystalline silicon. The second generation includes thin-film solar cells such as amorphous silicon, cadmium telluride, and copper indium gallium selenide. The third generation includes perovskite solar cells, organic photovoltaics (OPV), quantum dot solar cells, dye-sensitized solar cells (DSSC). The crystalline silicon-based solar cells, are still dominate the market due to their high efficiency and stability despite high manufacturing costs [12, 13]. The efficiency of a PV device is generally determined by the ability of the device to absorb photons and convert them into electricity. The developments in the area of inorganic semiconductor-based solar cell technology are based on the fact that the valence and conduction bands of the inorganic semiconductor materials are responsible for electron-hole generation and transformation within the solar cell device. For example, the classical way of PV devices is to convert light directly into electric current and voltage through the forming of a diode between the junction of two regions in an inorganic semiconductor, one doped as n-type and the other as a p-type. The n-type has one more electron than all their neighbors making it a donor (D), while the p-type dopants have one less electron and will accept electrons. When electrons migrate from the n-type region to the p-type region, and conversely,

holes move from the p-type to the n-type region, a depletion region is formed. This region creates a built-in electric field that influences charge carrier movement within the junction. As soon as a photon with enough energy strikes an electron in a semiconducting material it is excited into the conduction band (CB) without the need for a change in momentum (direct direct band gap semiconductor), while for indirect transition, this process requires both a photon and a phonon for electron excitation. The electron and hole pairs through the p-n semiconductor junction accelerate away from each other by the built-in electric field resulting in current output [14]. Several different semiconductor materials have been employed for the photon-electricity conversion process. Among these materials, silicon is the most successfully used semiconductor, which has many forms such as single-crystalline, multi-crystalline, and amorphous silicon. In addition to silicon, later polycrystalline thin films such as Copper indium diselenide (CIS), Cadmium telluride (CdTe), and and gallium arsenide (GaAs) also strongly contributed to the development of PV technology. [15]. Recently organic PV technology or polymer thin film solar cells, which use carbon-based materials such as small molecules, dendrimers, and polymers to convert solar energy into electricity have attracted research attention to substitute the traditional high-cost inorganic-based solar cells [16]. These electronic dissimilar organic materials consist of an electron donating polymer and an electron accepting molecule embedded together to form the interconnected bulk heterojunction (BHJ). Photon absorption occurs in the high ionization energy donor molecule through the electron transition between the highest occupied molecular orbital (HOMO) and the lowest unoccupied molecular orbital (LUMO). This leads to the formation of the Frenkel exciton which needs to diffuse to the donor to acceptor interface for it to be dissociated into separate electric charge carriers. The essential advantage of employing organic materials in thin film solar cells is their flexibility in modifying molecular properties to specific applications. Moreover, by manipulating factors like the length and functional groups of these polymers, several parameters such as molecular mass, bandgap, and the charge-generating rate can be finely adjusted [17, 18]. As shown in Figure. 1.3. The electronic formation of organic semiconductor polymers depends upon the presence of conjugated π-electrons, where their structure design looks like a sequence of alternating single and double carbon-carbon bonds. Single bonds are identified as σ-bonds and are associated with localized electrons, while double bonds contain both a σ-bond and a π-bond. The π-electrons exhibit heightened mobility compared to their σ-electron counterparts, facilitating their transition across carbon atoms through the related overlap of π orbitals along the conjugated pathway. This overlap results in the delocalization of wave functions throughout the conjugated structure. The π-bands within this system can either be empty, referred to as the LUMO, or filled with electrons, labeled as the HOMO. This π-electron arrangement summarizes the fundamental electronic characteristics of the polymer materials, including light absorption and emission, as well as charge generation and transport [19].

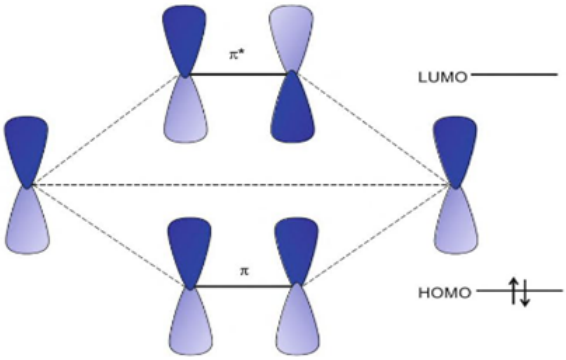

Figure 1.3: Bonding and antibonding orbitals of the conjugated polymers [20].

Due to the non-crystalline nature of organic polymer materials, there are no specific bands for electrons and holes, as well as there, is no particular electric field similar to that for inorganic materials. As a result, when incident light generates an excited electron, a quick recombination with its hole occurs unless pre-emptive separation takes place. To address this challenge, the employment of a double-material strategy, with one favoring electrons and the other holes is usually introduced. Then the electrons/holes pairs efficiently dissociate in separate materials, before their diffusion alongside respective concentration gradients [21]. Many types of electron donor (D) and acceptor (A) blends have been studied to bring photon-electricity conversion requirements and they can be classified into three major types: molecular, polymer, and hybrid. Maximizing the surface area to volume ratio of the interface between the two materials becomes essential for optimal charge carrier separation. This can be achieved through the fabrication of ultra-thin films of the blending of materials which form what a called bulk heterojunction (BHJ). Since the first development of BHJ design by Pochettino in 1906 subsequently, remarkable research efforts have been efficiently made to advance semiconducting polymers, simultaneously improving the performance of various organic electronic devices such as organic solar cells (OSCs), organic light-emitting diodes, and layered memory structures [4]. Due to the restrictive constraint set by the short exciton diffusion length and also the loss in the photoabsorption necessitates the use of plasmonic nanoparticles. The synthesizing and performing metal/semiconductor NPs into the active layer/buffer layer of BHJ thin film organic solar cells to improve the performance of the devices has attracted research interest due to the promising properties of NPs technology in terms of light absorption. Among these NPs, surface plasmonic resonance (SPR) and localized surface plasmonic resonance (LSPR) based NPs have been the most effectively employed in polymer thin-film solar cells. LSPRs arise from the collective oscillations of free electrons confined locally by metal nanostructures. Where, their effect stands out from the localized enhancement of the electromagnetic field due to strong resonance effects, resulting in efficient light trapping [3]. Moreover, when a nanostructured metal is exposed to light, the

electromagnetic field of the incident light applies a potential to the conduction electrons of the metal nanoparticle (MNP) forcing them to move near the NPs surface in the form of the electron cloud. However, as the electrons are still confined inside the NP, the negatively charged electrons cloud concentrate on one side, while positively charged holes accumulate on the opposite side of the electrons leading to the generation of a new electric field inside the metal nanostructure. but the electromagnetic field is frequency dependent, oscillations may arise from this attribute [4].

1.2 Problem Statements

The justification for the exploration and promotion of solar energy and PV technology lies in the urgent need to address the environmental challenges influenced by conventional energy sources. The abundance and clean nature of solar energy, coupled with the developing potentials of PV systems is a key factor in achieving a sustainable and strong energy future. As such, investing in research and development in this field is not only essential for mitigating climate change but also provides a holistic approach to environmental conservation and energy security. In this concern, thin-film organic solar cells technology is preferred choice for their optical and electronic flexibility, lightweight nature, low-cost and facile device fabrication making them best for photovoltaics, and portable devices. The efficiency of OPV cells can be enhanced by optimizing the bulk heterojunction structure or by utilizing the near-field and far-field effects of SPR to improve light absorption and charge carrier dynamics.

1.3 Aim of the Thesis

This study is primarily focused on improving the PCE of organic solar cells using the SPR effect. This improvement will be achieved by strategically incorporating optimized metal NPs at the active layer within the device structure. These NPs will be synthesized using a direct wet chemical method to produce plasmonic metal NPs, and their integration into solar cells will follow a cost-effective approach. The principal goal is to develop more environmentally stable devices while maintaining a low-cost fabrication process.

1.4 Objectives of The Thesis

A. Synthesis of plasmonic metal NPs in the form of Ag/Mg bimetallic NPs and incorporate them into the active layer of P3HT:$PC_{61}BM$ solar.

B. Synthesis of plasmonic metal NPs in the form of Ni/Ag clusters and incorporation into the active layer of P3HT:$PC_{61}BM$ solar.

C. Synthesis of Cobalt sulfide NPs and incorporation them into the active layer of PTB7:$PC_{71}BM$ solar cells.

D. Enhancing the efficiency of polymer solar cells by optimizing the solar absorber through the strategic incorporation of plasmonic metal and metal sulfide quantum dot NPs.

E. Employing possible characterization techniques, such as High-resolution transmission electron microscopy (HRTEM), High-resolution scanning electron microscopy (HRSEM), X-ray diffraction (XRD), Energy-dispersive X-ray spectroscopy (EDX), and Fourier Transform Infrared Spectroscopy (FTIR) to analyze the optical and morphological properties of the synthesized NPs.

1.5 Outline of The Thesis

This thesis investigates the impact of plasmonic metal NPs on the performance of the various functional layers of polymer solar cells. Several polymers blend solar absorber media such as P3HT:$PC_{61}BM$ and PTB7:$PC_{71}BM$ were used in the investigations. The thesis is composed of 7 chapters, highlighting the synthesis process, characterization, and incorporation of plasmon metal NPs into thin-film solar cells, thereby advancing device performance through improved light absorption. Chapter 1, discusses with a general overview of solar energy, addressing its role in reducing global energy crises and environmental issues. Beyond outlining the motivations for the research, this chapter covers problem statements, the aim of the study, objectives, and concludes with a detailed description of the thesis outline. Chapter 2, displays the literature review, providing a brief definitions for the fundamental concepts polymer thin film solar cells. Theses concepts include materials, device structure, working mechanisms, charge recombination, and solar cells parameters. Chapter 3 covers a detailed discussion of the concept of plasmonic, localized surface plasmonic resonance, and the possible mechanisms of the energy transfer from plasmonic metal NPs into thin films organic solar cells. This chapter also offers a brief description about the transitional metal chalcogenides (TMCs), and the quantum confinement effect in TMC NPs. Chapter 4, include bimetallic nano-composites of Silver magnesium (Ag/Mg) article covering the synthesis, characterization as well as a detailed discussion. The incorporation of the plasmonic Ag/Mg NP into the active layer of P3HT:$PC_{61}BM$ thin-film organic solar cells has enhanced the optical absorption, leading to improved efficiency through near-field enhancement plasmon mechanisms. Chapter 5, introduces Nickel-doped Silver nanoclusters (Ni/Ag) (NCs), which were successfully synthesized and characterized using high-resolution scanning and electron microscopy (HRSEM and HRTEM). These NCs are incorporated into the photo-active layer of conventional thin-film organic solar cells, demonstrating enhanced device performance of various solar cell parameters. Chapter 6 focuses on newly

synthesized cobalt sulfide core-shell NPs (CoS) used in the solar absorber medium of PTB7:$PC_{71}BM$. The CoS NPs doped in an inverted structure of thin-film organic solar cells enhanced photon harvesting and significantly improved PCE due to the quantum confinement effect. As a final point, chapter 7 is the conclusion of the thesis discussing the out come of the investigations.

References

[1] Olabi, A. G., & Abdelkareem, M. A. Renewable energy and climate change. *Renewable and Sustainable Energy Reviews*, 2022, **158**, 112111.

[2] Dincer, I. Renewable energy and sustainable development: a crucial review. *Renewable and Sustainable Energy Reviews*, 2000, **4**(2), 157-175.

[3] Gielen, D., Boshell, F., Saygin, D., Bazilian, M. D., Wagner, N., & Gorini, R. The role of renewable energy in the global energy transformation. *Energy Strategy Reviews*, 2019, **24**, 38-50.

[4] Ellabban, O., Abu-Rub, H., & Blaabjerg, F. Renewable energy resources: Current status, future prospects and their enabling technology. *Renewable and Sustainable Energy Reviews*, 2014, **39**, 748-764.

[5] Ranabhat, K., Patrikeev, L., Revina, A. A., Andrianov, K., Lapshinsky, V., & Sofronova, E. An introduction to solar cell technology. *Journal of Applied Engineering Science*, 2016, **14**(4).

[6] Kalak, T. Potential use of industrial biomass waste as a sustainable energy source in the future. *Energies*, 2023, **16**(4), 1783.

[7] Jones, G. G., & Bouamane, L. "Power from Sunshine": A Business History of Solar Energy. *Harvard Business School Working Paper Series*, 2012.

[8] Kannan, N., & Vakeesan, D. Solar energy for future world: A review. *Renewable and Sustainable Energy Reviews*, 2016, **62**, 1092-1105.

[9] Hersch, P., & Zweibel, K. Basic photovoltaic principles and methods. *Solar Energy Research Inst. (SERI), Golden, CO (United States)*, 1982.

[10] Green, M. A. Photovoltaic principles. *Physica E: Low-Dimensional Systems and Nanostructures*, 2002, **14**(1-2), 11-17.

[11] Razykov, T. M., Ferekides, C. S., Morel, D., Stefanakos, E., Ullal, H. S., & Upadhyaya, H. M. Solar photovoltaic electricity: Current status and future prospects. *Solar Energy*, 2011, **85**(8), 1580-1608.

[12] Yan, D., Cuevas, A., Stuckelberger, J., Wang, E.C., Phang, S.P., Kho, T.C., Michel, J.I., Macdonald, D. and Bullock, J., 2023. Silicon solar cells with passivating contacts: Classification and performance. Progress in Photovoltaics: Research and Applications, *31(4)*, pp.310-326.

[13] Płaczek-Popko, E., 2017. Top PV market solar cells 2016. Opto-Electronics Review, *25(2)*, pp.55-64.

[14] Rhaman, M. M., & Matin, M. A. Organic Solar Cells: Historical developments and challenges. In *2015 International Conference on Advances in Electrical Engineering (ICAEE)*, IEEE, 2015, pp 26-29.

[15] Mohan, R., & Paulose, R. Brief review on copper indium gallium diselenide (CIGS) solar cells. *Photoenergy and Thin Film Materials*, 2019, 157-192.

[16] Brabec, C. J., Sariciftci, N. S., & Hummelen, J. C. Plastic solar cells. *Advanced Functional Materials*, 2001, **11**(1), 15-26.

[17] Abdulrazzaq, O. A., Saini, V., Bourdo, S., Dervishi, E., & Biris, A. S. Organic solar cells: a review of materials, limitations, and possibilities for improvement. *Particulate Science and Technology*, 2013, **31**(5), 427-442.

[18] Thelakkat, M. Star-shaped, dendrimeric and polymeric triarylamines as photoconductors and hole transport materials for electro-optical applications. *Macromolecular Materials and Engineering*, 2002, **287**(7), 442-461.

[19] Bagher, A. M. Introduction to organic solar cells. *Sustainable Energy*, 2014, **2**(3), 85-90.

[20] Wu, B., Mathews, N., & Sum, T.C. *Plasmonic Organic Solar Cells: Charge Generation and Recombination*. Springer, 2016.

[21] Heeger, A. J. 25th anniversary article: Bulk heterojunction solar cells: understanding the mechanism of operation. *Advanced Materials*, 2014, **26**(1), 10-28.

[22] Rwenyagila, E. R. A review of organic photovoltaic energy source and its technological designs. *International Journal of Photoenergy*, 2017, **2017**(1), 1656512. Wiley Online Library.

[23] Jain, P. K., & El-Sayed, M. A. Plasmonic coupling in noble metal nanostructures. *Chemical Physics Letters*, 2010, **487**(4-6), 153-164. Elsevier.

[24] Singh, S., Singh, P. K., Umar, A., Lohia, P., Albargi, H., Castañeda, L., & Dwivedi, D. K. 2D nanomaterial-based surface plasmon resonance sensors for biosensing applications. *Micromachines*, 2020, **11**(8), 779. MDPI.

Chapter 2

Literature Review

2.1 Introduction

Today, energy stands as a key player in the running of modern civilization. Its absence presents a tough challenge, indicating insufficient access to food, adequate shelter, and connectivity to the Internet, encompassing the utilization of nanotechnology. The evolution of current energy developments requires the assessment of new technologies and constructing new physical and chemical processes. These are indispensable for the establishment and operation of efficient systems capable of generating, accumulating, transforming, and transporting energy across various forms. Despite global fossil fuel reserves remaining dominant, the noticeable contrary social, health, and environmental impacts resulting from our unsustainable energy consumption patterns highlight the urgency for change. Therefore, the needs for renewable energy resource not only lies in adopting alternative methods to meet these issues, but also provides a great option for enhancing our standard of living [1, 2]. Solar cells stand out as a prospective and potentially essential technology, representing the possible solution of sustainable and ecofriendly energy for the human future. Over the years, silicon and its derivatives such as single-crystalline, multi-crystalline, and amorphous silicon have been the most widely used semiconductor materials for converting sunlight into electricity through the PV process. Among these, single-crystal silicon (monocrystalline silicon) remains the dominant technology in the market due to its highly ordered atomic structure, which reduces defects and enhances charge carrier mobility, resulting in higher efficiency and lower recombination losses compared to multi-crystalline and amorphous silicon [3]. Recently organic solar cell technology has been recommended as the possible solution to cost-effective PV systems. They are emerging as potential substitute to the energy intensive and high cost Si-based PV devices. This shift towards low-cost organic photovoltaic (OPV) systems introduces a promising pathway for establishing sustainable PV based solutions and technologies [4].

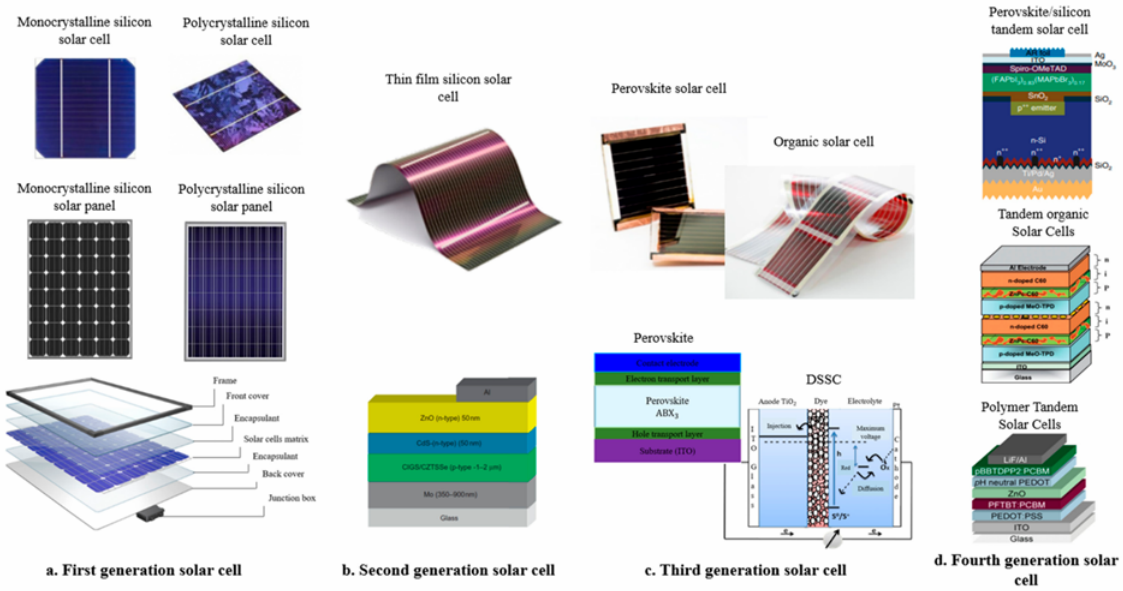

Figure 2.1: Different generations of the solar cells [5].

Early solar cells, such as selenium-based devices developed in the late 19th century, had efficiencies below 1%. Over the following decades, advancements in silicon PVs, material refinement, and cell design led to significant improvements, with the first commercial silicon solar cell achieving around 6% efficiency by 1954. For further optimization, research efforts focused on enhancing efficiency by selecting optimal materials for solar cell manufacturing (see Figure 2.1). Scientific literature indicates that the evolution of cost-effective and more efficient solar cell materials has passed through three main generations classified as first generation, second generation, and third generation. The order of progress reflects continuous improvements from one generation to the next. [7]. First-generation solar cells largely use single crystal Silicon, including monocrystalline and polycrystalline silicon, achieving efficiency values typically ranging from 13% to 22%, with monocrystalline silicon reaching higher efficiencies (15%–22%) and polycrystalline silicon generally falling between 13% and 18% [8, 9]. However, the high cost of single crystals has led to persistent research aimed at cost reduction coupled with efficiency enhancement and as a consequence, second-generation thin-film solar cells were produced. As a result, second-generation thin-film solar cells were developed. These cells, which include amorphous silicon (a-Si), cadmium telluride (CdTe), and copper indium gallium selenide (CIGS), are known for their cost-effectiveness, improved efficiency, greater flexibility, and reduced material usage. Despite their above mention properties, the second generation cells face challenges such as stability issues, lower energy conversion efficiency compared to first-generation silicon cells, and concerns over the toxicity and availability of certain materials, particularly cadmium in CdTe-based solar cells. The third generation of solar cells includes technologies based on dye-sensitized solar cells (DSSCs), organic/polymer solar

cells, nanocrystal-based solar cells, and nanoporous materials [11]. Currently, polymer solar cells (PSCs) represent one of the most promising technologies in the domain of 3rd generation devices as the PCE has been gradually enhanced to 19.9% [12]. As relevant to our work, in the following sections, we will highlight the basic fundaments of organic polymer thin film solar cells including device architecture, the nature of conjugated polymers, active layer materials, bulk heterojunction working principles, charge recombination in BHJ thin film solar cells, current- voltage characteristics of the device, and the concept of the localized surface plasmonic resonance.

2.2 Bulk Heterojunction Organic Solar Cells Configurations

Bulk Heterojunction (BHJ) solar absorber design offered significant advancements in the area of thin-film organic solar cells by providing a mixture of hole-accepting and electron-accepting organic materials that perform far better than traditional single and bi-layer devices [13, 14]. This assumption is based on the fact that the photo-generated excitons in organic semiconducting polymers have strong binding energy due to the low dielectric constant of the organic polymer. A strongly bound exciton implies that the exciton diffusion length is very short typically of the order of 100 nm. This constraint imposes the donor-acceptor interface to be in close proximity to within the exciton diffusion length [15]. Additionally, the electron or hole mobility in these materials are several orders of magnitude lower than their inorganic counterparts, this limits the efficiency of charge separation and transport in the BHJ. [14].

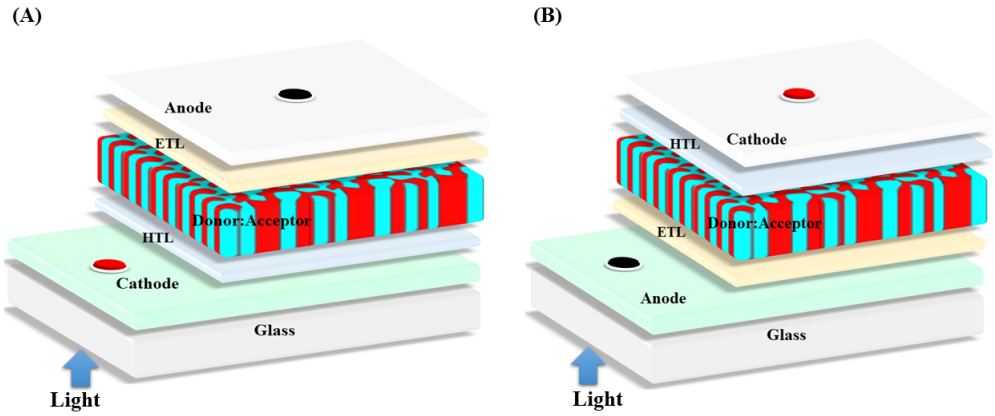

Figure 2.2: Conventional device structure [left], and an inverted device structure [right].

Following the discovery of the BHJ, the efficiency of organic polymer solar cells has been greatly improved by providing a better environment for charge generation, separation, and collection. As repre-

sented in Figure. 2.2. the optimized BHJ system has led to two major types of device structures, each with different functional layers and charge flow directions, which are well-known as the conventional and the inverted structures. These configurations allow for better material optimization and control of charge flow direction, for improving device performance. For example, the conventional structure of thin film OSCs consists of layers that start with a glass substrate at the bottom followed by a transparent conductive oxide layer, such as Indium Tin Oxide (ITO), serving as the anode/a hole collecting layer (HTL), usually made of poly(3,4-ethylenedioxythiophene) polystyrene sulfonate (PEDOT: PSS) with a function to facilitate the transport of holes to the anode while simultaneously blocking the electrons /active layer where light absorption and exciton generation takes place. Electron transport layer (ETL), with materials such as lithium fluoride/and finally, a cathode made of a low work function metal like aluminium [16]. On the other hand, the inverted structure generally rearranges these layers by the following architecture, a glass substrate coated with ITO layer followed by ETL usually consisting of stable materials like zinc oxide (ZnO)/the active layer/HTL such as Molybdenum trioxide (MoO3)/ an anode, usually a high work function metal such as Silver (Ag) or aluminium [17].

2.3 The Origin of Polymer Conductivity

The potential of organic polymer semiconductor materials for light absorption and electrical conductivity stand out from the unique properties of organic semiconductors [18] raised from the arrangement of carbon atoms in a sp^2-hybridization (see Figure. 2.3). In this configuration, the sp^2 orbitals within a plane form a triangular structure, while another plane containing p_z-orbitals is oriented perpendicularly, resulting in the π-conjugated molecular structure. The σ-bonds between the carbon atoms are formed by an orbital overlap of two sp^2-orbitals, creating a molecular structure. In long chains of bound atoms, the energy gap between the HOMO and LUMO is greater, the polymer behaves as an insulator. However, in sp^2-hybridization, the π-bonds formed by the overlap of p_z-orbitals result in a smaller energy gap between the HOMO and LUMO. This characteristic allows for the absorption of visible and near-visible light spectra, giving rise to semiconducting properties in the organic material [19].

A semiconducting polymer consists of a chain of carbon atoms, where each carbon atom is sp^2-hybridized. In this configuration, the carbon atoms have p_z-orbitals that overlap with those of neighboring carbon atoms establishing π-bonds. These π-bonds can extend along the chain creating a delocalized system of π-electrons. The whole system is characterized by an alternating design of single and double bonds throughout the polymer chain. The π-electronic delocalized system can have several numbers of atoms, facilitating the transformation of electrons using the π-electron cloud by either hopping or tunneling. This process gives the polymer its conductive behaviour, where the hopping of charge carriers

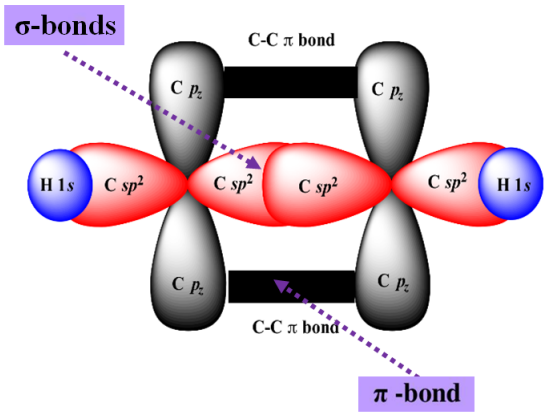

Figure 2.3: The conductivity of the conjugated polymer [20].

depends on the energy gap between the HOMO and LUMO levels of the π-bonds. This entire system is referred to as a conjugated system, leading to the term conjugated polymers [21, 22]. Moreover, the energy gap between the HOMO and the LUMO determines the electronic properties of organic conjugated polymers. By introducing electrons into the LUMO levels, these materials can be modified to behave as n-type semiconductors, while removing electrons from the HOMO levels converts them into p-type materials. This tunable electronic behavior allows these polymers to function as electron acceptors or donors in a variety of applications. Noticeably, conjugated polymers with significantly high HOMO levels tend to perform as p-types (donors) for hole transport, while polymers with low lying LUMO levels are said to be n-doped and are predominantly used as electron accepting materials. [23]. Based on this classification, many types of electron-donating/accepting polymers have been synthesized for several functions including thin-film polymer solar cells.

2.4 Materials For Solar Energy Conversion

Several materials with suitable properties, such as conjugated polymers and small molecular compounds, can serve as electron donor materials in organic thin-film solar cells. On the other side, many organic compounds show promise as electron acceptor materials. However, only a few types of electron-donating materials including P3HT and PTB7 likewise the electron-accepting materials such as $PC_{71}BM$ and $PC_{61}BM$ can provide efficient requirements for BHJ solar cell applications. These materials are chosen based on their optimal bandgap for solar absorption, proper energy level alignment for efficient charge transfer, sufficient driving force for exciton dissociation (LUMO offset higher than 0.3 eV), and ability to form a well-ordered phase-separated morphology for charge transport.

2.4.1 Electron Donating Polymers

Previously, we mentioned that conjugated polymers exhibit excellent electrical conductivity associated by hopping of charge carriers between the HOMO and LUMO energy levels. However, conducting properties alone are not sufficient to functionalize these conjugated polymers as electron donors for thin film PV conversion. Moreover, materials playing such a role need to possess several other characteristics, including broad band light absorption, good miscibility to form a better interface, and crystallinity for effective charge transport [24]. To achieve this, researchers have extensively studied the modification of the conjugated polymer structures including the HOMO and LUMO levels. For example, the size of the band gap and the locations of HOMO and LUMO energy levels of the conjugated polymers have a dominant contribution in influencing the optical and electrical properties [25].

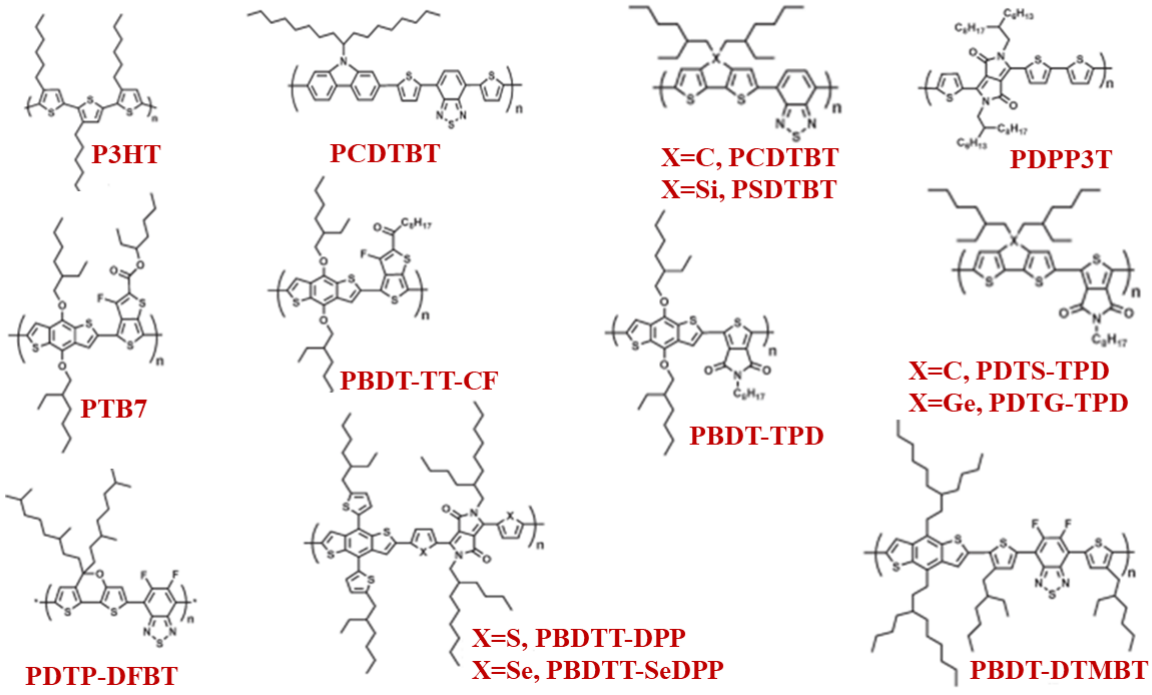

Figure 2.4: Some high-performance electron donors are frequently used in thin-film solar cells [25].

Increasing both the absorption coefficient and V_{oc} of the thin film solar cell device requires a proper energy level alignment between the polymer donor and the fullerene acceptor. These are generally balanced by down-shifting the HOMO level of the p-type materials or up-shifting the LUMO level of the n-type materials [26]. On the other side, the solubility behavior of the conjugated polymers is also greatly enhanced which is usually influenced by many structural factors such as the polymerization level of the polymer, the chain length, the polarity of the attached substituents, backbone stiffness, polymer regioregularity, and the intermolecular interaction [27]. Additionally, several methods have been employed by researchers to introduce conjugated polymers with very high electrical conductivity

including doping through oxidation or reduction chemistry, and base chemistry methods [28].

One of the most significant outcomes of the earlier research and commonly studied as the electron donor for thin film solar cell applications was the P3HT. This is based on the fact that P3HT has several advantages such as regioregularity, charge conductivity, and hole mobility [29]. However, its larger band (1.9 eV) limits the Voc and the threshold for optical absorption leading to significant mismatch with the solar emission spectrum [21]. Today, there are a variety of high-conducting polymers with low band gaps such as PTB7 and D-A types polymers providing superior performance as represented in Figure. 2.4. This advancement was achieved through the employment of several strategies and mechanisms to modify the band gap such as intra-chain charge transfer, bond-length alternation, aromaticity, substituents effects, intermolecular interactions, and π-conjugation length [30].

2.4.2 Electron Accepting Polymers

The use of fullerene derivatives as n-type semiconductors in polymer solar cells (PSCs) was started for the first time with the discovery of the C_{60} fullerene cage in 1992. Where Sariciftci et al investigated nature of the photoinduced electrons transporting from the polymer to the fullerene cage. Their study used poly(2-methoxy-5-(2'-ethyl-hexyloxy)- 1,4-phenylene vinylene) (MEH-PPV) as an electron donor with a fullerene C_{60} acceptor cage in a double layer of the device structure. An ultrafast photo-induced electron transfer between a conjugated polymer MEH-PPV donor and fullerene C60 acceptor cage was observed [31, 23]. However, these double-layered devices showed low PCE due to the short diffusion length of excitons, resulting in inefficient charge separation. This is based on the fact that the C60 fullerene cage has poor miscibility and solubility despite its strong potential for accepting more than six electrons [32, 33]. To address this issue, Gang Yu et al. introduced the BHJ structure for PSCs, using a soluble C60 derivative, $PC_{60}BM$, as the acceptor mixed with MEH-PPV a conjugated polymer donor. The new system significantly improved the efficiency of PSCs by providing a better interface between donor and acceptor for charge dissociation [33]. In addition to its enhanced separation, the newly optimized $PC_{61}BM$ demonstrated several useful properties more than the original fullerene C60 cage. These include sufficient thermal stability, with a crystallization temperature as high as 195°C, high electron affinity, small reorganization energy, and faster electron mobility, reaching up to 2×10^{-3} $cm^2\ V^{-1}\ S^{-1}$ [34]. Since then, numerous efforts have been reported by researchers to further enhance the performance of PC61BM acceptors.

These efforts are based on the fact that the $PC_{61}BM$ structure offers valuable opportunities for optimizing its molecular and structural properties. Generally, modifications were focused on four main areas including the phenyl group, the alkyl chain length, the terminal ester group, and changing the fullerene cage to achieve a higher fullerene derivatives with stronger absorption. The targeted area of

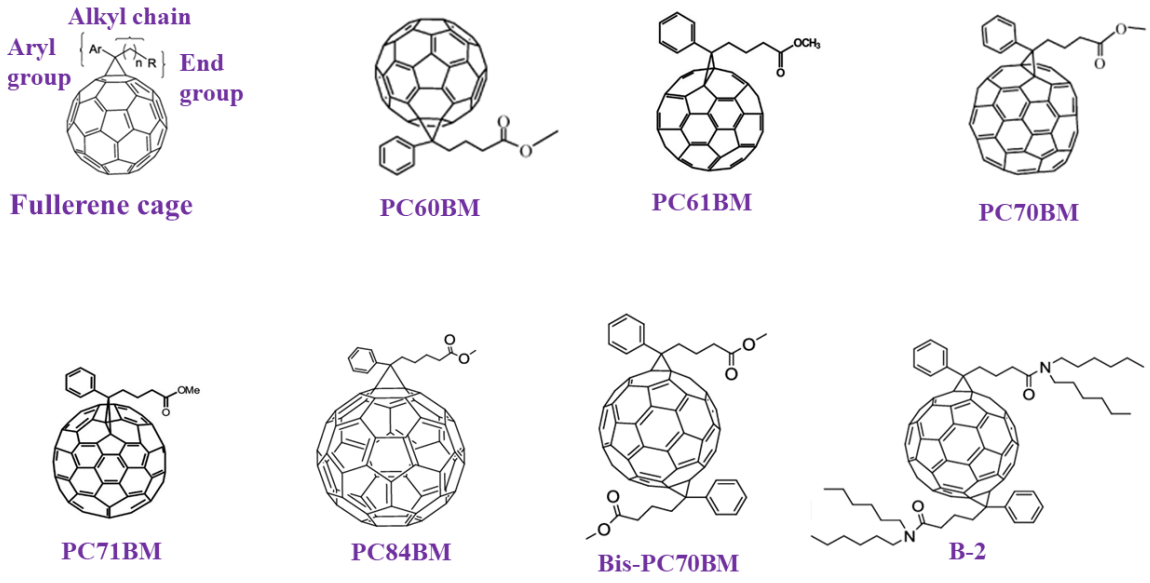

Figure 2.5: Fullerene derivatives [33] [35] [36].

these modifications and some outcomes of fullerenes are displayed in Figure. 2.5. [37]. By using these strategies, numerous fullerene derivatives have been reported such as $PC_{71}BM$, together with many functionally modified fullerene acceptors over the past several years. The new fullerene derivatives have demonstrated superior characteristics of LUMO levels, higher solubility in a variety of solvent and miscibility with versatile electron acceptors [35]. Wienk et al produced $PC_{71}BM$ from the $PC_{61}BM$ and it displayed improved light absorption in the visible region when mixed with MDMO-PPV polymer donor. More importantly, the Jsc of the latest device was twice as high as that of the first, achieving a PCE of 3.0% [38]. Generally, the expansion to the new acceptors' studies has been continuing today as there are numerous types of fullerene derivatives originating from fullerene C60 cage, $PC_{61}BM$, and $PC_{71}BM$ playing an important role in enhancing the efficiency of thin films organic solar cells.

2.5 Operating Principles of BHJ Organic Solar cell

As represented in (Figure. 2.6. and Figure. 2.7.) the working mechanisms of these solar cells can be classified into four major steps: (1) light absorption and exciton generation, (2) Exciton diffusion to the donor/acceptor heterojunction interface, (3) Exciton separation at the donor/acceptor interface, and (4) free electrons and holes (carrier) transport and collection by the respective electrodes. In the following section, we will go through each these mechanisms in greater detail.

2.5.1 Light Absorption and Exciton Generation

Figure. 2.6. shows the absorption of an incident photon by the electron in the HOMO and its transition to the LUMO of the donor polymer. The unique characteristics of organic semiconductors such as their small dielectric constant and localized electron and hole wavefunctions, result in the formation of a tightly bounded electron-hole pair formation with typical binding energies in the range 0.1-0.4 eV. The strong electrostatic attraction between the resulting electron-hole pair gives rise to what is well-known as an exciton (see Figure. 2.7(a)) [39, 40, 41]. In contrast, the binding energy of inorganic semiconductors is only a few meV. Consequently, there is a higher probability of immediately generating free charge carriers following photon absorption in inorganic semiconductors, where electron-hole pairs are simply separated due to thermal energy absorption. In addition, the active layer thickness of organic polymer-based solar cells and the short lifetime of photo-generated excitons challenging. However, it's possible to achieve sufficient and effective light absorption by reducing the active layer thickness to a few hundred nanometers, thanks to the high absorption coefficient of organic materials, which can reach approximately 10^5 cm^{-1} [3, 43]. To enhance the optical absorption of the polymer solar cells, especially in the regions where the photon harvesting is weak, several light-trapping mechanisms have been employed such as incorporating metal nanoparticles [44], doping with surface plasmonic and localized surface plasmonic metal nanoparticles [45, 46], double bulk heterojunction solar cells [47], and tandem solar cells [48], etc. A significant challenge with polymer solar cells stands out in the large band gap and limited absorption range of the donor material, resulting in inefficient photon absorption in the longer wavelength spectrum. In this concern, an earlier study reported that when the energy offset between LUMO – HOMO ranges reach 1.1 eV, the absorption efficiency of the solar absorber material can only extract approximately 77% of solar light [49]. In contrast, the widely-used OSC standard material P3HT possesses a band gap of around 1.9 eV, and PTB7 = 1.64 eV, while the majority of organic materials exhibit band gaps in the vicinity of 1.6 to 2 eV [50, 51].

2.5.2 Exciton Diffusion and Separation

After the exciton generation process occurs, the following challenge is separating the bound electron-hole pair into the generation of free charge carriers. This challenge is raised from the binding energy of the photo-generated excitons of organic polymer semiconductors which is approximately one order of magnitude higher than that of inorganic semiconductors. However, in organic semiconductor materials, this room-temperature thermal energy is insufficient for effective exciton dissociation into free charges, even at high internal electric fields such as ($\sim 10^6$ – 10^7 V/m) [39]. Concerning status, former research indicated that, the largely studied Poly(2-methoxy-5-(2 -ethyl-hexyloxy)-pphenylene vinylene) (MEH-PPV) [53] investigations have shown only 10% of the excitons are separated into free charges in a pure

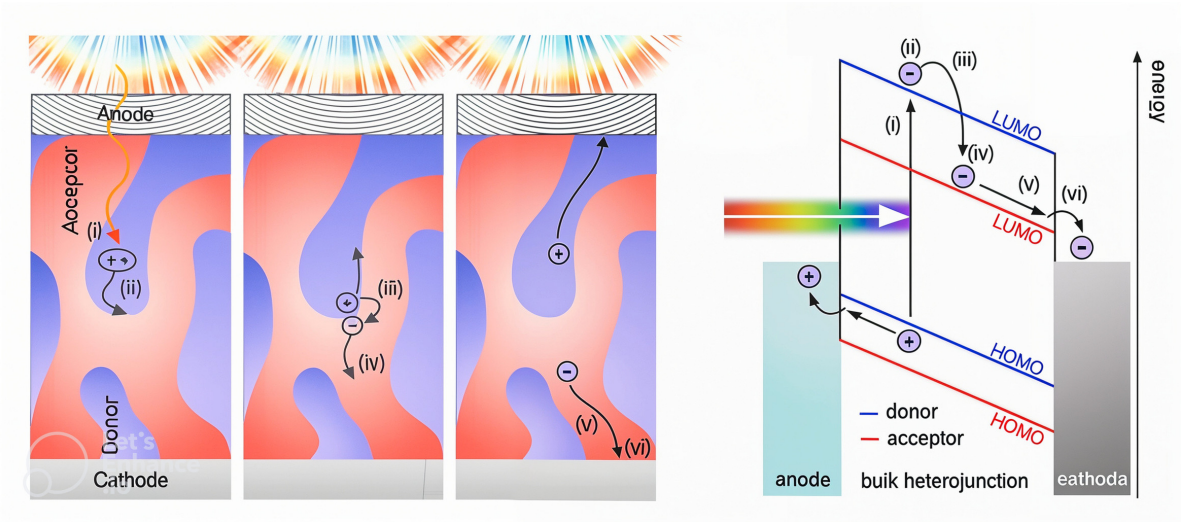

Figure 2.6: The working principles of organic bulk heterojunction solar cells [52].

layer [54], while the rest of excitons are decay through radiative or non-radiative recombination paths, resulting in very low efficiencies for single-layer polymer-based solar cells 0.1% [55, 56]. Heeger et al. have provided a remarkable approach by mixing two dissimilar organic materials with carefully aligned band levels and found that they produce superior performance than single-layer solar cells. This superior performance was attributed to the increased interface between the donor and the acceptor materials. It is also referred to as the heterojunction and it is the critical component of the OPV device design [57]. Using this model, the bound electron-hole pairs can migrate through the polymer layer material to the heterojunction and form so-called charge transfer states CTS (see Figure. 2.6 and Figure. 2.7 (b)). Following this, the CTSs can be effectively separated into free charges at the interface between polymer donor and acceptor molecules through the large potential drop. In contrast to the single-layer solar cell where the majority of excitons recombine in a moment, in heterojunction the electron can easily hop from the HOMO of the donor to the LUMO of the acceptor if the energy difference between HOMO and LUMO is higher than the exciton binding energy [58, 59]. The distance over which excitons can diffuse before separation takes place is known as the exciton diffusion length. For organic semiconductors, these exciton diffusion lengths are limited by only a few tens of nanometers [60, 52], and the excitons generated beyond this range from the heterojunction are more likely to recombine than separate before reaching to heterojunction interface, due to the short lifetime of the photo-generated excitons. Consequently, maintaining thin active layers has been an important technique to ensure that phase separation between the donor and acceptor occurs within the exciton dissociation length.

2.5.3 Free Charges Transport

Following the successful dissociation of exciton at the D/A interface, the resulting free charges (FCs) need to migrate to their corresponding anode and cathode for collection within a short time. The drift and diffusion currents usually influence the diffusion of holes toward the anode and electrons toward the cathode. The drift current is associated with the movement of FC_s alongside the build-in potential across the active layer of the solar cell device, which is generally optimized by the rational selection of the metal electrodes. Moreover, when a solar cell exhibits a large work function anode with a small work function cathode, the produced potential difference between two sides of the active layer forms a built-in electric field that contributes to determining the V_{oc} and influences the charge transport process [61, 62].

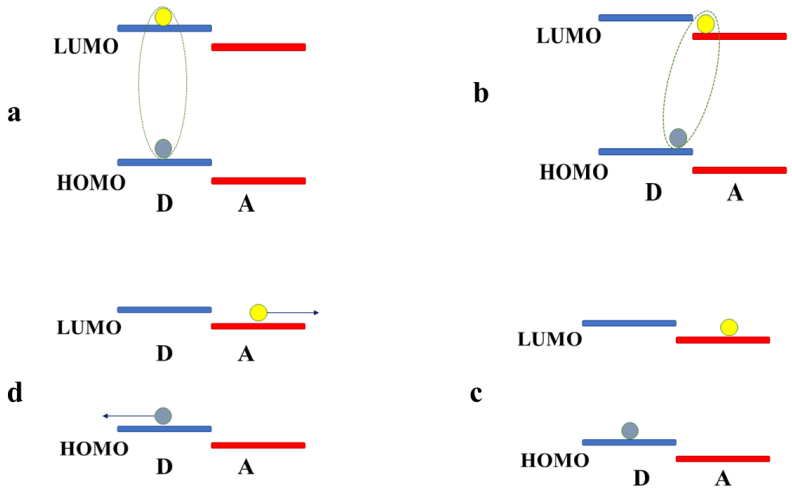

Figure 2.7: A schematic representation for the working principles of organic bulk heterojunction solar cells.

In such a case, once an external voltage is applied, an alteration occurs to the both internal electric field as well as the drift current. Consequently, the impacts of the drift current appear as the FC_s move along the modified internal electric field into their corresponding electrodes for collection. Another charge transport mechanism also takes place once the effect of the applied voltage on the internal electric field is almost zero. In this case, the charge transport process is influenced by the diffusion current, where the FC_s migrate through their raised accumulation area to the lower charge concentration areas. It is important to mention that, when the excitons are generated at an area near the solar cell interface, there will be a possible accumulation of electrons and holes in this area [47, 63]. Leading to the diffusion of charges away from the interface through the accumulation area, resulting in the diffusion current. For example, electrons in regions of high concentration within the acceptor material diffuse toward regions of lower concentration. Conversely, holes in regions of high concentration within the donor material

diffuse toward regions of lower [64]. One of the major challenges that limit the charge transport in polymer solar cells is their mobility within the active layer. This challenge originates from the relatively low hole and electron mobilities in organic polymer materials [65]. To overcome this issue, a technique such as maintaining a thin active layer is necessary to allow the FC_s to reach the electrodes within their lifetimes. Another factor also undesirably contributes to the mobility of the FC_s in the device, which is the electron/hole mobility ratio [66]. For example, if the mobility of electrons is much greater than that of holes, the mobility difference will lead to the formation of so-called space charge limited current (SCLC) in the solar cell device. Moreover, the SCLC occurs once one type of charge has higher mobility than its counterpart [67]. In organic polymer solar cells, it's widely known that the electrons have greater mobility than holes. Consequently, their transport towards the cathode is significantly more efficient than holes reaching the anode. This behavior leads to the accumulation of electrons at an active layer near the cathode interface [68]. Generally, this accumulation influences the space charge effect and imposes an upper limit on the current output of a solar cell. Therefore, possible balanced mobility between holes and electrons is very important to achieve effective charge transport in the active layer of polymer solar cells.

2.5.4 Charge Collection By Electrodes

Following the successful transport to the polymer/electrode (P/E) interface, the FC_s are collected from the active layer to the electrodes as the final step for the light-electricity conversion. To improve the effectiveness of this process, it is essential to minimize the potential barrier at the P/E interfaces. This ensures that the work functions of the anode and cathode are well aligned with the HOMO and LUMO of the donor and acceptor respectively. When this alignment is achieved, the contacts are referred to as Ohmic contacts, and the V_{oc} of the device is positively dependent on the energy difference between the LUMO of the acceptor and the HOMO of the donor [12]. In contrast, if the work functions of the anode and cathode materials do not closely match the donor HOMO or acceptor LUMO, the Ohmic contact will not be formed and the V_{oc} will be negatively affected. In such cases, the FC_s collection process is controlled by the metal-insulator-metal model [70, 71]. Two approaches are widely used to enhance the matching of work functions at the electrodes such as employing different types of materials as work functions materials, besides inserting interlayers (buffer layers) between the electrodes and the active layer to optimize the alignment of the electrode work function and the active layer LUMO or HOMO. Concerning the first case, indium tin oxide (ITO) is a common choice for the anode contact due to its work function of approximate range between 4.40–5.40 eV [72, 73], which demonstrated a good alignment with the HOMO of P3HT polymer donor $-5.0\,\text{eV}$ to $-5.4\,\text{eV}$) [74]. On the other side, low-work function metals such as aluminum (Al, 4.2 eV) are frequently employed as a cathode contact with

the LUMO of PCBM. Beyond the material selection, interlayers can be inserted between the electrodes and the active layer to further align the electrode work function with the active layer's LUMO or HOMO. For example, a thin layer of lithium fluoride (LiF) is widely used as a buffer layer between the active layer material and cathode as a mechanism for ohmic contact formation in this area [75]. On the anode side, poly(3,4-ethylenedioxythiophene) polystyrene sulfonate (PEDOT:PSS) is frequently used as a hole selection material in conventional solar cell architecture [51]. While in an inverted solar cell configuration, several solution-treated materials such as TiO2 [77] and zinc oxide (ZnO) [78] have demonstrated great performance in enhancing electron collection. Similarly, transition metal oxides such as molybdenum trioxide (MoO3) or tungsten trioxide (WO3) have been used as interlayers to form ohmic contacts at the anode side [79, 80].

2.6 Charge Recombinations In OSCs

The success of BHJ design is based on the formation of large area D/A interfaces for effective dissociation of exciton's. However, in practical applications, several issues arise due to Energy loss (E_{LOSS}) at various steps of the polymer solar cells' operation, significantly limiting their efficiency (see Figure.2.8). Overall, solar cells can lose energy during the absorption process for those photons residing outside of the active layer band gap [81]. Added to that, the device can also lose recombination in the form of excitons and through charge transformation and collection process as well. Specifically, the process of charge or energy loss inside the BHJ polymer solar cell systems is generally known as charge recombination which can be divided into Geminate recombination (GR) and Non-geminate recombination (NGR). GR includes the recombination of photogenerated excitons or CTSs before they completely dissociate into FC_s. NGR, on the other hand, occurs after the successful separation of excitons into FCs and before being extracted by their corresponding electrodes, the details are discussed in the section below.

2.6.1 Geminate Charge Recombinations

Due to the complex nature of photo-generated excitons, the GR can occur immediately after the exciton formations and during their diffusion, as well as in the form of CTSs. The complex nature of excitons arises from their relatively strong electrostatic attraction force, limited lifetime, and other issues related to the semiconductor polymer materials. GR during the diffusion process is usually influenced by the short lifetime of excitons and the large domain size of the donor-acceptor mixture, which results from poor miscibility [82]. As represented in Figure. 2.9. there are possible probabilities for electron/hole pairs recombination and relaxation to the ground state to occur before their diffusion to the interface. Additionally, the probability of photo-generated recombination at the D/A interface is very high after

their successful migration to the D/A interface and the formation of CTSs. For the CTSs, the electron is placed in the acceptor phase, while the hole resides in the donor phase before being fully separated by the built-in electric field as shown in Figure. 2.8. Thus, the binding energy for the CTSs will remain active and evaluated as a few hundred milli-electron volts which is slightly greater than room-temperature thermal energy [83, 84]. If the CTSs fail to dissociate into free charges they will recombine and relax to the ground energy states and transfer to the local triplet energy states.

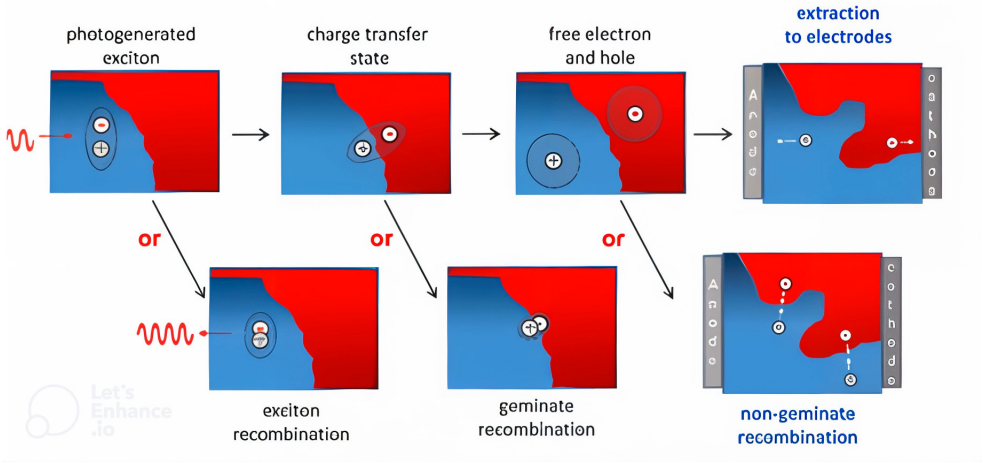

Figure 2.8: Free charges generation and recombination principles of organic bulk heterojunction solar cells [52].

In this case, if the energy of the geminate CTS is higher than that of the triplet state, the excitons are expected to diffuse again excited singlet state, S_1 to the heterojunction, otherwise, they will relax to the S_0 state through radiative and nonradiative decays (see Figure. 2.9) [85]. The amount of energy required to fully separate CTSs is still unclear. For example, earlier reports believed that the effective separation, 0.3 eV of energy should be available which is the energy difference between the LUMO of the acceptor and the HOMO of the donor [86]. However, other studies have achieved dissociation with low energy offset [87]. Generally, the thermal ionization energy rate (K_i) required to split the CTSs is estimated by:

$$K_i = \omega_0 \exp\left(\frac{-E_b}{KT}\right) \tag{2.1}$$

Where E_b is the binding energy of the charge transfer state at the heterojunction. The possibility of ionization of the charge transfer state for a recombination rate is given by:

$$P_i = \frac{K_i}{K_I + K_r} \tag{2.2}$$

$$P_i = \left[1+K_r\omega_o^{-1}\exp\left(\frac{E_b}{KT}\right)\right]^{-1} \tag{2.3}$$

where K_r is the charge transfer recombination rate. For high-efficiency solar cells where the ionization rate is much greater than the recombination rate, the possibility of the geminate charge recombination is evaluated by $P_{geminate}$ = 1 - P_i which is approximately = K_r ω_0 $^{-1}$ exp $(\frac{E_b}{KT})$ [88].

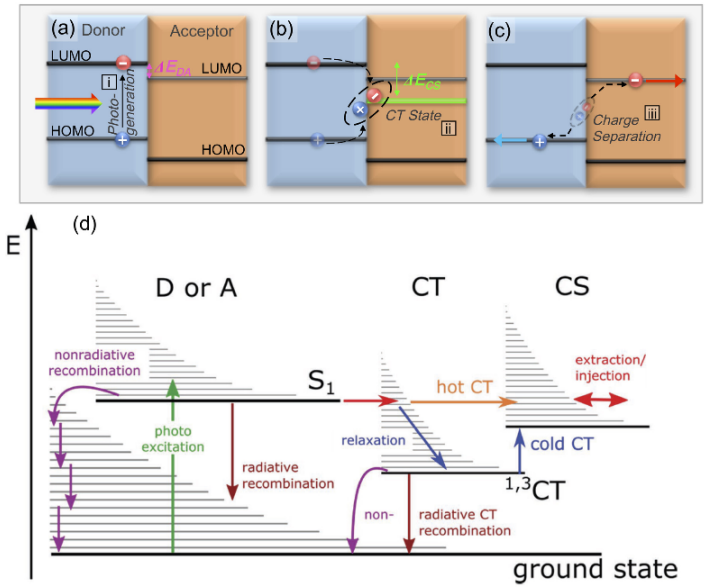

Figure 2.9: Geminate and non-geminate charge recombination diagram as described by Jablonski for an organic solar cell heterojunction. [89]

2.6.2 Non-Geminate Charge Recombinations

Following the subsequent CTSs separation into free electrons and holes, the probability for these charge carriers to encounter each other and recombine before they can be extracted by their corresponding electrodes remains possible. Non-geminate recombination is also known as bimolecular charge recombination in polymer solar cells, and it can be influenced by several factors including thin film thickness, electron/hole mobility, trap assist, charge density, temperature... etc. [90]. Non-geminate recombination is widely considered a major source that affects the fill factor, and the efficiency of the polymer TFSCs. The nongeminate recombination rate is generally an arbitrary process depending on the oppositely charged free carrier's density and mobility. Several models have been employed to study this type of recombination including Langevin recombination and Shockley–Read–Hall trap-assisted recombination. Langevin recombination originated from the diffusion equation, where direct recombination takes place for oppositely signed free charges as they encounter each other in the presence of an electric field [91]. The charge transport rate (β) according to the Langevin assumption is estimated by:

$$\beta = \frac{e(\mu_e+\mu_h)}{\varepsilon\varepsilon_0} \tag{2.4}$$

here μ_h and μ_e are the hole and the electron mobility respectively, e is the elementary charge, and ε and ε_0 are the permittivity of the medium and free space respectively [92]. In experiments, Langevin recombination constants are usually used to deviate significantly from theoretical values. This deviation can be influenced by many issues, such as larger single phased domain sizes, enlarged energetic disorder, and unbalanced electron/hole mobility. Shockley–Read–Hall recombination, on the other hand, includes energy states or tail states inside the bandgap that act as traps for charge carriers [93, 94]. This model takes the form of cases where mid-gap traps exist, and the free charges are then trapped and released by trap states, resulting in trap-assisted recombination. The free charge trap, de-trap, and recombination are calculated by the following equation:

$$\frac{\delta n_t}{\delta t} = r_{ec}-r_{ee}-r_{hc}+r_{he} \tag{2.5}$$

Where r_{he} and r_{ee} are the rate at which the hole/electron can become freed from the trap state to become free charges again respectively, r_{he} and r_{ec} are hole and electron trapped rate [95, 96]. Generally, researchers employ several methods to study NG recombination, such as transient electrical measurements and steady-state measurements.

2.7 Solar Cell Parameters

The characterization of the solar cell depends on the measured current density - voltage (J-V) characteristics which provides valuable information about the internal dynamic and quality of the solar cell once the device is in the dark and illumination conditions. As represented in Figure. 2.10. when the solar cell is under dark conditions, the current density - voltage characteristic resembles that of a diode operating in the forward biased direction. In this instance the short circuit current (J_{sc}) and the open circuit voltage (V_{oc}) are zero. However, under illumination conditions (solid curve), the photocurrent is down shifted due to the effect of photoabsorption and carrier generation. Deriving from the current density to voltage, or the J-V curve, several characteristic parameters can be determined [97]. The first among these parameters is the short circuit current density (J_{sc}), which represents the total value of the current density at zero voltage. This parameter depends upon the selection of the specific material used for the active layer and the thickness of the active layer as well [98]. The second parameter is the open-circuit voltage (V_{oc}), which represents the voltage at which there is no net current flowing through the device. The determination of the V_{oc} is fundamentally associated with the energy differ-

ential between the HOMO of the donor material and the LUMO of the acceptor material of the active layer components.

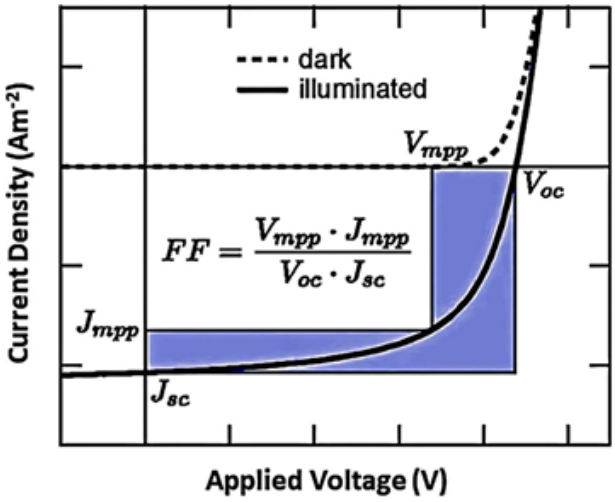

Figure 2.10: Represents the current-voltage characteristic of the solar cell under dark and illumination conditions [99].

Moreover, the V_{oc} of solar cells serves as the maximum potential delivered by a device to an external circuit and it can be evaluated by the separation of hole and electron quasi-Fermi levels. For crystalline silicon solar cells, the stable effective density of states is found at the base of the conduction (valence) band, facilitating the direct calculation of the quasi-Fermi level through the Fermi–Dirac distribution. On the other hand, organic materials are similar to amorphous silicon, exhibit gap tail states that are induced by disorder [69]. Consequently, the relaxation of carriers into these tail states results in a downward shift of the electron quasi-Fermi level and an upward shift of the hole quasi-Fermi level affecting the value of V_{oc} [70]. Understanding the factors influencing V_{oc} in organic heterojunction solar cells is a significant challenge for achieving scientific and technological proficiency in this field. Over decades, a various material combination and enhanced experimental techniques, have contributed to understanding the causes of V_{oc} losses in organic BHJ solar cells. The primary voltage losses are associated with the polymer materials interface including separating the photo-generated exciton into a charge pair at the donor/acceptor heterojunction interface and the non-radiative recombination of separated charges [100]. The third parameter is the maximum power point, for example, once the voltage range takes the values between V = 0 to V = V_{oc} on the J-V curve, there is a specific point at which the product of the voltage and the current density is a maximum. This operating point is referred to as the maximum power point of the solar cells device. It represents the operating point at which the PV device delivers the highest power as shown below: $P_{MPP} = V_{MPP}$ x J_{MPP}. As indicated in (Figure. 2.10). this particular point is identified as the maximum power point(P_{MPP}) of the solar

cell device, where the solar cell delivers the highest amount of power as shown below [101].

$$P_{MPP} = J_{MPP}.V_{MPP} \tag{2.6}$$

The J-V curve also provides another key parameter known as the fill factor (FF), which is calculated by dividing the power at the maximum power point by the product of the open-circuit voltage and the short-circuit current as shown below:

$$FF = \frac{P_{MPP}}{J_{sc}.V_{oc}} = \frac{J_{MPP}.V_{MPP}}{J_{sc}.V_{oc}} \tag{2.7}$$

The fill factor is dependent upon the efficiency of charge collection and can be negatively affected by several factors such as bimolecular recombination, imbalanced charge transport, as well as parallel and series resistance [102]. The FF of the solar cell system is a measurement that characterizes the squareness quality of the J–V curve (see Figure. 2.10), reflecting the ease or difficulty with which photo-generated carriers can be extracted from a PV device. An optimal FF value is unity (100%) which can be reached when the J–V curve forms a rectangle. In this scenario, a slight deviation from the V_{oc} can cause the current density to rise perpendicularly to its maximum value J_{sc}. This behavior remains unchanged even as the applied voltage changes from V_{oc} to zero Volts and undergoes significant reversed bias. However, attaining a perfect FF of 100% is unfeasible in practice even in inorganic solar cells that report higher PCE [46]. Due to the complicated device structure resulting from the BHJ and the complex mechanism encompassing the conversion of photons to charge carriers, this parameter demonstrates to be more abstract compared to other factors determining PCE, such as V_{oc} and J_{sc} [104]. The last parameter is the power conversion efficiency, for example, in measuring the efficiency of solar cells under Air Mass (AM) 1.5G illumination with an intensity of incident power (light) P_{in}= 100 W/cm^2, the maximum generated power point is used to calculate the PCE. The PCE is the amount of power output to power input, providing a system of measurement for the generated power to the incident solar radiation's available power Pin. In this context, P_{in} encompasses the collective power across all wavelengths and is consistent at 100 W/cm^2 in scenarios involving solar simulators. This definition offers a comprehensive and widely applicable characterization of efficiency. Considering the previously defined quantities the PCE is evaluated by using the following formula:

$$PCE = \frac{P_{MPP}}{p_{In}} = \frac{J_{sc}.V_{oc}.FF}{P_{In}} \tag{2.8}$$

Generally, the AM denotes the atmospheric thickness sunlight crosses before reaching the earth's surface. This phenomenon is generally denoted as AM(x), where x represents the inverse of the cosine of the

sun's zenith angle. In solar cell measurements, AM 1.5 is often employed, corresponding to a solar angle of approximately 48°. However, as the air mass is characterized by the solar radiation spectrum it doesn't consider the significance of intensity. therefore, the subsequent intensity for the solar cell analysis is fundamentally fixed at 100 W/cm^2 [105].

References

[1] Ranabhat K., Patrikeev L., Revina A. A., Andrianov K., Lapshinsky V., Sofronova E. An introduction to solar cell technology. *Journal of Applied Engineering Science*, **14**(4), 2016.

[2] Dorian J. P., Franssen H. T., Simbeck D. R. Global challenges in energy. *Energy Policy*, **34**(15), pp. 1984-1991, 2006. Elsevier.

[3] Liu Y., Li Y., Wu Y., Yang G., Mazzarella L., Procel-Moya P., Tamboli A. C., Weber K., Boccard M., Isabella O., et al. High-efficiency silicon heterojunction solar cells: materials, devices and applications. *Materials Science and Engineering: R: Reports*, **142**, pp. 100579, 2020. Elsevier.

[4] Rwenyagila E. R. A review of organic photovoltaic energy source and its technological designs. *International Journal of Photoenergy*, **2017**(1), pp. 1656512, 2017. Wiley Online Library.

[5] Sarr A., Soro Y. M., Tossa A. K., Diop L. Agrivoltaic, a synergistic co-location of agricultural and energy production in perpetual mutation: A comprehensive review. *Processes*, **11**(3), pp. 948, 2023. MDPI.

[6] Venkateswari R., Sreejith S. Factors influencing the efficiency of photovoltaic system. *Renewable and Sustainable Energy Reviews*, **101**, pp. 376-394, 2019. Elsevier.

[7] Tang C. W. Two-layer organic photovoltaic cell. *Applied Physics Letters*, **48**(2), pp. 183-185, 1986. AIP Publishing.

[8] Baghel, N.S. and Chander, N., 2022. Performance comparison of mono and polycrystalline silicon solar photovoltaic modules under tropical wet and dry climatic conditions in east-central India. Clean Energy, *6(1)*, pp.165-177.

[9] Sugianto, S., 2020. Comparative analysis of solar cell efficiency between monocrystalline and polycrystalline. INTEK: Jurnal Penelitian, *7(2)*, pp.92-100.

[10] Pattelath, M.S., Giripunje, S.M. and Verma, A.K., 2023. A Review of Photovoltaic Cell Generations and Simplified Overview of Bifacial Photovoltaic Cell Technology. Applied Solar Energy, *59(5)*, pp.621-646.

[11] Ahmad K. S., Naqvi S. N., Jaffri S. B. Systematic review elucidating the generations and classifications of solar cells contributing towards environmental sustainability integration. *Reviews in Inorganic Chemistry*, **41**(1), pp. 21-39, 2021. De Gruyter.

[12] Vandewal K., Widmer J., Heumueller T., Brabec C. J., McGehee M. D., Leo K., Riede M., Salleo A. Increased open-circuit voltage of organic solar cells by reduced donor-acceptor interface area. *Advanced Materials*, **26**(23), pp. 3839-3843, 2014.

[13] Bernede, J.C., 2008. Organic photovoltaic cells: history, principle and techniques. Journal of the Chilean Chemical Society, *53(3)*, pp.1549-1564.

[14] Sundar V. C., Zaumseil J., Podzorov V., Menard E., Willett R. L., Someya T., Gershenson M. E., Rogers J. A. Elastomeric transistor stamps: reversible probing of charge transport in organic crystals. *Science*, **303**(5664), pp. 1644-1646, 2004. American Association for the Advancement of Science.

[15] Sajjad, M.T., Ruseckas, A. and Samuel, I.D., 2020. Enhancing exciton diffusion length provides new opportunities for organic photovoltaics. Matter, *3(2)*, pp.341-354.

[16] Hamed M. S. G., Ike J. N., Wang Y., Zhou K., Ma W., Mola G. T. Reducing Energy Loss in Polymer Solar Cell through Optimization of Novel Metal Nanocomposite. *Energy & Fuels*, **37**(8), pp. 6129-6137, 2023. ACS Publications.

[17] Hamed M. S. G., Adedeji M. A., Mola G. T. Rare-earth metal-induced plasmon resonances for enhanced photons harvesting in inverted thin film organic solar cell. *Energy & Fuels*, **35**(18), pp. 15010-15017, 2021. ACS Publications.

[18] Heeger A. J. Semiconducting and metallic polymers: the fourth generation of polymeric materials. *The Journal of Physical Chemistry B*, **105**(36), pp. 8475-8491, 2001. ACS Publications.

[19] Malik A. H., Habib F., Qazi M. J., Ganayee M. A., Ahmad Z., Yatoo M. A. A short review article on conjugated polymers. *Journal of Polymer Research*, **30**(3), pp. 115, 2023. Springer.

[20] https://www.chem.ucla.edu/ harding/IGOC/S/sp208.png

[21] R. Murad A., Iraqi A., Aziz S. B., N. Abdullah S., Brza M. A. Conducting polymers for

optoelectronic devices and organic solar cells: A review. *Polymers*, **12**(11), pp. 2627, 2020. MDPI.

[22] Al-Azzawi A. G. S., Aziz S. B., Dannoun E. M. A., Iraqi A., Nofal M. M., Murad A. R., M. Hussein A. A mini review on the development of conjugated polymers: Steps towards the commercialization of organic solar cells. *Polymers*, **15**(1), pp. 164, 2022. MDPI.

[23] Li Y., Huang W., Zhao D., Wang L., Jiao Z., Huang Q., Wang P., Sun M., Yuan G. Recent progress in organic solar cells: a review on materials from acceptor to donor. *Molecules*, **27**(6), pp. 1800, 2022. MDPI.

[24] Lu L., Yu L. Understanding low bandgap polymer PTB7 and optimizing polymer solar cells based on it. *Advanced Materials*, **26**(26), pp. 4413-4430, 2014. Wiley Online Library.

[25] Dou L., You J., Hong Z., Xu Z., Li G., Street R. A., Yang Y. 25th anniversary article: a decade of organic/polymeric photovoltaic research. *Advanced Materials*, **25**(46), pp. 6642-6671, 2013. Wiley Online Library.

[26] Bundgaard E., Krebs F. C. Low band gap polymers for organic photovoltaics. *Solar Energy Materials and Solar Cells*, **91**(11), pp. 954-985, 2007. Elsevier.

[27] Cheng Y.J., Yang S.H., Hsu C.S. Synthesis of conjugated polymers for organic solar cell applications. *Chemical Reviews*, **109**(11), pp. 5868-5923, 2009. ACS Publications.

[28] Salaneck W. R., Friend R. H., Brédas J. L. Electronic structure of conjugated polymers: consequences of electron-lattice coupling. *Physics Reports*, **319**(6), pp. 231-251, 1999. Elsevier.

[29] Bhatta R. S., Tsige M. Chain length and torsional dependence of exciton binding energies in P3HT and PTB7 conjugated polymers: A first-principles study. *Polymer*, **55**(11), pp. 2667-2672, 2014. Elsevier.

[30] Mehmood U., Al-Ahmed A., Hussein I. A. Review on recent advances in polythiophene based photovoltaic devices. *Renewable and Sustainable Energy Reviews*, 2016, **57**, pp 550-561.

[31] Sariciftci N. S., Smilowitz L., Heeger A. J., Wudl F. Photoinduced electron transfer from a conducting polymer to buckminsterfullerene. *Science*, 1992, **258**(5087), pp 1474-1476.

[32] Seyler H., Wong W. W. H., Jones D. J., Holmes A. B. Continuous flow synthesis of fullerene derivatives. *The Journal of Organic Chemistry*, 2011, **76**(9), pp 3551-3556.

[33] He Y., Li Y. Fullerene derivative acceptors for high performance polymer solar cells. *Physical*

Chemistry Chemical Physics, 2011, **13**(6), pp 1970-1983.

[34] Mi D., Kim J.H., Kim H. U., Xu F., Hwang D.H. Fullerene derivatives as electron acceptors for organic photovoltaic cells. *Journal of Nanoscience and Nanotechnology*, 2014, **14**(2), pp 1064-1084.

[35] Ganesamoorthy R., Sathiyan G., Sakthivel P. Fullerene based acceptors for efficient bulk heterojunction organic solar cell applications. *Solar Energy Materials and Solar Cells*, 2017, **161**, pp 102-148.

[36] Bernardo G., Melle-Franco M., Washington A. L., Dalgliesh R. M., Li F., Mendes A., Parnell S. R. Different agglomeration properties of PC 61 BM and PC 71 BM in photovoltaic inks-a spin-echo SANS study. *RSC Advances*, 2020, **10**(8), pp 4512-4520.

[37] Troshin P. A., Hoppe H., Renz J., Egginger M., Mayorova J. Y., Goryachev A. E., Peregudov A. S., Lyubovskaya R. N., Gobsch G., Sariciftci N. S., et al. Material solubility-photovoltaic performance relationship in the design of novel fullerene derivatives for bulk heterojunction solar cells. *Advanced Functional Materials*, 2009, **19**(5), pp 779-788.

[38] Wienk M. M., Kroon J. M., Verhees W. J. H., Knol J., Hummelen J. C., Van Hal P. A., Janssen R. A. J. Efficient methano [70] fullerene/MDMO-PPV bulk heterojunction photovoltaic cells. *Angewandte Chemie International Edition*, 2003, **42**(29), pp 3371-3375.

[39] Gregg B. A., Hanna M. C. Comparing organic to inorganic photovoltaic cells: Theory, experiment, and simulation. *Journal of Applied Physics*, 2003, **93**(6), pp 3605-3614.

[40] Fung D. S., Choy W. C. Introduction to organic solar cells. In *Organic Solar Cells: Materials and Device Physics*, Springer, 2012, pp 1-16.

[41] Mayer A. C., Scully S. R., Hardin B. E., Rowell M. W., McGehee M. D. Polymer-based solar cells. *Materials Today*, 2007, **10**(11), pp 28-33.

[42] Coakley K. M., McGehee M. D. Conjugated polymer photovoltaic cells. *Chemistry of Materials*, 2004, **16**(23), pp 4533-4542.

[43] Brütting W. Introduction to the physics of organic semiconductors. In *Physics of Organic Semiconductors*, Wiley Online Library, 2005, pp 1-14.

[44] Jabeen U., Shah S. M., Hussain N., Ali A., Khan S. U., et al. Synthesis, characterization, band gap tuning and applications of Cd-doped ZnS nanoparticles in hybrid solar cells. *Journal of Photochemistry and Photobiology A: Chemistry*, 2016, **325**, pp 29-38.

[45] Duche D., Torchio P., Escoubas L., Monestier F., Simon J.J., Flory F., Mathian G. Improv-

ing light absorption in organic solar cells by plasmonic contribution. *Solar Energy Materials and Solar Cells*, 2009, **93**(8), pp 1377-1382.

[46] Li X., Choy W. C. H., Lu H., Sha W. E. I., Ho A. H. P. Efficiency enhancement of organic solar cells by using shape-dependent broadband plasmonic absorption in metallic nanoparticles. *Advanced Functional Materials*, 2013, **23**(21), pp 2728-2735.

[47] Xie F.x., Choy W. C. H., Wei E. I., Zhang D., Zhang S., Li X., Leung C.-w., Hou J. Enhanced charge extraction in organic solar cells through electron accumulation effects induced by metal nanoparticles. *Energy & Environmental Science*, 2013, **6**(11), pp 3372-3379.

[48] Zhang Y., Kan B., Sun Y., Wang Y., Xia R., Ke X., Yi Y.Q., Li C., Yip H.L., Wan X., et al. Nonfullerene tandem organic solar cells with high performance of 14.11%. *Advanced Materials*, 2018, **30**(18), p 1707508.

[49] Nunzi, J.M. Organic photovoltaic materials and devices. *Comptes Rendus Physique*, 2002, **3**(4), 523-542.

[50] Hoppe, H., Sariciftci, N. S. Organic solar cells: An overview. *Journal of Materials Research*, 2004, **19**(7), 1924-1945.

[51] Khanam, J. J., Foo, S. Y. Modeling of high-efficiency multi-junction polymer and hybrid solar cells to absorb infrared light. *Polymers*, 2019, **11**(2), 383.

[52] Kietzke, T. Recent advances in organic solar cells. *Advances in OptoElectronics*, 2007, **2007**(1), 040285.

[53] Braun, D., Heeger, A. J. Visible light emission from semiconducting polymer diodes. *Applied Physics Letters*, 1991, **58**(18), 1982-1984.

[54] Miranda, P. B., Moses, D., Heeger, A. J. Ultrafast photogeneration of charged polarons in conjugated polymers. *Physical Review B*, 2001, **64**(8), 081201.

[55] Marks, R. N., Halls, J. J. M., Bradley, D. D. C., Friend, R. H., Holmes, A. B. The photovoltaic response in poly (p-phenylene vinylene) thin-film devices. *Journal of Physics: Condensed Matter*, 1994, **6**(7), 1379.

[56] Yu, G., Zhang, C., Heeger, A. J. Dual-function semiconducting polymer devices: Light-emitting and photodetecting diodes. *Applied Physics Letters*, 1994, **64**(12), 1540-1542.

[57] Chang, L., Sheng, M., Duan, L., Uddin, A. Ternary organic solar cells based on non-fullerene acceptors: A review. *Organic Electronics*, 2021, **90**, 106063.

[58] Brabec, C. J., Zerza, G., Cerullo, G., De Silvestri, S., Luzzati, S., Hummelen, J. C., Sariciftci, S. Tracing photoinduced electron transfer process in conjugated polymer/fullerene bulk heterojunctions in real time. *Chemical Physics Letters*, 2001, **340**(3-4), 232-236.

[59] Deibel, C., Strobel, T., Dyakonov, V. Role of the charge transfer state in organic donor-acceptor solar cells. *Advanced Materials*, 2010, **22**(37), 4097-4111.

[60] Andersson, V., Tvingstedt, K., Inganäs, O. Optical modeling of a folded organic solar cell. *Journal of Applied Physics*, 2008, **103**(9).

[61] Siebert-Henze, E., Lyssenko, V. G., Fischer, J., Tietze, M., Brueckner, R., Menke, T., Leo, K., Riede, M. Electroabsorption studies of organic pin solar cells: Increase of the built-in voltage by higher doping concentration in the hole transport layer. *Organic Electronics*, 2014, **15**(2), 563-568.

[62] Wang, Y., Lan, W., Li, N., Lan, Z., Li, Z., Jia, J., Zhu, F. Stability of nonfullerene organic solar cells: from built-in potential and interfacial passivation perspectives. *Advanced Energy Materials*, 2019, **9**(19), 1900157.

[63] Chen, B., Qiao, X., Liu, C.M., Zhao, C., Chen, H.C., Wei, K.-H., Hu, B. Effects of bulk and interfacial charge accumulation on fill factor in organic solar cells. *Applied Physics Letters*, 2013, **102**(19).

[64] Satpathy, R., Pamuru, V. Making of crystalline silicon solar cells. *Solar PV Power*, 2021, 71-134.

[65] Pivrikas, A., Sariciftci, N. S., Juškā, G., Osterbacka, R. A review of charge transport and recombination in polymer/fullerene organic solar cells. *Progress in Photovoltaics: Research and Applications*, 2007, **15**(8), 677-696.

[66] Mola, G. T., Ahmed, A. Y. A., Ike, J. N., Liu, M., Hamed, M. S. G., Zhang, Y. Engineering non-fullerene acceptors as a mechanism to control film morphology and energy loss in organic solar cells. *Energy & Fuels*, 2022, **36**(9), 4691-4707.

[67] Koster, L. J. A., Mihailetchi, V. D., Xie, H., Blom, P. W. M. Origin of the light intensity dependence of the short-circuit current of polymer/fullerene solar cells. *Applied Physics Letters*, 2005, **87**(20).

[68] Mihailetchi, V. D., Wildeman, J., Blom, P. W. M. Space-charge limited photocurrent. *Physical Review Letters*, 2005, **94**(12), 126602.

[69] Adler, D., 1971. Amorphous semiconductors. Critical Reviews in Solid State and Material

Sciences, *2(3)*, pp.317-465.

[70] Qi, B., Wang, J. Open-circuit voltage in organic solar cells. *Journal of Materials Chemistry*, 2012, **22**(46), 24315-24325.

[71] Steim, R., Kogler, F. R., Brabec, C. J. Interface materials for organic solar cells. *Journal of Materials Chemistry*, 2010, **20**(13), 2499-2512.

[72] Berredjem, Y., Bernede, J. C., Djobo, S. O., Cattin, L., Morsli, M., & Boulmokh, A. On the improvement of the efficiency of organic photovoltaic cells by the presence of an ultra-thin metal layer at the interface organic/ITO. *The European Physical Journal-Applied Physics*, 2008, **44**(3), 223–228. EDP Sciences.

[73] Sharma, A., Hotchkiss, P. J., Marder, S. R., & Kippelen, B. Tailoring the work function of indium tin oxide electrodes in electrophosphorescent organic light-emitting diodes. *Journal of Applied Physics*, 2009, **105**(8). AIP Publishing.

[74] Kim, J.H., Hong, J.A., Kwon, D.-G., Seo, J., & Park, Y. Energy level alignment in polymer organic solar cells at donor-acceptor planar junction formed by electrospray vacuum deposition. *Applied Physics Letters*, 2014, **104**(16). AIP Publishing.

[75] Bory, B. F., Rocha, P. R. F., Janssen, R. A. J., Gomes, H. L., De Leeuw, D. M., & Meskers, S. C. J. Lithium fluoride injection layers can form quasi-Ohmic contacts for both holes and electrons. *Applied Physics Letters*, 2014, **105**(12). AIP Publishing.

[76] Ogundele, A. K., & Mola, G. T. Semiconductor quantum dots as a mechanism to enhance charge transfer processes in polymer solar cells. *Chemosphere*, 2023, **345**, 140453. Elsevier.

[77] Shah, S. K., Hayat, K., & Ali, K. Effect of TiO_2 interlayer on the performance of inverted polymeric solar cells. *Materials Research Express*, 2019, **6**(6), 065102. IOP Publishing.

[78] Chang, Y.M., & Leu, C.Y. Conjugated polyelectrolyte and zinc oxide stacked structure as an interlayer in highly efficient and stable organic photovoltaic cells. *Journal of Materials Chemistry A*, 2013, **1**(21), 6446-6451. Royal Society of Chemistry.

[79] Kim, D. Y., Subbiah, J., Sarasqueta, G., So, F., Ding, H., Irfan, I., & Gao, Y. The effect of molybdenum oxide interlayer on organic photovoltaic cells. *Applied Physics Letters*, 2009, **95**(9). AIP Publishing.

[80] Kim, S., Saeed, M. A., Kim, S. H., & Shim, J. W. Enhanced hole selecting behavior of WO_3 interlayers for efficient indoor organic photovoltaics with high fill-factor. *Applied Surface Science*, 2020, **527**, 146840. Elsevier.

[81] Menke, S. M., Ran, N. A., Bazan, G. C., & Friend, R. H. Understanding energy loss in organic solar cells: toward a new efficiency regime. *Joule*, 2018, **2**(1), 25-35. Elsevier.

[82] Kaake, L. G., Jasieniak, J. J., Bakus, R. C., Welch, G. C., Moses, D., Bazan, G. C., & Heeger, A. J. Photoinduced charge generation in a molecular bulk heterojunction material. *Journal of the American Chemical Society*, 2012, **134**(48), 19828-19838. ACS Publications.

[83] Hodgkiss, J. M., Albert-Seifried, S., Rao, A., Barker, A. J., Campbell, A. R., Marsh, R. A., & Friend, R. H. Exciton-charge annihilation in organic semiconductor films. *Advanced Functional Materials*, 2012, **22**(8), 1567-1577. Wiley Online Library.

[84] Brédas, J.-L., Norton, J. E., Cornil, J., & Coropceanu, V. Molecular understanding of organic solar cells: the challenges. *Accounts of Chemical Research*, 2009, **42**(11), 1691-1699. ACS Publications.

[85] Tvingstedt, K., Vandewal, K., Zhang, F., & Inganäs, O. On the dissociation efficiency of charge transfer excitons and Frenkel excitons in organic solar cells: a luminescence quenching study. *The Journal of Physical Chemistry C*, 2010, **114**(49), 21824–21832. ACS Publications.

[86] Clarke, T. M., & Durrant, J. R. Charge photogeneration in organic solar cells. *Chemical Reviews*, 2010, **110**(11), 6736-6767. ACS Publications.

[87] Lee, J., Vandewal, K., Yost, S. R., Bahlke, M. E., Goris, L., Baldo, M. A., Manca, J. V., & Van Voorhis, T. Charge transfer state versus hot exciton dissociation in polymer-fullerene blended solar cells. *Journal of the American Chemical Society*, 2010, **132**(34), 11878-11880. ACS Publications.

[88] Street R. A. Localized state distribution and its effect on recombination in organic solar cells. *Physical Review B—Condensed Matter and Materials Physics*, 2011, **84**(7), 075208.

[89] Gurney, R.S., Lidzey, D.G. and Wang, T. A review of non-fullerene polymer solar cells: from device physics to morphology control. *Reports on Progress in Physics* , 2019, **82**(3), p.036601.

[90] Servaites J. D., Ratner M. A., Marks T. J. Organic solar cells: A new look at traditional models. *Energy & Environmental Science*, 2011, **4**(11), 4410-4422.

[91] Clarke T. M., Peet J., Nattestad A., Drolet N., Dennler G., Lungenschmied C., Leclerc M., Mozer A. J. Charge carrier mobility, bimolecular recombination and trapping in polycarbazole copolymer: fullerene (PCDTBT: PCBM) bulk heterojunction solar cells. *Organic*

Electronics, 2012, **13**(11), 2639-2646.

[92] Shuai Z., Geng H., Xu W., Liao Y., André J. M. From charge transport parameters to charge mobility in organic semiconductors through multiscale simulation. *Chemical Society Reviews*, 2014, **43**(8), 2662-2679.

[93] Zhou N., Facchetti A. Charge transport and recombination in organic solar cells (OSCs). In: *Organic and Hybrid Solar Cells*, Springer, 2014, pp 19-52.

[94] Wetzelaer G. J. A. H., Van der Kaap N. J., Koster L., Blom P. W. M. Quantifying bimolecular recombination in organic solar cells in steady state. *Advanced Energy Materials*, 2013, **3**(9).

[95] Kirchartz T., Pieters B. E., Kirkpatrick J., Rau U., Nelson J. Recombination via tail states in polythiophene: fullerene solar cells. *Physical Review B—Condensed Matter and Materials Physics*, 2011, **83**(11), 115209.

[96] Kirchartz T., Nelson J. Meaning of reaction orders in polymer: fullerene solar cells. *Physical Review B—Condensed Matter and Materials Physics*, 2012, **86**(16), 165201.

[97] Kemell M., Ritala M., Leskelä M. Thin film deposition methods for $CuInSe_2$ solar cells. *Critical Reviews in Solid State and Materials Sciences*, 2005, **30**(1), 1-31.

[98] Kouijzer S. Photoactive and interface layers in polymer solar cells. *Journal of Materials Chemistry*, 2014.

[99] Ghorab M., Fattah A., Joodaki M. Fundamentals of organic solar cells: A review on mobility issues and measurement methods. *Optik*, 2022, **267**, 169730.

[100] Azzouzi M., Kirchartz T., Nelson J. Factors controlling open-circuit voltage losses in organic solar cells. *Trends in Chemistry*, 2019, **1**(1), 49-62.

[101] Garcia A. S., Kristensen S. T., Strandberg R. Analytical modeling of the temperature sensitivity of the maximum power point of solar cells. *IEEE Journal of Photovoltaics*, 2022, **12**(5), 1237-1242.

[102] Nguyen B. P., Kim T., Park C. R. Nanocomposite-based bulk heterojunction hybrid solar cells. *Journal of Nanomaterials*, 2014, **2014**, 243041.

[103] Qi B., Wang J. Fill factor in organic solar cells. *Physical Chemistry Chemical Physics*, 2013, **15**(23), 8972-8982.

[104] Jao M. H., Liao H. C., Su W. F. Achieving a high fill factor for organic solar cells. *Journal*

of Materials Chemistry A, 2016, **4**(16), 5784-5801.

[105] Benanti T. L., Venkataraman D. Organic solar cells: An overview focusing on active layer morphology. *Photosynthesis Research*, 2006, **87**, 73-81.

Chapter 3

Surface plasmonic and Transition Metal Chalcogenides Nanoparticles

3.1 SPR and LSPR

The interaction between the electromagnetic fields of the incident radiation with surface electron plasma of the metal nano-particles leads to the surface plasmonic resonance (SPR). Where at this scale, the optical properties of nano-structured metals go through remarkable transformations due to the presence of SPR, leading to behaviors completely different from those observed in bulk metals. The surface plasmonic effect was initially discovered by Faraday in 1857 during his investigation of colloidal metal NPs. Where he defined it as the coherent oscillation of electrons propagating along the surface of a conductor [1]. Localized Surface Plasmon Resonance (LSPR) and SPR are two distinct forms of surface plasmon excitation. LSPRs arise from the collective oscillations of electrons confined locally by metal nano-structures. Where, their effect establishes from the localization of the electromagnetic field due to strong resonance effects, resulting in efficient light concentration. On the other hand, SPP is generated from the collective oscillations of electromagnetic waves at metal-dielectric interfaces. These waves are tightly bound near the surface of the conductor and decline away from the interface. They form when the electromagnetic field interacts with the collective motion of free electrons plasma in the metal. [2]. Today, LSPR offers a means to overcome the optical and electrical limitations of organic-based devices by amplifying, concentrating, and manipulating light at the nanoscale. The outstanding optical benefits of the SPR process originated from the collective oscillations of the free conductive electrons of the metal nanostructure as a response to the incident electromagnetic field of light [3]. Moreover, when a nanostructured metal is exposed to light, the E-field component of the EM wave induces an electrostatic force on the conduction electrons of the plasmonic metal NPs forcing them

to oscillate coherently on the NP surface while simultaneously undergoing the restoring force of the positive screened ion cores. However, as the electrons are still confined inside the NP, the negatively charged electrons cloud concentrate on one side, while positively charged nucleus on the opposite side of the electrons leading to the generation of electric dipole moment inside the metal nanostructure [4]. As the internal metal nanostructured electric field is opposite to that of the external incident light, the first one does force the electrons to return to their initial equilibrium position and the process continues in the form of oscillation as shown in Figure. 3.1(a). The greater electron dislocation means the greater electric dipole and restoring force. On one hand, when the electrons are moved from their initial position as well as the electric field, the resultant oscillation frequency of the electrons, in this case, is known as the resonant frequency, and the whole process is generally called SPR [5]. While in the other hand, once the light interacts with an MNP with a size much smaller than the incident electromagnetic wavelength, the resulting process creates a plasmonic oscillation localized in the vicinity of the MNP leading to the oscillating of conduction electrons at a certain frequency referred to as the LSPR [6]. The utilization of the promising plasmon-enhanced light harvesting strategy for plasmonic metallic NPs can be either located between interfaces [6] or within the buffer [8] or active layers [9] of organic photovoltaic (OPV) devices. Depending on their unique properties, the numerous applications of the plasmonic nanostructured materials have shown their usefulness in various areas such as light-emitting diodes [10], sensing [11], plasmofluidics [12], photodetectors [13], plasmonic water splitting [14], photocatalysis [15], and photovoltaics [16]. For example, in the light PV application of plasmonic, researchers in this area have dedicated significant attention to investigating the interaction between light and metallic nanostructures to further enhance many processes within the solar cell device. Commonly, the incorporations of SPR and LSPR into the PV devices have been intended to address several issues including light absorption, charge generation, charge transport, and collection efficiency. For example, the utilization of optical properties of the SPR and LSPR through the PV devices are generally based on the synergistic interaction between metallic nanostructures and the semiconductor layers responsible for energy conversion. Thus, understanding the plasmonic enhancement mechanisms was based on the study of the behavior and dynamics at the interfaces of metal-semiconductors [17].

The rate of absorption and scattering through LSPR is highly dependent on the shape and size of NPs as well as the permittivity of both metal NP ($\varepsilon_{(\omega)}$ and the surrounding medium (ε_d). For example, the absorption cross-section (σ_{abs}) and scattering cross-section (σ_{sca}) for spherical metal NPs having a diameter less than the incident depth of electromagnetic light are evaluated by cross-section (σ_{ext}) and quasi-static approximation as shown in the equations below:

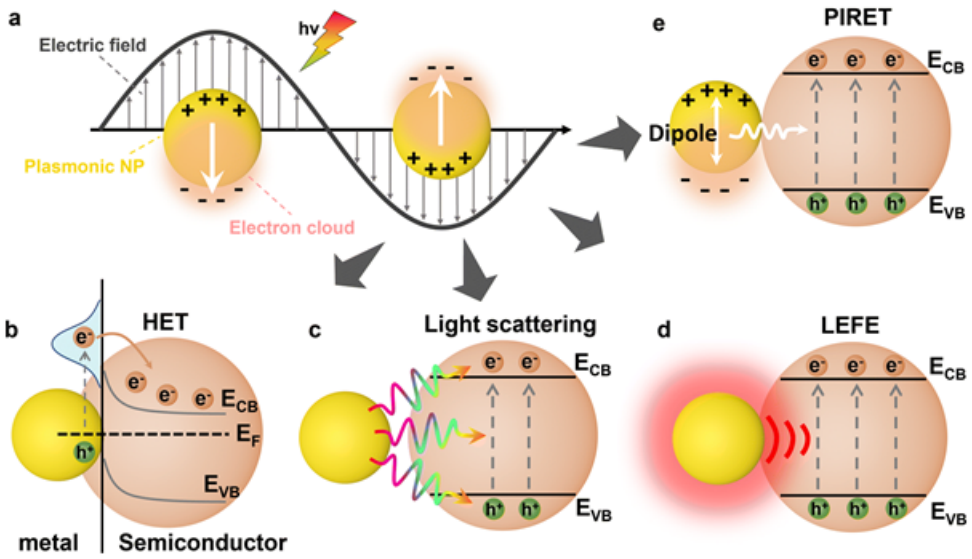

Figure 3.1: The schematic depiction of (a) the localized surface plasmon resonance effect, (b) the hot electron transfer mechanism, (c) plasmonic far field light scattering, (d) the localized electric field enhancement process mechanism, and (e) plasmon-induced resonance energy transfer [18].

$$\sigma_{ext}(\omega) = \sigma_{abs} + \sigma_{sca} \tag{3.1}$$

The polarization (α) of a plasmonic NP is essential in determining its absorption and scattering cross-sections, as these properties are influenced by the ability of these NPs to interact with and polarize in response to an oscillating incident electromagnetic field. Moreover, when the plasmonic metal NP is embedded in a medium with permittivity of (ε_d), the dielectric function of metal NP ($\varepsilon_{(\omega)}$) can determine the induced dipole moment. In this case, the polarizability is generally used to quantify the strength of the induced dipole moment

$$\alpha = 4\pi a^3 \frac{\varepsilon(\omega) - \varepsilon_d}{\varepsilon(\omega) + 2\varepsilon_d}. \tag{3.2}$$

Where, a is the radius of plasmonic NP. Then the corresponding cross sections for scattering and absorption σ_{abs} and σ_{sca} can be calculated via:

$$\sigma_{abs} = kIm[\alpha] = 4\pi k a^3 Im\left[\frac{\varepsilon(\omega) - \varepsilon_d}{\varepsilon(\omega) + 2\varepsilon_d}\right] \tag{3.3}$$

$$\sigma_{sca} = \frac{k^4}{6\pi}[\alpha]^2 = 8\frac{\pi}{3}k^4 a^6 \left[\frac{\varepsilon(\omega) - \varepsilon_d}{\varepsilon(\omega) + 2\varepsilon_d}\right]^2 \tag{3.4}$$

Where, a wave vector k = 2 π/λ, [19]. For small NPs where their radius are much smaller than λ, the efficiency of absorption process a^3 is higher than that of the scattering process a^6. While for larger size of NPs (the radius approximately equal to λ), the scattering cross-section scaling a^6 becomes more dominant than absorption cross-section scaling with a^3.

The permittivity of the plasmonic NP $\varepsilon_{(\omega)}$ in equations (3.3) and (3.4) is expressed as a combination between real and imaginary components. The real part, often indicates the resonance peak. While the imaginary part provides information about the de-phasing. The total NP permittivity is calculated as shown below:

$$\varepsilon(\omega) = \varepsilon_r(\omega) + i\varepsilon_i(\omega) \tag{3.5}$$

$$\varepsilon(\omega) = 1 - \frac{\varepsilon_p^2}{\omega(\omega + \gamma_b)} \tag{3.6}$$

The parameters γ_b and ε_p known as the damping constant and the frequency of plasmonic NP respectively, where they represented as:

$$\gamma_b = \frac{\nu_F}{I_m} \tag{3.7}$$

Where ν_F is the Fermi velocity of free electrons in the metal and I_m is the mean free path of the electrons.

$$\varepsilon_p^2 = \frac{Ne^2}{\varepsilon_0 m} \tag{3.8}$$

Where, N, m, e, ε_0 are the density of electrons, mass of the electron, charge of the electron, and the permittivity of the free space respectively. The oscillation frequency of the plasmonic resonance is critical in determining the resonance SPR. This frequency is influenced by four key factors including Effective electron mass, Density of electrons, Shape of the NP, and Size of the charge distribution [22, 20, 21].

3.2 Plasmonic for Enhanced Collection Photocurrent

Plasmonic energy can be achieved through various SPR mechanisms (see Figure. 3.1), including far-field scattering effects, near-field localized, hot energy transfer, and dipole-dipole coupling energy transfer. The enhancement of optical absorption via the far-field scattering effect arises from the increased optical path of incident photons and reduced reflection at illuminated surfaces. Near-field SPR effects increase

the exciton dissociation rate by providing a strong electric field near the area of plasmonic NP. In the case of hot energy transfer mechanism, a hot electrons produced by plasmonic NPs can be directly injected into the conduction band of neighboring semiconductor polymers. Lastly, in plasmonic dipole-dipole coupling, the energy of a plasmonic oscillation is transferred from a plasmonic NP to a semiconductor polymer through either electromagnetic field interactions or dipole-dipole interactions. Each mechanism mentioned above for enhancing OSCs requires careful control over the shapes (see Figure. 3.2), sizes, and locations of nanoparticles, as well as a rational selection of the material's nature, including its dielectric constant [23, 24].

3.2.1 Near-Field Effect

The nature of LSPR involves the non-propagating excitation of electrons limited within a plasmonic metallic NP. When LSPR arises, the electrons within the metallic NPs undergo collective oscillations in response to incident light, resulting in significantly strengthened electric fields near the NP surfaces as shown in Figure. 3.1(d) [25]. This enhancement mechanism mostly contributes to influencing the exciton dissociation process within the surrounding semiconductor by providing an electric field of the LSPR much stronger than that of incident light. The exciton dissociation efficiency, in this case, is highly dependent on the LSPR electromagnetic field concentration near the area of the semiconductor. Hence, the exciton generation amount inside the semiconductor arises as the electric field intensity increases [26]. Additionally, the probability of exciton dissociations in a semiconductor medium, which is influenced by LSPR, also arises as the intensity of the plasmonic electric field increases, leading to further efficient utilization of the free charge carriers. Generally, these two characteristics of LSPR near field effect are usually referred to as the Localized electromagnetic field enhancement (LEFE) effect of LSPR [18].

3.2.2 Far Field Scattering

Depending on the mechanism by which absorption is enhanced, the scattering phenomenon is generally called light trapping or a far-field effect, as indicated in Figure. 3.1(C). Where the plasmonic NPs effectively scatter incident photons into the surrounding medium, with the scattering properties mostly depending upon the morphology of the metal particles [27, 28]. According to the observation regarding the optical enhancement using metal NPs, the scattering effect is most dominant in NPs with sizes exceeding 50 nm, while for smaller NPs (approximately 50 nm and below), the absorption process is the dominant phenomenon [24].

This effect is usually optimized by balancing the incident power density and mitigating transmission losses, especially in thin-film devices. To achieve this, light is often directed perpendicularly onto the

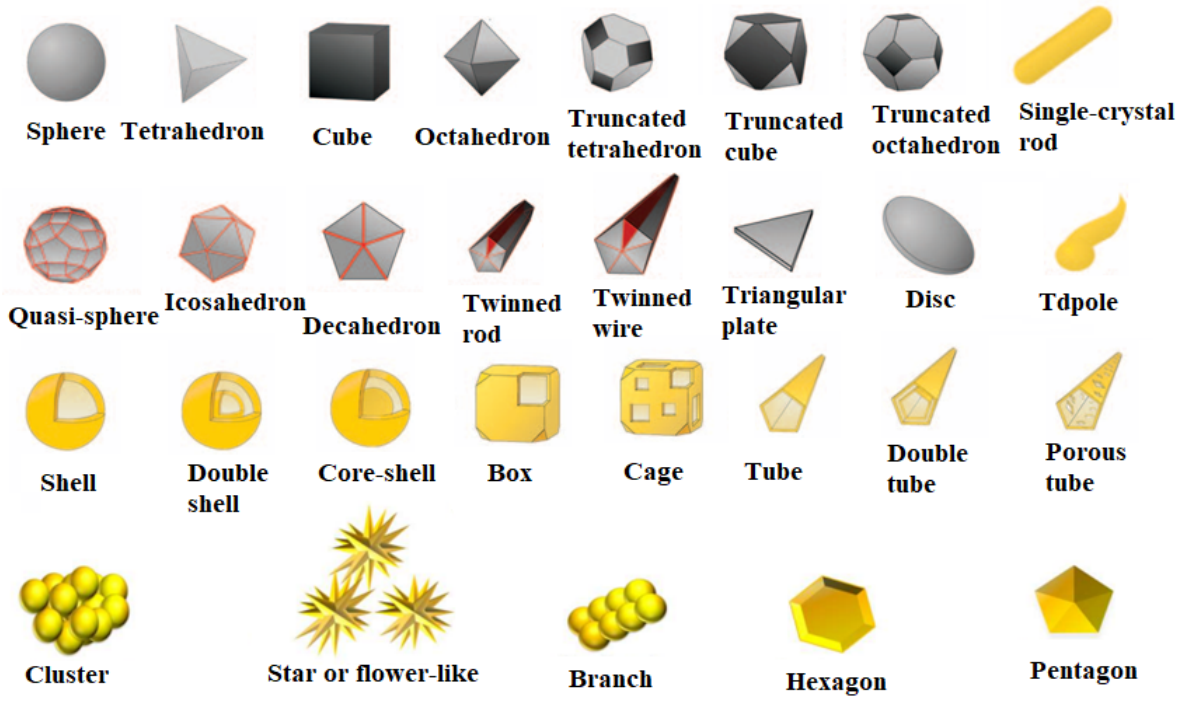

Figure 3.2: T. a schematic representation of various plasmonic nanoparticle shapes [1, 2].

surface to maximize its interaction with the NPs thereby reducing the loss of photons. Moreover, once photons are scattered at the front surface, they travel a longer optical path compared to the thickness of the active layer, increasing the chances of optical absorption. In the case of spherical NPs, the scattering behaviour generally depends on their size. Hence, smaller NPs (much smaller than the wavelength of light) tend to scatter more efficiently in the forward direction, facilitating enhanced light penetration into the active layer. Larger NPs, (comparable to or larger than the wavelength) show increased backscattering, which can redirect photons toward the light source in a process similar to reflection [29, 30]. It is possible to control the direction of scattering by adjusting the size of plasmonic NPs as well as their positions within the device. For instance, when NPs with small diameters are located at the top of the active layer, they can change the arriving photons at a certain angle usually lower than 90 degrees, thereby increasing their possibility of absorption [31]. Another possible case also arises when plasmonic NPs are placed at the lowest surface of the active layer, they allow the unabsorbed photons to be scattered back into the active layer, enhancing their chances of absorption. On the other hand, employing NPs together at both sides of the active layer enables unabsorbed photons to undergo repeated reflection within the active layer until they are fully absorbed [32, 33]. Generally, irrespective of the scattering path, many scattering actions are predicted to increase the utilization of the light by the photovoltaic device.

3.2.3 Hot Electron Transfer Mechanism

This mechanism is also known as the LSPR-sensitization effect, where hot electrons generated by plasmonic NPs can be directly injected into the conduction band of neighbouring semiconductor polymers. This mechanism was well explained by Zhang et al, through their investigations on LSPR applications in photo-catalysts. Their study was focused on utilizing plasmonic-metal/n-type-semiconductor systems with direct contact. Their observations indicated that a persistent Fermi–Dirac distribution of electron states is established within the volume of the metal NP following the excitation of LSPR of plasmonic metal NP by incident light leading to upshifting of electronic energy states of plasmonic metal NP. As a result, a hot electron is injected into the conduction band of the neighbouring semiconductor (see Figure 3.1(b)). Later, the electron states in the plasmonic NP return to the Fermi–Dirac distribution with a higher Fermi level through electron-electron relaxation. In this situation, electrons having greater energy than the Fermi level can easily migrate to the CB of the neighbouring semiconductor. As soon as the energy of the surface plasmon decays, the standard Fermi–Dirac distribution of electrons is re-established [34]. According to Zhang et al, this mechanism is only available for those plasmonic NPs in direct contact with the semiconductor molecules forming a Schottky barrier with the work function of the plasmonic material either higher than that of an n-type semiconductor or lower than that of a p-type semiconductor. The hot electron injection process suggests that the amount of excited hot electrons with energy greater than the Schottky barrier determines the efficiency of hot-electron injection [35]. Therefore, factors such as the size, shape, and intrinsic properties of plasmonic NPs, along with the electrochemical properties of surrounding semiconductors molecules play an essential role in influencing the hot-electron-injection process [36].

3.2.4 Dipole-Dipole Coupling

The plasmonic dipole-dipole coupling or plasmon-induced resonance energy transfer (PIRET) mechanism can be understood as the process by which the energy of a plasmonic oscillation is transferred from a plasmonic NP to a neighbouring semiconductor molecule through either an electromagnetic field or via a dipole-dipole interaction as shown in figure. 3.1(e) [37]. This mechanism was primarily established to facilitate exciton dissociation within a semiconductor material using the internal electromagnetic field generated by surface plasmons. The intensity of the LSPR-induced electromagnetic field near plasmonic metals is stronger than that of the incident photons. Consequently, plasmonic materials can be considered as concentrators that amplify the intensity of the near-field electromagnetic resonance during the plasmonic-enhanced process via plasmon-resonance energy transfer [38]. The PIRET mechanism facilitates energy transfer from plasmonic NPs to neighbouring semiconductor (1 to 10 nanometers) medium through either by an electromagnetic field or dipole-dipole interactions. This process enhances

electronic excitations near or below the semiconductor band edge due to the strong electromagnetic field generated by LSPR. In this mechanism, the plasmonic NPs perform as the energy donors, similar to the fluorescent donors in Förster resonance energy transfer (FRET). The condition for PRET to occur in materials are that the polymer must be in close proximity of the plasmon for the interaction to be significant. Moreover, there must be spectral overlap between the plasmonic resonance edge and the threshold for optical absorption in the semiconductor. These points are not well cited here please edit where appropriate. The utilization of plasmon enhancement in OSCs through the PRET mechanism is usually controlled by the morphology, and composition of metal NPs, as well as the distance separating between metal NP and the semiconductor material [39].

3.3 Transition Metal Chalcogenides

Transition metal chalcogenides (TMCs) are formed when combining transition metals and group 16 elements such as sulfur, selenium, and tellurium. These TMCs have increased researchers' attention in various areas due to their tunable electrical, optical, and magnetic properties [40]. The structural diversity and electronic behaviors of these materials allow them to be useful in numerous fields, including PVs, catalysis, sensors, and energy storage devices. Their flexibility originates from the partially filled d orbitals of transition metals, facilitating the creation of compounds like metal sulfides, selenides, and tellurides with varying degrees of semiconducting behavior. Moreover, Additionally, the directional nature of p-bonds in chalcogenide elements also influences their band structure, charge transport, and optical properties [41, 42]. Additionally, the chemical flexibility of TMCs allows for further chemical modifications, such as doping alloying, and is feasible to expand the range of optical and electronic properties. The relationship between their size, morphology, and composition offers a wide range of possible configurations, which can significantly impact the performance of devices incorporating TMCs [43].

3.3.1 Chalcogenide Transition Metal Quantum Dots

One of the most outstanding phenomena observed in nano-structured TMCs is the quantum confinement effect, which occurs when the size of a material is reduced to dimensions close to or smaller than the exciton Bohr radius (approximately below 10 nano-meters). This phenomenon leads to separate energy levels, unlike the continuous energy bands found in bulk materials. The result is a size-dependent band gap, where smaller particles have wider band gaps due to the spatial restriction of electron-hole pairs (excitons) [44]. As illustrated in Figure. 3.3. the quantum confinement effect of the TMCs can be controlled by adjusting the dimensions of the NPs. For example, when the size of NPs is reduced,

the resultant band gap tends to be wide, shifting the optical properties into the higher frequencies of the electromagnetic spectrum. This size-dependent behavior is very important for optimizing the optical absorption over a wide range of wavelengths is needed for effective solar energy conversion [45]. Moreover, when TMCs NPs are reduced in size, the quantum confinement effect not only increases the band gap but also enhances the photo-stability and absorption coefficient. These properties are very important for thin film solar cells, as the increased band gap allows for better control over light absorption and electron transport.

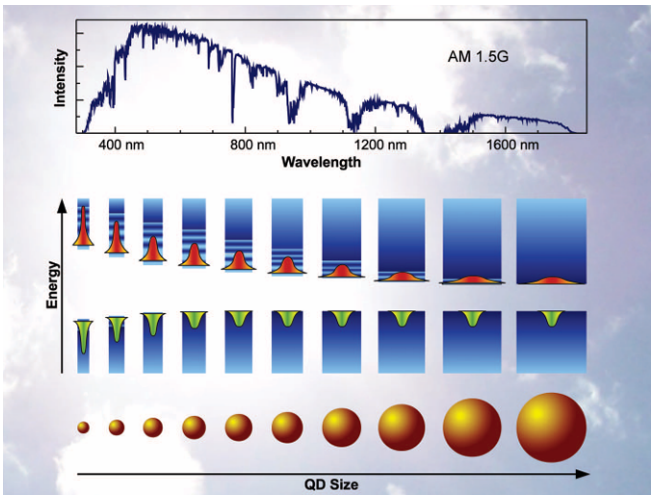

Figure 3.3: demonstrate the effect of size of NP on the energy gap and absorption area [45].

Additionally, the enhanced surface-to-volume ratio in quantum-confined nano-structures provides extra active sites for light absorption and exciton generation, further improving the performance of photovoltaic devices [46]. For example, in quantum dot solar cells, the employment of the TMC quantum dots facilitates a broader absorption spectrum due to the tune-ability of the band gap. This flexibility allows for better matching of the material's absorption with the solar spectrum and then improving the efficiency of the solar cell [47]. Furthermore, the quantum confinement effect also enhances the generation of multiple excitons per photon, which can significantly increase the photo-current and PCE in thin film solar cells. In quantum-confined NPs like quantum dots, the absorption of a single high-energy photon (with energy higher two times than the band gap energy) can produce multiple electron-hole pairs. This process is generally known as multiple exciton generation (MEG). The multiple exciton generation occurs more efficiently in quantum dots due to enhance Coulomb interactions and altered energy relaxation pathways caused by quantum confinement [48, 49].

3.3.2 The Effect of Quantum Confinement in TFSCs

The quantum confinement effect can influence both the optical and electrical properties of TMCs, making them highly relevant for improving the performance of thin film solar cells. As mentioned previously, the fundamental mechanism by which quantum confinement property enhances the solar cell device efficiency takes place through band gap modification. Thus, by finely controlling the nano-structures of TMCs, it is possible to tune the band gap to optimize light harvesting capacity and charge carrier generation ratio in thin film solar cells [50]. For example, by incorporating quantum dots NPs with a certain band gap into the active layer of a thin film solar cell, it is possible to improve light absorption across a wider range of wavelengths, leading to more efficient utilization of the solar spectrum [51]. Thus the confinement of excitons within these NPs increases the probability of exciton dissociation into free charge carriers, which can then be successfully collected at the electrodes [52]. Additionally, the size-dependent electronic properties of TMCs quantum-confined provide opportunities to reduce recombination losses of the thin film solar cells. Hence the adaptable energy levels resulting from quantum confinement assist in separating charge carriers thus reducing the probability of electron-hole recombination [53, 54, 55]. Generally, the quantum confinement property and the band gap tenability provide a great approach for optimizing the thin film solar cell device performance.

3.3.3 The Morphology Control of TMCs

The structural and morphological characteristics of TMCs play a fundamental role in determining their optical and electrical properties. By controlling the synthesis parameters, such as reaction temperature, precursor concentration, and chemical agents, it is possible to obtain nano-structures with specific shapes and sizes, influencing their quantum confinement effects. By using different synthesis methods, several nano-structured morphologies based on TMCs can be achieved, such as nano-sheets, nano-sphere, nano-rods, and nano-wires with different degrees of confinement depending on their dimensionality [56, 57]. For example, nano-sheets exhibit strong in-plane quantum confinement, with their large horizontal dimensions and very thin side view, which can provide the possibility to change their electronic and optical behavior [58]. On the other hand, nano-rods and nano-wires confine excitons in two dimensions, leading to different band gap placements and optical absorption characteristics. Moreover, the morphology of TMCs can also influence their electrical properties. For example, nano-structure-based TMCs with high surface area and well-defined crystallinity provide more active sites for charge transfer, improving the charge collection efficiency in solar devices [59, 60]. Generally, the facility to control the morphology of TMCs provides additional options to exploit the quantum confinement property in thin film solar cells by designing nano-structures with specific shapes and sizes.

References

[1] Faraday M. X. The Bakerian Lecture.—Experimental relations of gold (and other metals) to light. *Philosophical Transactions of the Royal Society of London*, 1857, **147**, 145-181.

[2] Chou C. H., Chen F. C. Plasmonic nanostructures for light trapping in organic photovoltaic devices. *Nanoscale*, 2014, **6**(15), 8444-8458.

[3] Jain P. K., El-Sayed M. A. Plasmonic coupling in noble metal nanostructures. *Chemical Physics Letters*, 2010, **487**(4-6), 153-164.

[4] Singh S., Singh P. K., Umar A., Lohia P., Albargi H., Castañeda L., Dwivedi D. K. 2D nanomaterial-based surface plasmon resonance sensors for biosensing applications. *Micromachines*, 2020, **11**(8), 779.

[5] García M. A. Surface plasmons in metallic nanoparticles: fundamentals and applications. *Journal of Physics D: Applied Physics*, 2011, **44**(28), 283001.

[6] Willets K. A., Van Duyne R. P. Localized surface plasmon resonance spectroscopy and sensing. *Annu. Rev. Phys. Chem.*, 2007, **58**(1), 267-297.

[7] Fleetham T., Choi J. Y., Choi H. W., Alford T., Jeong D. S., Lee T. S., Lee K. S., Li J., Kim I. Photocurrent enhancements of organic solar cells by altering dewetting of plasmonic Ag nanoparticles. *Scientific Reports*, 2015, **5**(1), 14250.

[8] Su Z., Wang L., Li Y., Zhang G., Zhao H., Yang H., Ma Y., Chu B., Li W. Surface plasmon enhanced organic solar cells with a MoO_3 buffer layer. *ACS Applied Materials & Interfaces*, 2013, **5**(24), 12847-12853.

[9] Shen H., Bienstman P., Maes B. Plasmonic absorption enhancement in organic solar cells with thin active layers. *Journal of Applied Physics*, 2009, **106**(7).

[10] Gu X., Qiu T., Zhang W., Chu P. K. Light-emitting diodes enhanced by localized surface plasmon resonance. *Nanoscale Research Letters*, 2011, **6**, 1-12.

[11] Szunerits S., Boukherroub R. Sensing using localised surface plasmon resonance sensors. *Chemical Communications*, 2012, **48**(72), 8999-9010.

[12] Patra P. P., Chikkaraddy R., Tripathi R. P. N., Dasgupta A., Kumar G. V. P. Plasmofluidic single-molecule surface-enhanced Raman scattering from dynamic assembly of plasmonic nanoparticles. *Nature Communications*, 2014, **5**(1), 4357.

[13] Berini P. Surface plasmon photodetectors and their applications. *Laser & Photonics Reviews*, 2014, **8**(2), 197-220.

[14] Huang Y. S., Hsiao Y. C., Tzeng S. H., Wu Y. H., Perng T. P., Lu M. Y., Chueh Y. L., Chen L. J. Vastly improved solar-light induced water splitting catalyzed by few-layer MoS_2 on Au nanoparticles utilizing localized surface plasmon resonance. *Nano Energy*, 2020, **77**, 105267.

[15] Hou W., Cronin S. B. A review of surface plasmon resonance-enhanced photocatalysis. *Advanced Functional Materials*, 2013, **23**(13), 1612-1619.

[16] Pillai S., Green M. A. Plasmonics for photovoltaic applications. *Solar Energy Materials and Solar Cells*, 2010, **94**(9), 1481-1486.

[17] Jang Y. H., Jang Y. J., Kim S., Quan L. N., Chung K., Kim D. H. Plasmonic solar cells: from rational design to mechanism overview. *Chemical Reviews*, 2016, **116**(24), 14982-15034.

[18] Ye Z., Xu Z., Yue W., Liu X., Wang L., Zhang J. Exploiting the LSPR effect for an enhanced photocatalytic hydrogen evolution reaction. *Physical Chemistry Chemical Physics*, 2023, **25**(4), 2706-2716.

[19] Hu M., Chen J., Li Z. Y., Au L., Hartland G. V., Li X., Marquez M., Xia Y. Gold nanostructures: engineering their plasmonic properties for biomedical applications. *Chemical Society Reviews*, 2006, **35**(11), 1084-1094.

[20] Maier, S.A. and Maier, S.A., 2007. Surface plasmon polaritons at metal/insulator interfaces. Plasmonics: Fundamentals and Applications, pp.21-37.

[21] Locarno, M. and Brinks, D., 2023. Analytical calculation of plasmonic resonances in metal nanoparticles: A simple guide. *American Journal of Physics*, 91(7), pp.538-538.

[22] Murray W. A., Barnes W. L. Plasmonic materials. *Advanced Materials*, 2007, **19**(22), 3771-3782. Wiley Online Library.

[23] Alkhalayfeh M. A., Aziz A. A., Pakhuruddin M. Z. An overview of enhanced polymer solar cells with embedded plasmonic nanoparticles. *Renewable and Sustainable Energy Reviews*,

2021, **141**, 110726.

[24] Uddin A., Yang X. Surface plasmonic effects on organic solar cells. *Journal of Nanoscience and Nanotechnology*, 2014, **14**(2), 1099-1119.

[25] Feng L., Niu M., Wen Z., Hao X. Recent advances of plasmonic organic solar cells: Photophysical investigations. *Polymers*, 2018, **10**(2), 123.

[26] Wu X., Jaatinen E., Sarina S., Zhu H. Y. Direct photocatalysis of supported metal nanostructures for organic synthesis. *Journal of Physics D: Applied Physics*, 2017, **50**(28), 283001.

[27] Callahan D. M., Munday J. N., Atwater H. A. Solar cell light trapping beyond the ray optic limit. *Nano Letters*, 2012, **12**(1), 214-218.

[28] Eustis S., El-Sayed M. A. Why gold nanoparticles are more precious than pretty gold: noble metal surface plasmon resonance and its enhancement of the radiative and nonradiative properties of nanocrystals of different shapes. *Chemical Society Reviews*, 2006, **35**(3), 209-217.

[29] Mokkapati S., Beck F. J., De Waele R., Polman A., Catchpole K. R. Resonant nanoantennas for light trapping in plasmonic solar cells. *Journal of Physics D: Applied Physics*, 2011, **44**(18), 185101.

[30] Ferry V. E., Verschuuren M. A., Li H. B. T., Verhagen E., Walters R. J., Schropp R. E. I., Atwater H. A., Polman A. Light trapping in ultrathin plasmonic solar cells. *Optics Express*, 2010, **18**(102), A237-A245.

[31] Lee Y. Y., Ho W. J., Liu J. J., Lin C. H. Light-trapping performance of silicon thin-film plasmonics solar cells based on indium nanoparticles and various TiO_2 space layer thicknesses. *Japanese Journal of Applied Physics*, 2014, **53**(6S), 06JE11.

[32] Tan H., Santbergen R., Smets A. H. M., Zeman M. Plasmonic light trapping in thin-film silicon solar cells with improved self-assembled silver nanoparticles. *Nano Letters*, 2012, **12**(8), 4070-4076.

[33] Morawiec S., Mendes M. J., Filonovich S. A., Mateus T., Mirabella S., Águas H., Ferreira I., Simone F., Fortunato E., Martins R. et al. Broadband photocurrent enhancement in a-Si:H solar cells with plasmonic back reflectors. *Optics Express*, 2014, **22**(104), A1059-A1070.

[34] Zhang X., Chen Y. L., Liu R. S., Tsai D. P. Plasmonic photocatalysis. *Reports on Progress in Physics*, 2013, **76**(4), 046401.

[35] Zhang P., Wang T., Gong J. Mechanistic understanding of the plasmonic enhancement for

solar water splitting. *Advanced Materials*, 2015, **27**(36), pp 5328-5342.

[36] Ma X.C., Dai Y., Yu L., Huang B.-B. Energy transfer in plasmonic photocatalytic composites. *Light: Science & Applications*, 2016, **5**(2), pp e16017-e16017.

[37] Liu S., Sun Y., Chen L., Zhang Q., Li X., Shuai J. A review on plasmonic nanostructures for efficiency enhancement of organic solar cells. *Materials Today Physics*, 2022, **24**, pp 100680.

[38] Zheng Z., Huang B.-B., Qin X., Zhang X.-Y., Dai Y., Whangbo M.-H. Facile in situ synthesis of visible-light plasmonic photocatalysts M@ TiO_2 (M= Au, Pt, Ag) and evaluation of their photocatalytic oxidation of benzene to phenol. *Journal of Materials Chemistry*, 2011, **21**(25), pp 9079-9087.

[39] Erwin W. R., Zarick H. F., Talbert E. M., Bardhan R. Light trapping in mesoporous solar cells with plasmonic nanostructures. *Energy & Environmental Science*, 2016, **9**(5), pp 1577-1601.

[40] Yadav S., Yashas S. R., Shivaraju H. P. Transitional metal chalcogenide nanostructures for remediation and energy: a review. *Environmental Chemistry Letters*, 2021, **19**(5), pp 3683–3700.

[41] Kharboot L. H., Fadil N. A., Bakar T. A. A., Najib A. S. M., Nordin N. H., Ghazali H. A review of transition metal sulfides as counter electrodes for dye-sensitized and quantum dot-sensitized solar cells. *Materials*, 2023, **16**(7), pp 2881.

[42] Fernando A., Weerawardene K. L. D. M., Karimova N. V., Aikens C. M. Quantum mechanical studies of large metal, metal oxide, and metal chalcogenide nanoparticles and clusters. *Chemical Reviews*, 2015, **115**(12), pp 6112-6216.

[43] Gopika M. S., Pillai S. S. Impact of morphology on the magnetic and optical properties of cobalt sulfide. *Journal of Materials Research*, 2023, **38**(8), pp 2097-2111.

[44] Shen S., Wang Q. Rational tuning the optical properties of metal sulfide nanocrystals and their applications. *Chemistry of Materials*, 2013, **25**(8), pp 1166–1178.

[45] Ruhle S., Shalom M., Zaban A. Quantum-dot-sensitized solar cells. *ChemPhysChem*, 2010, **11**(11), pp 2290-2304.

[46] Feng Y., Marusak K. E., You L., Zauscher S. Biosynthetic transition metal chalcogenide semiconductor nanoparticles: Progress in synthesis, property control and applications. *Current Opinion in Colloid & Interface Science*, 2018, **38**, pp 190-203.

[47] Rhee J. H., Chung C.C., Diau E. W.G. A perspective of mesoscopic solar cells based on metal chalcogenide quantum dots and organometal-halide perovskites. *NPG Asia Materials*, 2013, **5**(10), pp e68-e68.

[48] Nozik A. J. Multiple exciton generation in semiconductor quantum dots. *Chemical Physics Letters*, 2008, **457**(1-3), pp 3-11.

[49] Beard M. C. Multiple exciton generation in semiconductor quantum dots. *The Journal of Physical Chemistry Letters*, 2011, **2**(11), pp 1282-1288.

[50] Mohammed M. K. A. Studying the structural, morphological, optical, and electrical properties of CdS/PbS thin films for photovoltaic applications. *Plasmonics*, 2020, **15**(6), pp 1989-1996.

[51] Ogundele, A. K., & Mola, G. T. Semiconductor quantum dots as a mechanism to enhance charge transfer processes in polymer solar cells. *Chemosphere*, 2023, **345**, 140453. Elsevier.

[52] Ogundele A. K., Mola G. T. Ternary atoms alloy quantum dot assisted hole transport in thin film polymer solar cells. *Journal of Physics and Chemistry of Solids*, 2022, **171**, pp 110999.

[53] Shang Q., Kaledin A. L., Li Q., Lian T. Size dependent charge separation and recombination in $CsPbI_3$ perovskite quantum dots. *The Journal of Chemical Physics*, 2019, **151**(7).

[54] Nagaoka H., Colbert A. E., Strein E., Janke E. M., Salvador M., Schlenker C. W., Ginger D. S. Size-dependent charge transfer yields in conjugated polymer/quantum dot blends. *The Journal of Physical Chemistry C*, 2014, **118**(11), pp 5710–5715.

[55] Yuan M., Zhang X., Kong J., Zhou W., Zhou Z., Tian Q., Meng Y., Wu S., Kou D. Controlling the band gap to improve open-circuit voltage in metal chalcogenide based perovskite solar cells. *Electrochimica Acta*, 2016, **215**, pp 374-379.

[56] Kumar N. Synthesis and Characterization of Nano-Engineered Chalcogen Materials for Environmental and Biomedical Applications. University of Johannesburg (South Africa), 2017.

[57] Zhu J.J., Wang H. Synthesis of metal chalcogenide nanoparticles. In: *Encyclopedia of nanoscience and nanotechnology*, vol. 10, pp 347-367. American Scientific Publishers Stevenson Ranch, CA, USA, 2004.

[58] Jha A., Sharma G., Scott A. J. Fabrication and characterisation of two-dimensional transition metal dichalcogenides for applications in nano devices and spintronics. CRC Press,

2021.

[59] Berends A. C., de Mello Donega C. Ultrathin one-and two-dimensional colloidal semiconductor nanocrystals: pushing quantum confinement to the limit. *The Journal of Physical Chemistry Letters*, 2017, **8**(17), pp 4077-4090.

[60] Dai M., Wang R. Synthesis and applications of nanostructured hollow transition metal chalcogenides. *Small*, 2021, **17**(29), pp 2006813.

Chapter 4

Silver decorated magnesium doped photoactive layer for improved collection of photo-generated current in polymer solar cell

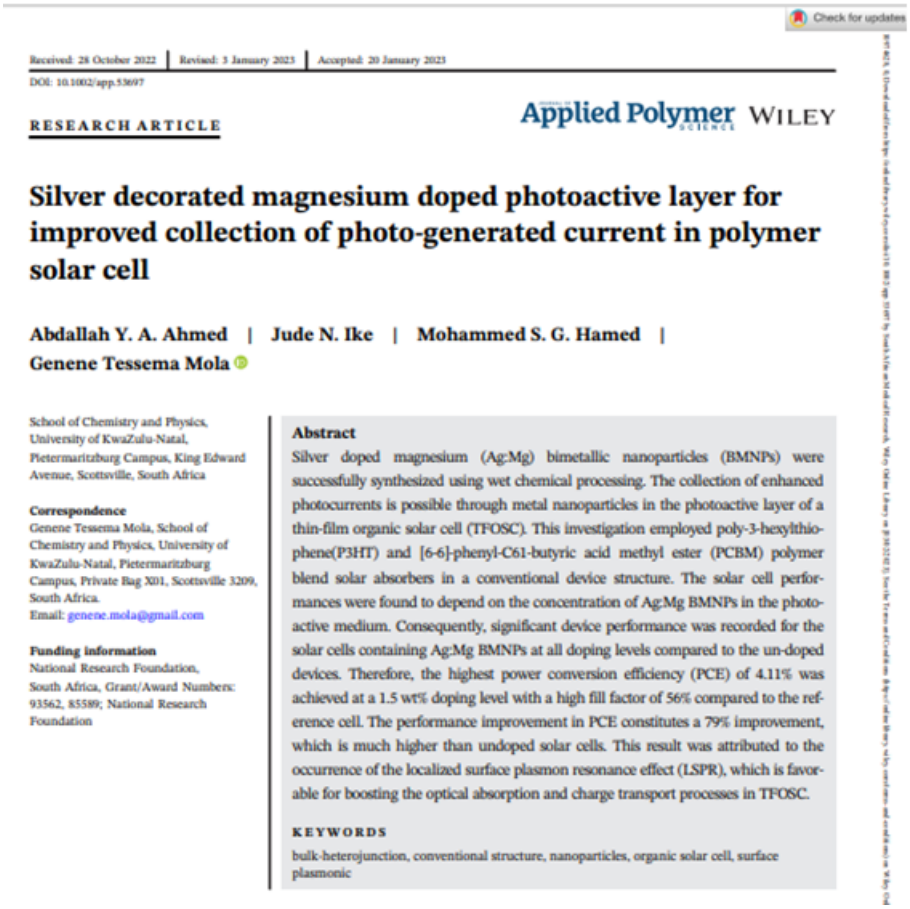

Received: 28 October 2022 | Revised: 3 January 2023 | Accepted: 20 January 2023
DOI: 10.1002/app.53697

RESEARCH ARTICLE

Applied Polymer WILEY

Silver decorated magnesium doped photoactive layer for improved collection of photo-generated current in polymer solar cell

Abdallah Y. A. Ahmed | Jude N. Ike | Mohammed S. G. Hamed | Genene Tessema Mola

School of Chemistry and Physics, University of KwaZulu-Natal, Pietermaritzburg Campus, King Edward Avenue, Scottsville, South Africa

Correspondence
Genene Tessema Mola, School of Chemistry and Physics, University of KwaZulu-Natal, Pietermaritzburg Campus, Private Bag X01, Scottsville 3209, South Africa.
Email: genene.mola@gmail.com

Funding information
National Research Foundation, South Africa, Grant/Award Numbers: 93562, 85589; National Research Foundation

Abstract
Silver doped magnesium (Ag:Mg) bimetallic nanoparticles (BMNPs) were successfully synthesized using wet chemical processing. The collection of enhanced photocurrents is possible through metal nanoparticles in the photoactive layer of a thin-film organic solar cell (TFOSC). This investigation employed poly-3-hexylthiophene(P3HT) and [6-6]-phenyl-C61-butyric acid methyl ester (PCBM) polymer blend solar absorbers in a conventional device structure. The solar cell performances were found to depend on the concentration of Ag:Mg BMNPs in the photoactive medium. Consequently, significant device performance was recorded for the solar cells containing Ag:Mg BMNPs at all doping levels compared to the un-doped devices. Therefore, the highest power conversion efficiency (PCE) of 4.11% was achieved at a 1.5 wt% doping level with a high fill factor of 56% compared to the reference cell. The performance improvement in PCE constitutes a 79% improvement, which is much higher than undoped solar cells. This result was attributed to the occurrence of the localized surface plasmon resonance effect (LSPR), which is favorable for boosting the optical absorption and charge transport processes in TFOSC.

KEYWORDS
bulk-heterojunction, conventional structure, nanoparticles, organic solar cell, surface plasmonic

Chapter 4

Silver decorated magnesium doped photoactive layer for improved collection of photo-generated current in polymer solar cell

Abstract

Silver-doped magnesium (Ag:Mg) bimetallic nano-particles (BMNPs) were successfully synthesized using wet chemical processing. The collection of enhanced photo-currents is possible through metal nano-particles in the photo-active layer of a thin-film organic solar cell (TFOSC). This investigation employed poly-3-hexylthiophene(P3HT) and [6-6]-phenyl-C61-butyric acid methyl ester (PCBM) polymer blend solar absorbers in a conventional device structure. The solar cell performances were found to depend on the concentration of Ag:Mg BMNPs in the photo-active medium. Consequently, significant device performance was recorded for the solar cells containing silver magnesium (Ag.Mg) BMNPs at all doping levels compared to the un-doped devices. Therefore, the highest power conversion efficiency (PCE) of 4.11% was achieved at a 1.5 wt% doping level with a high fill factor of 56% compared to the reference device. The performance improvement in PCE constitutes a 79% improvement, which is much higher than undoped solar cells. This result was attributed to the occurrence of the localized surface plasmonic resonance (LSPR), which is favorable for boosting the optical absorption and charge transport processes in TFOSC.

Keywords:

Bulk-heterojunction, conventional structure, nanoparticles, organic solar cells, surface plasmonic resonance.

4.1 Introduction

The growing world population has created substantial pressure on the energy sector due to the demand for more energy in every aspect of life, which has led to increased consumption of fossil fuels. This has worsened environmental pollution owing to the emission of harmful by-products from the use of fossil fuels. Such dangerous climate trends have motivated scientists to seek alternative renewable and green energy sources [1]. Solar energy is one of the possible renewable energy sources that can be tapped by various solar cell technologies. From the available emerging solar cell technologies, today, thin-film organic solar cell (TFOSCs) have made tremendous progress in the realization of cheap, lightweight, and flexible solar panels [2, 3]. The success of TFOSC depends on the effectiveness of the Bulk heterojunction (BHJ) active layer design, which is composed of a donor (D) and acceptor (A) polymer molecules blend that substantially improves exciton dissociation owing to the large A/D inter-facial surfaces in the medium [4, 5].

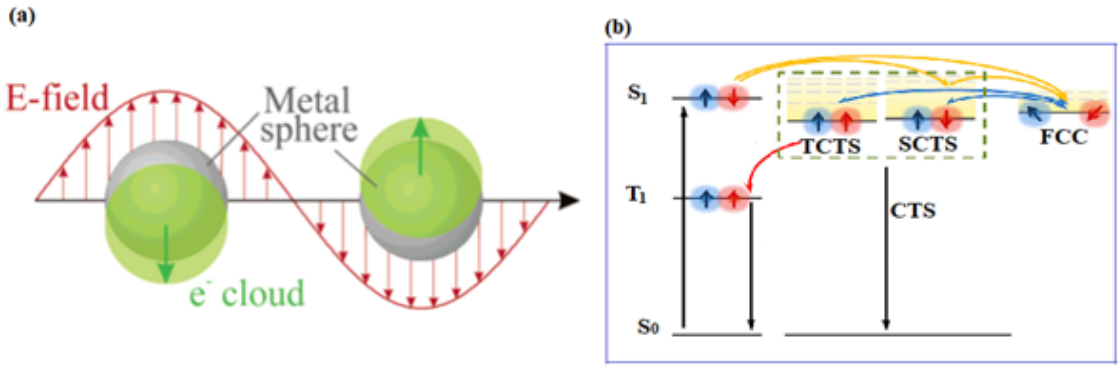

Figure 4.1: (a) Oscillations of free conduction electrons by the electric field of the incident radiation and Coulomb attraction force [6]. (b) Represents the spin-uncorrelated free electrons and holes charge carriers and charge-transfer-state recombination mechanisms for high charge density organic solar cell [7]

The power conversion efficiency (PCE) of solution-processed thin film solar cell technologies dramatically increased in recent years from less than 10% 7 years ago to nearly 20% using non-fullerene acceptor-based solar cells [8, 9]. However, the PCE values of fullerene-based solar cells are still lower than those of non-fullerene-based OSC because of the limitations of fullerene molecules in terms of narrow optical absorption band, poor energy level tunability, and poor morphology of the absorber film [10, 11].

To address some of the challenges in fullerene-based OSC, researchers employed functional metal NPs and plasmonic metal nanoparticles at different functional layers of the device structure, such as the photo-active layer or/and in the charge transport layers, which are beneficial in increasing the optical path lengths of the incident photons and harvest more photocurrent in TFOSCs [12, 13, 14, 15, 16, 17]. Moreover, the interaction of the free electrons of the metal and the incident electromagnetic waves in a dielectric medium has a substantial benefit in improving the optical absorption and charge transport processes [18, 19]. Plasmon is the result of the interaction of the incident photons and with the electron plasma of the metal NPs in a dielectric medium. The electric field component of the EM induces charge polarization on the metal NPs, which creates a dipole moment that oscillates at the frequency of the incident wave, causing resonance absorption. Absorption strongly depends on the shape and size of the metal NPs [20, 21, 22]. When the resonance frequency of the oscillating electrons is equal to or very close to the frequency of the incident light, the resulting resonance is known as the LSPR effect occurs, as provided in Figure 4.1(a). However, if the small-sized NPs have diameters less than 50 nm, at near-field enhancement effect occurs near the plasmonic nano-particles that couple to the photoactive layer, thereby increasing its effective absorption cross-section and exciton dissociation, respectively. Nevertheless, when the diameter of the NPs is much higher than 50 nm, a far-field is produced, which is probably used as an effective sub-wavelength scattering element that couples and traps freely propagating plane waves of the incident light into the solar absorber [19, 20, 21, 22, 23, 24]. According to the Haiss equation, the oscillation energy of free conduction electrons is strongly dependent on the density of the electrons N within the metal NPs according to the following relation:

$$\omega_{sp} = \sqrt{\frac{N \times e^2}{m \times \varepsilon_0}} \tag{4.1}$$

$$E_{sp} = \hbar \omega_{sp} \tag{4.2}$$

where ω_{sp} is the oscillating frequency of free conduction surface electrons, N refers to the number of electrons of the SPMNPs, m is the mass of the electron, e is the elementary charge, ϵ_0 is the free space permittivity, $\hbar$ is the Planck's constant, E_{sp} is surface plasmonic oscillating energy [25].

Materials such as gold and silver are well-known for their excellent sources of plasmonic behavior, but the high cost of these materials is the main challenge for the synthesis of NPs [26, 27]. In previous reports, Fostiropoulos et al. investigated the charge selection properties of magnesium-silver (Mg:Ag) alloy in TFOSCs and used Mg:Ag alloy as a buffer layer material and Ag as a cathode. Thus, they observed improved configuration of energy levels alignment and charge mobility with CuPc:C60 light

absorber [28]. Similarly, Oseni et al. further used Ag:Mg NPs in PTB7:PC60BM blend solar absorber in an inverted structure composed of layers of materials as (GLASS/ITO/ZnO/PTB7:PCBM:Ag:Mg NPs/MoO3 (HTL)/Al) for TFOSCs. The authors have later found an improvement in PCE that has increased by nearly 41% compared to the reference cell [29]. In this study, silver-doped magnesium bimetallic NPs (BMNPs) have been successfully synthesized and used as sub-light absorption and charge dissociation mechanisms within P3HT:PCBM solar absorber medium, in a conventional device structure such as (GLASS/ITO/PEDOT:PSS/P3HT: PCBM-Ag:Mg NPs/LiF/Al). The most popular polymer blend (P3HT:PCBM) has a high the potential of producing large area and flexible solar panel at a low cost. Therefore, the purpose of this work is to improve device performance through the use of plasmon NPs, which is expected to provide evidence on how the metal NPs influence the optoelectronic properties of the polymer films. We are reporting here a high device performance due to improved photon harvesting and charge transport processes, which resulted in an increase in PCE by 79% compared to pristine.

4.2 MATERIALS AND METHODS

4.2.1 Materials

The chemicals used in the synthesis of Ag:Mg BMNPs are silver nitrate Ag (99.5% NO2)3, Magnesium (Mg) nitrate hexahydrate Mg(NO3)2 6H2O (≥99.0%), and sodium hydroxide (99.98% NaBH4), which are purchased from a commercial source and used without further processing. Electron donor poly(3-hexylthiophene) (P3HT), an electron acceptor [6,6]-phenyl-C61-butyric acid methyl ester (PC_{61BM}) were used as a photoactive layer in the BHJ system; poly(3,4-ethylene-dioxythiophene)poly(styrenesulfonate) (PEDOT:PSS), and chloroform solvent were purchased from Sigma Aldrich.

4.2.2 Synthesis of Ag:Mg NPs

The wet chemistry method was used to synthesize Ag:Mg BMNPs, as illustrated in literature [30]. In the process, 0.25, 0.19, and 0.56 g of silver nitrate, magnesium nitrate hexahydrate, and sodium borohydride (NaBH4) were dissolved in three flasks containing 50 mL of deionized water each. The solutions were stirred for 10 min each and then mixed up in a dropwise manner while stirring the solution. The resulting mixtures were further stirred continuously for 3 h on a hot plate using a magnetic stirrer at 40°C of temperature. The resultant mixture was then filtered and washed thoroughly with deionized water several times to remove sodium ions. The resultant suspension was then dried in the oven at 70°C for 2 h and the silver-doped magnesium powder was obtained. The optical and morphological properties of the synthesized NPs dispersed in deionized water were then characterized using ultraviolet–visible

(UV–Vis) absorption spectra, high-resolution transmission tunneling and scanning electron microscopy (HRTEM and HRSEM), and energy dispersive x-ray (EDX) measurements.

4.2.3 Device fabrication

The bulk-heterojunction organic solar cells were successfully fabricated using indium tin oxide (ITO) coated glass substrates. Initially, the substrates were partially etched with a warm acid solution containing hydrochloric acid, hydrogen (II) oxide, and tri-oxonitrate-5-acid (HCL:H2O:HNO3 at a concentration of 48%:48%:4%) by volume to obtain half-coated glass substrates. After that, the substrates were subsequently cleaned up using an ultrasonic cleaner with deionized water, acetone, and isopropanol for 15 min in each solution. Then, the substrates were further dried in the oven for 20 min at 100°C. In the process, the 45 nm thickness of a hole transfer layer PEDOT:PSS was spin-coated on the substrates at 3500 rpm for 60 s followed by annealing in the oven under an ambient atmosphere at 100°C for 20 min. The photoactive layers were prepared from P3HT:$PC_{61}BM$ blends in chloroform solvent doped with 1%, 1.5%, and 3% concentrations of Ag:Mg BMNPs by weight. The solution concentration was kept at 20 mg/mL in all cases. Similarly, the reference solar absorber (P3HT:PC_{61BM}) was prepared without metal NPs. The film's solutions were heated and stirred on a hot plate at 40°C for 4 h for suitable miscibility of the molecules in the medium. The mixtures were then spin-coated on top of the dried PEDOT:PSS layer at 1200 rpm for 40 s. The samples were then annealed in the furnace under nitrogen gas for 5 min at 90°C and then transferred into a vacuum deposition chamber at a pressure of 2×10^{-6} mbar. Followed by the deposition of the electron transport layer lithium fluoride (LiF) and the Al electrode at thicknesses of 0.5 and 100 nm, respectively. The resulting device structure was GLASS SUBSTRATE/ITO/PEDOT:PSS/P3HT:$PC_{61}BM$:Ag:Mg BMNPs/LiF/Al (Figure. 4.2). Furthermore, post-device fabrication annealing was conducted for all samples for 5 min at 90°C. The optical and electrical properties of the conventional structure of TFOSCs active area (0.04) were then characterized using a Keithley HP2420 source meter and solar simulator (model SS50AAA) operating at AM1.5 and 100 mWcm^{-2} of light intensity.

4.3 RESULTS AND DISCUSSION

4.3.1 Characterizations of Ag:Mg BMNPs

The structural, morphological, and physical characteristics of Ag:Mg BMNPs were carried out using high-resolution transmission and scanning electron microscopy, respectively, as depicted in Figure. 4.3 The HRTEM image provided in Figure. 4.3(a) clearly shows different sizes of semi-spherical and core-shell-like structures for silver-doped magnesium powder. Moreover, details on the morphology of the

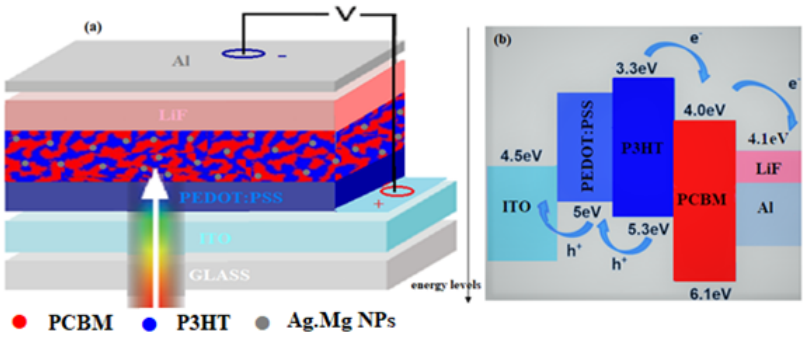

Figure 4.2: (a) The conventional structure for Ag:Mg bimetallic nanoparticles doped for the fabricated device and (b) the energy levels for different layers used in this experiment.

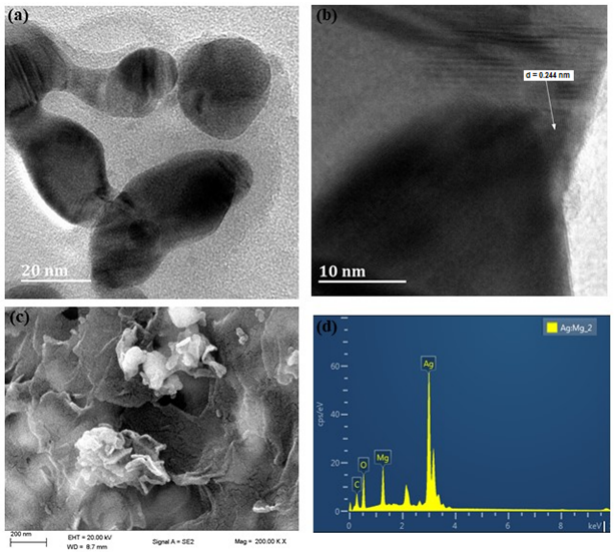

Figure 4.3: (a,b) The transmission electron microscopy images of Ag:Mg bimetallic nanoparticles at different magnifications, (c) the scanning electron microscopy image, and (d) energy dispersive x-ray.

particles as shown in Figure. 4.3(b) exhibited crystalline structure evidenced by clear fringes with a lattice spacing of about 0.244 nm. Furthermore, the HRSEM image provided in Figure. 4.3(c) clearly shows flower-like morphology of Ag:Mg NPs in the D/A medium, which also contains information about the presence of the magnesium and silver supported by the elemental analysis conducted using energy-dispersive x-ray the image is given in Figure. 4.3(d).

4.3.2 Optical properties of thin-film solar absorbers

The effect of Ag:Mg BMNPs on the optical properties of the P3HT:PCBM active layer was investigated using UV–Vis measurements. Figure. 4.4(a) is the optical absorption of Ag:Mg BMNPs powder in deionized water suspension, which constitutes a broad spectrum centered around 450 nm. The long tail

of the absorption is due to the scattering phenomenon in the water medium.

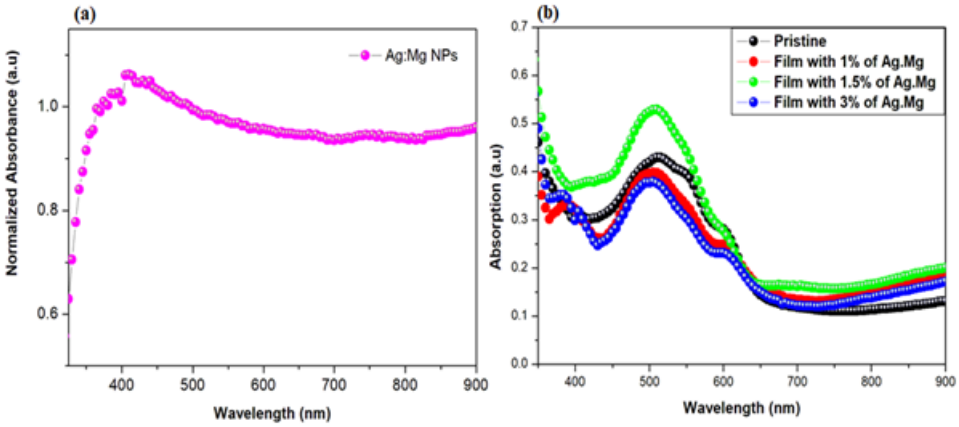

Figure 4.4: (a) Absorption spectrum of the Ag:Mg bimetallic NPs suspension in deionized water and (b) represents UV–vis absorption spectra taken from polymers blend films containing different concentrations of Ag:Mg nano-composites.

The optical absorption spectra are provided in Figure. 4.4(b) are taken from the photo-active films of newly fabricated organic solar cells. There are two prominent absorption peaks of the films in Figure. 4.4(b) centred at 430 and 510 nm are expected to result from band-to-band transitions of silver and P3HT molecules, respectively. The optical absorbance of NPs doped films from 700 to 900 nm are attributed to the long wavelength scattered waves caused by the presence of Ag:Mg NPs in the medium [31]. Furthermore, the normalized absorption spectra taken from films with/without Ag:Mg, displayed in Figure. 4.4(b), is clearly dependent on concentration as evidenced by doping levels 0%, 1%, 1.5%, and 3% by weight, respectively. Maximum peak intensity is observed at 1.5% concentrations of Ag:Mg NPs in the medium while the intensity reduces as the concentration increases. Moreover, the Ag:Mg BMNPs concentrations demonstrated maximum peaks of absorbency shifted slightly into ultraviolent regions that suggest the existence of interaction of the metal NPs with polymer molecules. The broad optical absorption, above 700 nm, in thin-film organic solar cells (TFOSCs) indicates the presence of different sizes and shapes of synthesized NPs. Such substantial light absorbance boosts the organic thin-film solar absorbers with the assistance of LSPR and SPR has a remarkable effect on exciton generations and then enhances the value of PCE in TFOSCs.

4.3.3 J–V characteristics for thin-film solar cell devices

The effect of Ag:Mg NPs is clearly evident in the performance of the solar cells, which can be analyzed from the electrical characteristics of the solar cell devices. Figure. 4.5 shows the current-voltage curves taken from the newly produced solar cells containing different concentrations of NPs in the absorber

layers. The result clearly demonstrates that there is a significant surge in photo-current by the presence of the metal NPs compared to the reference cell (Figure. 4.5). It is to be noted that the enhancement of the photo-current is dependent upon the concentration of the NPs. However, increasing concentration of the metal NPs, more than the optimum level, are found to be unfavourable for device performance as this can be noted from device parameters of the highest doping level 3%.

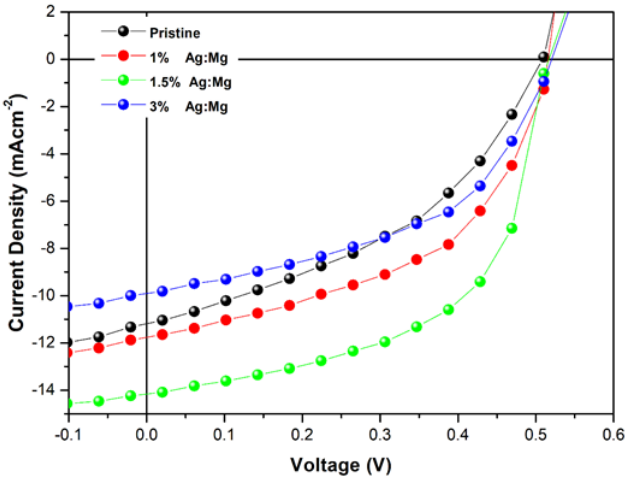

Figure 4.5: J–V characteristics of the fabricated organic solar cells at different dopant levels of Ag:Mg bimetallic NPs.

Consequently, the short circuit current (Jsc) at the 3 wt% doping level dramatically decreases when the concentration of NPs increases above 1.5 wt% (see Table 4.1). These changes could be attributed to the formation of high defect complexes that would promote high charge carrier recombination. A similar trend of device performance with concentration has been reported in the literature [32]. Furthermore, the open circuit voltage (V_{oc}) has slightly increased in NP-doped solar cells compared to the reference one, which is an indication of better energy level alignment at the interfaces.

The drop of J_{sc} at the 3% concentration of Ag:Mg BMNPs could be due to the high rate of encounters between spin uncorrelated free charge carriers within the active layer in TFOSCs. The amount of CT states that are formed directly from photo-generated excitons can play a critical role in polymer: fullerene solar cell's performance via bimolecular encounters of free charges. Furthermore, the nano-scale thickness of the low band-gap active layer polymer D and high charge densities of TFOSCs resulting from absorption, which extended to near-infrared can probably lead to a high rate of bimolecular encounters between spin-uncorrelated electrons and holes. This process can cause recombination and formation of low energy triplet excitons on the donor polymer that decays to the ground state and limits the organic photovoltaic efficiency [32, 33]. It is to be noted that the charge generation and separation mechanisms for the organic bulk-heterojunction system of the excitons can initially dissociate into charge-transfer-states (CTSs) with singlet spin and further be separated into free electrons and holes charge carriers

Table 4.1: The parameters of P3HT: $PC_{61}BM$-based solar cells fabricated at various Ag-doped-Mg nanocomposites concentrations.

Ag:Mg(%)	V_{oc}	$J_{sc}(mAm^{-2})$	FF (%)	PCE%	$R_s(\Omega cm^2)$	$R_{sh}(\Omega cm^2)$
0	0.50	11.18	40.31	2.29	915	4803
1	0.51	11.68	50.44	3.03	356	4489
1.5	0.51	14.12	56.36	4.11	364	10625
3	0.52	9.90	48.80	2.51	398	5879

(FCC) at the D/A interface followed by extraction of FCCs at their respective electrode [34, 35, 36].

Notably, the charge carrier recombination process in TFOSCs is divided into two classes such as geminate recombination (GR) and non-geminate recombination (NGR). The CT states that recombine before forming FCC is known as geminate and nongeminate recombination (NGR) occurs after the formation of FCC. Depending on the spin of the excited state where the recombination from the ground state occurs, the carrier recombination can either be radiative or non-radiative based on device performance [37, 38]. According to Han et al, NGR can probably lead to the formation of the CTS with a ratio of 25% for Singlet charge transfer(SCT) and 75% for Triplet charge transfer state(TCTS), which manifolds based on the spin-statistics. The SCT state can decay to the ground state via radiative fluorescence and nonradiative internal transformation, while the recombination of the TCTS state takes place through the low-lying triplet states (T1) on D or A, which establishes a high non-radiative energy loss [34]. As displayed in Figure. 4.1(b), TCTSs can separate again into free charges and be collected through their respective electrodes if the energy offset ($\Delta E = E_{S1} - E_{T1}$) between S1 and T1 is small enough. However, it is very challenging to regenerate free charge from SCTSs. In the low band gap polymer of fullerene solar cells, the encounters of free electrons and holes can probably lead to the formation of CT with both singlet and triplet states, as displayed in Figure. 4.1(b). The triplet charge transfer states can relax to the lower-lying triplet exciton (T1) state on the donor polymer if it is energetically possible [38, 39, 40]. The best performance recorded for the fabricated conventional solar cell was found at 1.5 wt% of doping level, which demonstrated the highest device parameters such as V_{oc} = 0.51 V, J_{sc} = 14.12 mA/cm2, FF = 56.36%, and PCE = 4.11%, respectively. Shunt resistance (R_{sh}) and series resistance (R_s) for all devices were measured under illumination with standard conditions, as provided in Table 4.1. The results further show that the performances of solar cell devices are consistent with the expected values of R_{sh} and R_s of the device, which indicates considerable charge transfer and a low recombination rate are observed at the doping level of 1.5% and 1 wt%. The fabrication of organic solar cells is environmentally friendly and uses common organic solvents unlike silicon-based solar cell

technology, which produces hazardous by-products.

4.3.4 Charge transport process in organic solar cell

Charge transport in polymer solar absorbers is an important process to understand the electrical properties of the medium. The space charge limited current (SCLC) is often considered a charge saturation condition which is useful to study the charge transport properties across the photo-active layer in thin film organic solar cells. The SCLC is measured under dark conditions, where the photo-generated charge carriers are almost suppressed and all the traps in the solar absorber medium are filled.

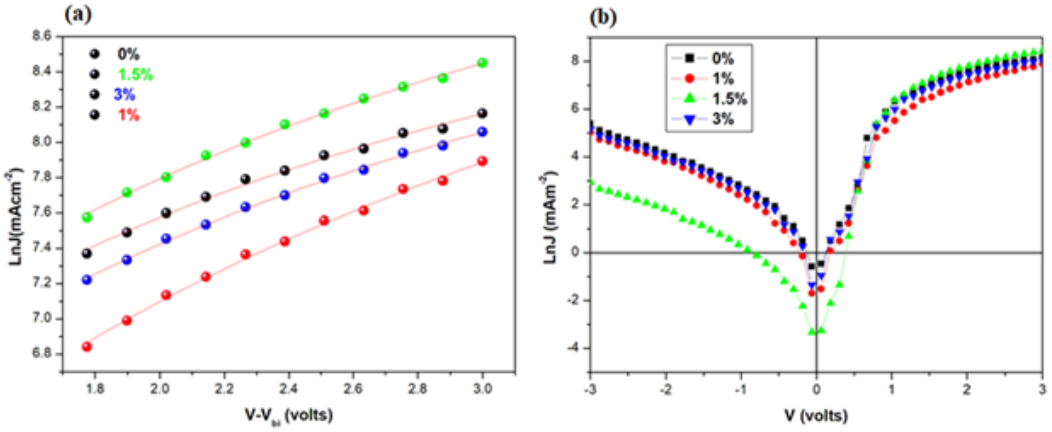

Figure 4.6: (a) The space-charge limited currents of the conventional solar cells with various concentrations of Ag:Mg bimetallic nanoparticles and (b) J–V measured under dark conditions.

As displayed in Figure. 4.6(a,b), the SCLC data were collected from the forwarded bias of the dark current, which started from the injection limited region (≥1.6 V) of the device and ended at the point where the current saturated. The data taken by SCLC was then compared with Mott-Gurny law 4.3 that uses a field-dependent mobility equation, as provided below:

$$J_{SLC} = \frac{9}{8}\varepsilon\varepsilon_0\mu_0\frac{V^2}{L^3}\exp\left(0.89\gamma\sqrt{\frac{V}{L}}\right) \tag{4.3}$$

V and L represent the applied voltage over the sample and the thickness of the solar absorber, respectively. The ϵ is the relative dielectric permittivity of the absorber medium, ϵ_0 is known as the free space permittivity, μ_0 donates the zero-field mobility, γ is the field activation factor of the device [30, 39, 40, 41]. Mathematically, the field activation factor can be expressed as $\gamma = B\left(\frac{1}{k_BT} - \frac{1}{k_BT_0}\right)$ [41]. It is dependent on temperature (T) and the constant parameters T_0 and B have mainly relied on the nature of the material. It is to be noted that the negative values found at the field activation factor suggest that the mobility diminishes at the high applied electric field in the polymer solar cells, as reported

by recent studies [41]. Furthermore, a detailed analysis of the determination of device parameters is available in literature [42, 43].

Table 4.2: The parameters of P3HT:$PC_{61}BM$-based solar cells fabricated at different concentration levels of Ag-doped-Mg nanocomposites concentrations.

Mg:Mg(%)	μ_0**(cm^2 S^{-1} V^{-1})**	γ**(cm^2 V^{-1})**
0	5.8072×10^{-4}	$\neg$ 3.4028×10^{-5}
1	1.6054×10^{-3}	$\neg$ 9.4972×10^{-5}
1.5	2.3084×10^{-3}	$\neg 1.3526\times10^{-4}$
3	1.2042×10^{-3}	$\neg$ 1.233×10^{-4}

The fits of Equation 4.3 to the experimental SCLC data are in good agreement with the theoretical prediction as provided in Figure. 4.6(a). The results further indicate that the zero-field mobility at the doping level of 1%, 1.5%, and 3% of Ag:Mg BMNPs are effectively enhanced by one order of magnitude higher than that of pristine (Table 4.2). These results are clear evidence of the effect of Ag:Mg BMNPs that enhanced the charge transport process in the polymer matrix and assisted the charge dissociation in thin-film organic solar cells.

4.4 CONCLUSION

In conclusion, core-shell type silver doped magnesium bimetallic NPs were successfully synthesized and used in P3HT:$PC_{61}BM$ bulk-heterojunction solar absorber layer at varying concentrations from 0% to 3% by weight. The effect of the NPs has been demonstrated in terms of substantial improvements in energy harvesting and charge transport properties in TFOSC. Consequently, the power conversion efficiencies of all doped solar cells outperformed the reference cells, which were in fact dependent on the concentration of the metal NPs. The highest PCE recorded in this experiment was 4.11% at 1.5 wt% doping level of Ag:Mg BMNPs. This is a 79% PCE improvement compared to the un-doped solar cell. Such improvements are attributed to the occurrence of LSPR and far-field scattering phenomena, which are favourable in light trapping, exciton dissociation, and enhancing charge transport processes in thin film organic solar cells.

References

[1] Irfan M., Zhao Z. Y., Ahmad M., Mukeshimana M. C. Solar energy development in Pakistan: Barriers and policy recommendations. *Sustainability*, 2019, **11**(4), 1206.

[2] Zhao F., Zhou J., He D., Wang C., Lin Y. Low-cost materials for organic solar cells. *Journal of Materials Chemistry C*, 2021, **9**(43), 15395-15406.

[3] Kippelen B., Brédas J. L. Organic photovoltaics. *Energy & Environmental Science*, 2009, **2**(3), 251-261.

[4] Wang H., Zhang Z., Yu J., Liu X., Tang W. High mobility acceptor as third component enabling high-performance large area and thick active layer ternary solar cells. *Chemical Engineering Journal*, 2021, **418**, 129539.

[5] Street R. A., Schoendorf M., Roy A., Lee J. H. Interface state recombination in organic solar cells. *Physical Review B—Condensed Matter and Materials Physics*, 2010, **81**(20), 205307.

[6] Kelly K. L., Coronado E., Zhao L. To Let. *The Optical Properties of Metal Nanoparticles: The Influence of Size, Shape, and Dielectric Environment*, 2003, **107**(3), 668-677.

[7] Chen Z., Chen X., Jia Z., Zhou G., Xu J., Wu Y., Xia X., Li X., Zhang X., Deng C. Triplet exciton formation for non-radiative voltage loss in high-efficiency nonfullerene organic solar cells. *Joule*, 2021, **5**(7), 1832-1844.

[8] Mola, G. T., Ahmed, A. Y. A., Ike, J. N., Liu, M., Hamed, M. S. G., Zhang, Y. Engineering non-fullerene acceptors as a mechanism to control film morphology and energy loss in organic solar cells. *Energy & Fuels*, 2022, **36**(9), 4691-4707.

[9] Notarianni M., Vernon K., Chou A., Aljada M., Liu J., Motta N. Plasmonic effect of gold nanoparticles in organic solar cells. *Solar Energy*, 2014, **106**, 23-37.

[10] Hou J., Inganas O., Friend R. H., Gao F. Organic solar cells based on non-fullerene acceptors. *Nature Materials*, 2018, **17**(2), 119-128.

[11] Camaioni N., Po R. Pushing the envelope of the intrinsic limitation of organic solar cells. *The Journal of Physical Chemistry Letters*, 2013, **4**(11), 1821-1828.

[12] Hamed M. S. G., Mola G. T. Highly stable thin film organic solar cells using poly crystallized silver doped LaPO4. *Solar Energy*, 2020, **207**, 157-164.

[13] Linic S., Christopher P., Ingram D. B. Plasmonic-metal nanostructures for efficient conversion of solar to chemical energy. *Nature Materials*, 2011, **10**(12), 911-921.

[14] Dlamini M. W., Mola G. T. Near-field enhanced performance of organic photovoltaic cells. *Physica B: Condensed Matter*, 2019, **552**, 78-83. Elsevier.

[15] Oseni S. O., Mola G. T. Bimetallic nanocomposites and the performance of inverted organic solar cell. *Composites Part B: Engineering*, 2019, **172**, 660-665. Elsevier.

[16] Lindquist N. C., Luhman W. A., Oh S. H., Holmes R. J. Plasmonic nanocavity arrays for enhanced efficiency in organic photovoltaic cells. *Applied Physics Letters*, 2008, **93**(12).

[17] Gu M., Ouyang Z., Jia B., Stokes N., Chen X., Fahim N., Li X., Ventura M. J., Shi Z. Nanoplasmonics: a frontier of photovoltaic solar cells. *Nanophotonics*, 2012, **1**(3-4), 235-248.

[18] Sakai J., Taima T., Yamanari T., Yoshida Y., Fujii A., Ozaki M. Pentacene: fullerene multilayer-heterojunction organic photovoltaic cells fabricated by alternating evaporation method. *Japanese Journal of Applied Physics*, 2010, **49**(3R), 032301.

[19] Stratakis E., Kymakis E. Nanoparticle-based plasmonic organic photovoltaic devices. *Materials Today*, 2013, **16**(4), 133-146. Elsevier.

[20] Atwater H. A., Polman A. Plasmonics for improved photovoltaic devices. *Nature Materials*, 2010, **9**(3), 205-213.

[21] Bohren C. F., Huffman D. R. Absorption and scattering of light by small particles. John Wiley & Sons, 2008.

[22] Sha W. E. I., Choy W. C. H., Liu Y. G., Chew W. C. Near-field multiple scattering effects of plasmonic nanospheres embedded into thin-film organic solar cells. *Applied Physics Letters*, 2011, **99**(11).

[23] Pillai S., Catchpole K. R., Trupke T., Green M. A. Surface plasmon enhanced silicon solar cells. *Journal of Applied Physics*, 2007, **101**(9).

[24] Wei E. I., Choy W. C. H., Chew W. C. Angular response of thin-film organic solar cells

with periodic metal back nanostrips. *Optics Letters*, 2011, **36**(4), 478-480.

[25] Haiss W., Thanh N. T. K., Aveyard J., Fernig D. G. Determination of size and concentration of gold nanoparticles from UV-Vis spectra. *Analytical Chemistry*, 2007, **79**(11), 4215-4221.

[26] Lee Y. H., Kim D. H., Kim T. W. Enhancement of the power conversion efficiency of organic photovoltaic cells due to Au@SiO2 core shell nanoparticles embedded into a WO3 hole transport layer. *Organic Electronics*, 2019, **68**, 182-186.

[27] Oo T. Z., Mathews N., Xing G., Wu B., Xing B., Wong L. H., Sum T. C., Mhaisalkar S. G. Ultrafine gold nanowire networks as plasmonic antennae in organic photovoltaics. *The Journal of Physical Chemistry C*, 2012, **116**(10), 6453-6458.

[28] Fostiropoulos K., Rusu M. Engineering of hybrid interfaces in organic photovoltaic devices. *Solar Energy Materials and Solar Cells*, 2011, **95**(6), 1489-1494.

[29] Mola G. T., Arbab E. A. A., Taleatu B. A., Kaviyarasu K., Ahmad I., Maaza M. Growth and characterization of V2O5 thin film on conductive electrode. *Journal of Microscopy*, 2017, **265**(2), 214-221.

[30] Ike J. N., Dlamini M. W., Dwivedi R. P., Zhang Y., Mola G. T. Plasmon assisted optical absorption and reduced charge recombination for improved device performance in polymer solar cell. *Journal of Physics and Chemistry of Solids*, 2022, **165**, 110662.

[31] Hamed M. S. G., Ike J. N., Mola G. T. Plasmonic nano-particles mediated energy harvesting in thin-film organic solar cells. *Journal of Physics D: Applied Physics*, 2021, **55**(1), 015102.

[32] Chow P. C. Y., Gélinas S., Rao A., Friend R. H. Quantitative bimolecular recombination in organic photovoltaics through triplet exciton formation. *Journal of the American Chemical Society*, 2014, **136**(9), 3424-3429.

[33] Di Nuzzo D., Aguirre A., Shahid M., Gevaerts V. S., Meskers S. C. J., Janssen R. A. J. Improved film morphology reduces charge carrier recombination into the triplet excited state in a small bandgap polymer-fullerene photovoltaic cell. *Advanced Materials*, 2010, **22**(38), 4321-4324.

[34] Han G., Hu T., Yi Y. Reducing the singlet-triplet energy gap by end-group π-π stacking toward high-efficiency organic photovoltaics. *Advanced Materials*, 2020, **32**(22), 2000975.

[35] Norton J. E., Cornil J., Coropceanu V. Molecular Understanding of Organic Solar Cells: The Challenges. *Accounts of Chemical Research*, 2009, **42**(11), 1691-1699.

[36] Han G., Yi Y., Shuai Z. From molecular packing structures to electronic processes: theo-

retical simulations for organic solar cells. *Advanced Energy Materials*, 2018, **8**(28), 1702743.

[37] Liu Y., Li Y., Wu Y., Yang G., Mazzarella L., Procel-Moya P., Tamboli A. C., Weber K., Boccard M., Isabella O., et al. High-efficiency silicon heterojunction solar cells: materials, devices and applications. *Materials Science and Engineering: R: Reports*, **142**, pp. 100579, 2020. Elsevier.

[38] Mühlbacher D., Scharber M., Morana M., Brabec C., Zhu Z., Waller D., Gaudiana R. High photovoltaic performance of a low-bandgap polymer. *Advanced Materials (Weinheim)*, 2006, **18**.

[39] Dyer-Smith C., Reynolds L. X., Bruno A., Bradley D. D. C., Haque S. A., Nelson J. Triplet formation in fullerene multi-adduct blends for organic solar cells and its influence on device performance. *Advanced Functional Materials*, 2010, **20**(16), 2701-2708.

[40] Coropceanu V., Cornil J., da Silva Filho D. A., Olivier Y., Silbey R., Brédas J. L. Charge transport in organic semiconductors. *Chemical Reviews*, 2007, **107**(4), 926-952.

[41] Mola G. T., Abera N. Correlation between LUMO offset of donor/acceptor molecules to an open circuit voltage in bulk heterojunction solar cell. *Physica B: Condensed Matter*, 2014, **445**, 56-59.

[42] Sharma N., Gupta S. K., Negi C. M. S. Influence of active layer thickness on photovoltaic performance of PTB7: PC70BM bulk heterojunction solar cell. *Superlattices and Microstructures*, 2019, **135**, 106278.

[43] Yadav A., Upadhyaya A., Gupta S. K., Negi C. M. S. Thermal annealing dependence of charge injection and transport in the P3HT: graphene nanocomposite based devices. *Physica E: Low-dimensional Systems and Nanostructures*, 2020, **124**, 114351.

Chapter 5

Nickel-doped silver nanoclusters as a mechanism to capture photons

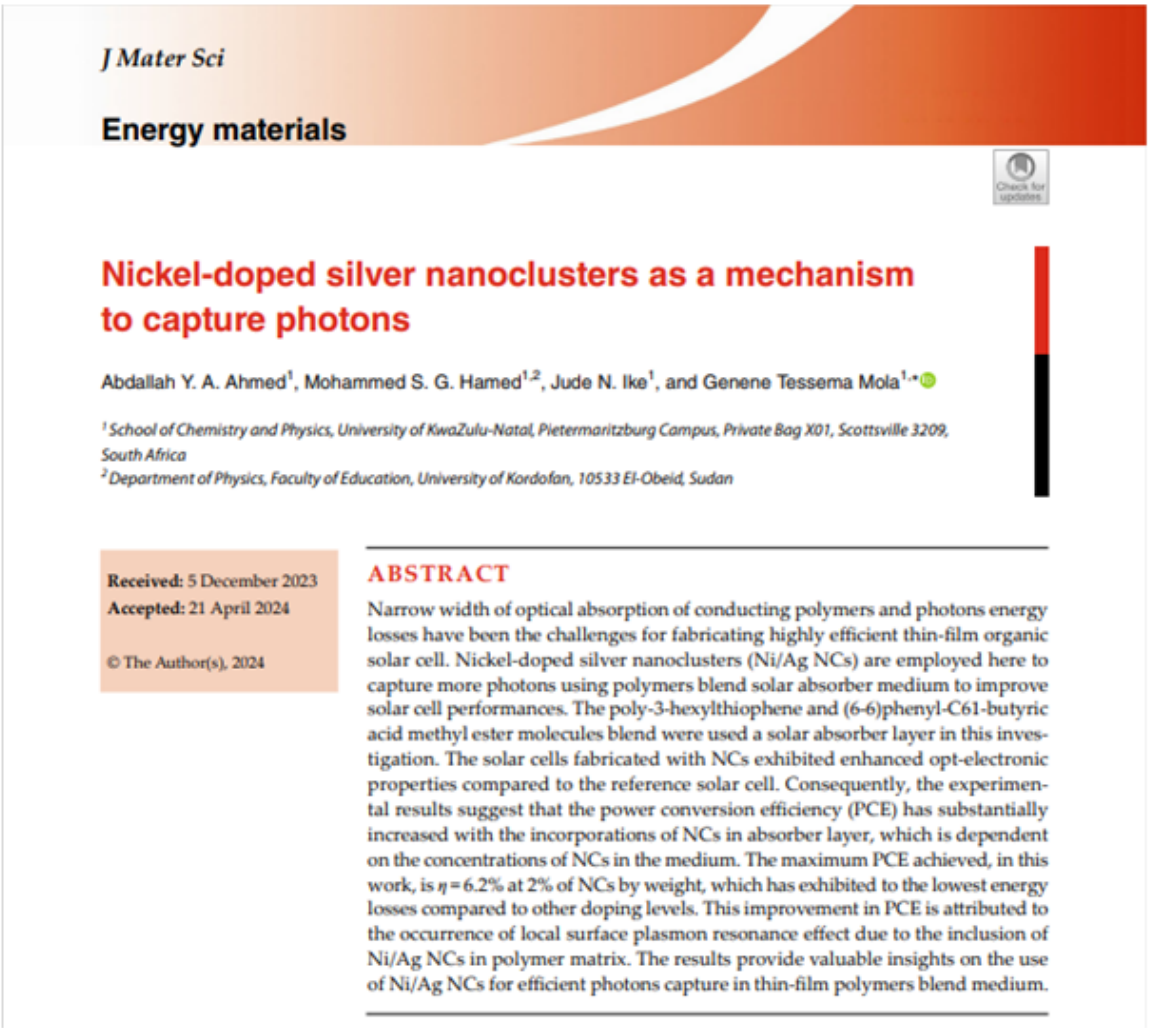

J Mater Sci

Energy materials

Nickel-doped silver nanoclusters as a mechanism to capture photons

Abdallah Y. A. Ahmed[1], Mohammed S. G. Hamed[1,2], Jude N. Ike[1], and Genene Tessema Mola[1,*]

[1] *School of Chemistry and Physics, University of KwaZulu-Natal, Pietermaritzburg Campus, Private Bag X01, Scottsville 3209, South Africa*

[2] *Department of Physics, Faculty of Education, University of Kordofan, 10533 El-Obeid, Sudan*

Received: 5 December 2023
Accepted: 21 April 2024

ABSTRACT

Narrow width of optical absorption of conducting polymers and photons energy losses have been the challenges for fabricating highly efficient thin-film organic solar cell. Nickel-doped silver nanoclusters (Ni/Ag NCs) are employed here to capture more photons using polymers blend solar absorber medium to improve solar cell performances. The poly-3-hexylthiophene and (6-6)phenyl-C61-butyric acid methyl ester molecules blend were used a solar absorber layer in this investigation. The solar cells fabricated with NCs exhibited enhanced opt-electronic properties compared to the reference solar cell. Consequently, the experimental results suggest that the power conversion efficiency (PCE) has substantially increased with the incorporations of NCs in absorber layer, which is dependent on the concentrations of NCs in the medium. The maximum PCE achieved, in this work, is $\eta = 6.2\%$ at 2% of NCs by weight, which has exhibited to the lowest energy losses compared to other doping levels. This improvement in PCE is attributed to the occurrence of local surface plasmon resonance effect due to the inclusion of Ni/Ag NCs in polymer matrix. The results provide valuable insights on the use of Ni/Ag NCs for efficient photons capture in thin-film polymers blend medium.

Chapter 5

Nickel-doped silver nanoclusters as a mechanism to capture photons

Abstract

Narrow width of optical absorption of conducting polymers and photons energy losses have been the challenges for fabricating highly efficient thin-flm organic solar cell. Nickel-doped silver nanoclusters (Ni/Ag NCs) are employed here to capture more photons polymers blend solar absorber medium to improve solar cell performances. The poly-3-hexylthiophene and (6-6)phenyl-C61-butyric acid methyl ester molecules blend were used as solar absorber layer. The solar cells fabricated with NCs exhibited enhanced opt-electronic properties compared to the reference solar cell. Consequently, the experimental results suggest that the power conversion efficiency (PCE) has substantially increased with the incorporations of NCs in absorber layer, which is dependent on the concentrations of NCs in the medium. The maximum PCE achieved, in this work, is $\eta = 6.2\%$ at 2% of NCs by weight, which has exhibited to the lowest energy losses compared to other doping levels. This improvement in PCE is attributed to the occurrence of local surface plasmon resonance effect due to the inclusion of Ni/Ag NCs in polymer matrix. The results provide valuable insights on the use of Ni/Ag NCs for efficient photons capture in thin-flm polymers blend medium.

5.1 Introduction

Solution-processed thin-film organic solar cells (TFOSCs) have garnered significant attention due to their mechanical flexibility, lightweight, and inexpensive fabrication methods [1, 2, 3, 4]. However, there are still challenges to be addressed in the area of improving optical absorption bandwidth, charge

transport processes, and the lifetime of TFOSC without compromising the low-cost device fabrication. In this study, several approaches have been proposed to optimize photon energy harvesting, inter-facial engineering, and controlling film morphology in TFOSCs through the incorporation of various materials, such as metal NPs, graphene, carbon nano-tubes, and solvent additives [5, 6]. One key component, in achieving high-power conversion efficiency, in TFOSCs structure is the nature of solar absorber for effective photon capture and the generation of free charge carriers [7, 8, 9]. Increasing the thickness of the thin-film solar absorber layer is one of the direct mechanisms to enhance optical absorption and harvest more photons. However, this approach promotes high charge recombination since the short exciton diffusion length generated in the donor polymer constrains the effective photo-active layer thickness to few hundred for the bulk heterojunction [10, 11, 12, 13]. Consequently, solar cells with relatively high active layer thicknesses suffer from significant loss of photogenerated current through radiative and non-radiative charge recombinations before reaching the donor/acceptor interface. Therefore, to address this challenge, researchers have explored the use of metal NPs at different functional layers of TFOSCs. Metal NPs enhance light absorption via light scattering processes that increase optical path length leading to trapping in the photoactive medium. This resulted in improved performance indicators across all solar cell parameters [11, 14]. There are several research reports on the positive impact of metal NPs such as silver, copper, and gold incorporated into the photoactive layer of a solar cell, which is characterized by the enhanced electrical conductivity of the thin-film organic semiconductor medium [15, 16, 17, 18, 19, 20]. Additionally, the occurrence of surface plasmonic resonance (SPR) of the metal NPs can significantly improve the optical absorption of the semiconductor medium [21] by promoting light scattering and electron band-to-band transition. A thorough understanding of the physics behind the local surface plasmonic resonance (LSPR) phenomenon is crucial for the development and implementation of plasmonic NPs for various applications. To achieve the desired adaptation between film absorption and SPR property of the metal NPs, certain physical features such as size, morphology, location, and composition of noble metal NPs must be precisely designed, taking into account the permittivity of the surrounding medium [22]. An excellent device performance is reported from use of poly-(3-hexylthiophene) (P3HT) and non-fullerene acceptor [23], which is an important development on the application of stable donor polymer P3HT. On the other hand, metal nanoparticles such as gold (Au) are reported to make a notable influence on the optical absorption and subsequent improvement in power conversion efficiencies (PCE) of solar cells, upon the integration of plasmonic gold (Au) nanoparticles into OPV structures, consisting of P3HT and [6,6]-phenyl C61 butyric acid methyl ester (PCBM) [24, 25, 26, 27]. However, the utilization of materials such as gold for large-scale device production remains a challenge due to their limited supply and high cost. In this study, Ni/Ag NCs have been used for the first time in the P3HT and PC61BM blend solar absorber is known as P3HT:PCBM

matrix or any other conjugated polymer blend to the knowledge of the authors. The inclusion of the NCs in a polymer blend has positively impacted the optical absorption and the device performance much better than reported in the literature for the same polymer blends. Therefore, the results of the investigation indicated that significant improvement in PCE is recorded due to the presence of Ni/Ag NCs in device functional layers. Details of the results are discussed in the following sections.

5.1.1 Fundamentals of surface plasmonic

The origin of SPR is the coherent oscillation of free electrons on the surface of metal NPs by the actions of the incident electromagnetic field. This oscillation arises from the induced dipole moments as the result of surface electron displacement relative to the nuclei due to the changing electric field of the incident electromagnetic wave (see Figure. 5.1(a)). The restoring force of the induced moment causes the electron cloud to oscillate against the oppositely charged nuclei at a specific frequency [28, 29]. A resonance occurs when the frequency of oscillation coincides with the incident photons. On the other hand, such interactions between electron plasma and incident radiation could cause the excitation of metals through electron band-to-band transition (see Figure. 5.1(b)) and contribute to optical absorption. The intense electromagnetic field formed near the metal NPs, as the result of the interaction, would cause the emission of light at a frequency similar to the incident photons and is scattered in all directions [30]. Therefore, the collective oscillation of electrons on the surface of NPs produces a high extinction cross-section of metal NPs in the form of scattering and absorption. Furthermore, the oscillating electrons lose some of their energy in the form of heat due to their continuous mechanical oscillations. Nonetheless, the active area of the metal nanoparticle that scatters light is defined by the scattering cross-section σ_{sc} [31] while the absorption cross-section is denoted by σ_{abs}. Hence, the total extinction cross-section coefficient of the metal NPs in the surrounding medium can be expressed by the Espinosa E_q. [32].

$$\sigma_{axt} = \sigma_{abs} + \sigma_{sc} \tag{5.1}$$

The absorption and scattering cross-sections are derived from the classical electromagnetic theory using spherical metal NPs with diameters below the light penetration depth.

By employing quasi-static approximation method, the absorption cross-section (σ_{abs}) and scattering cross-section (σ_{sc}) are given by:

$$\sigma_{abs} = 4m\pi ka^3 lm\left[\frac{\varepsilon(\omega)-\varepsilon_d}{\varepsilon(\omega)+2\varepsilon_d}\right] \tag{5.2}$$

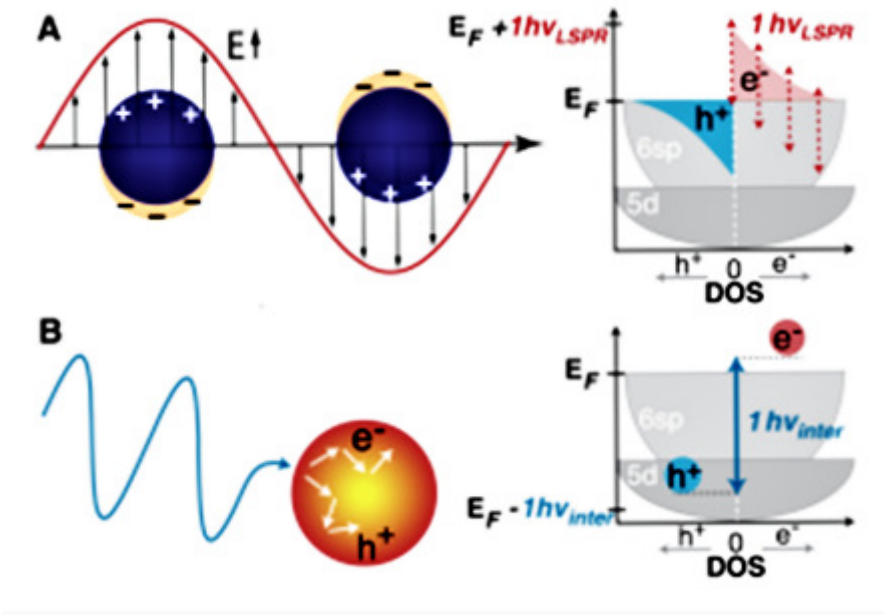

Figure 5.1: A schematic diagram illustrating the process of electron-hole pair generation and inter-band transition at the local surface plasmon resonance in pure metal and hybrid metal nanocomposites. The diagram shows how the incident light induces oscillations of electron clouds (left), leading to a decline in LSPR and the generation of a population of hot carriers with various energies (right). b How inter-band transitions are a result of higher energy photons (left) and directly produce electron-hole pairs (right) [33].

$$\sigma_{sca} = 8\frac{\pi}{3}k^4a^6\left[\frac{\varepsilon(\omega)-\varepsilon_d}{\varepsilon(\omega)+2\varepsilon_d}\right]^2 \tag{5.3}$$

where wave vector k is defned as k = $2\pi/\lambda$, λ is the wavelength of the incident wave. In this context, $\varepsilon(\omega)$ represents the dielectric constant or permittivity of the metal NPs, while a refers to the radius of the NPs. The dielectric constant ε_d stands for the medium that surrounds the NPs, as cited in reference [34]. In the realm of physics, the permittivity $\varepsilon(\omega)$ can be expressed as a composite of two distinct components, namely the real and imaginary parts. The real part, often referred to as the resonance peak, serves as a marker of the position of the permittivity. On the other hand, the imaginary part conveys information about the de-phasing. It is important to note that these two components work in tandem to fully characterize the permittivity.

$$\varepsilon(\omega) = \varepsilon_r(\omega)+i\varepsilon_i(\omega) \tag{5.4}$$

The permittivity of metal NPs in Eq. (6.4) is further rearranged and simplified into:

$$\varepsilon(\omega) = 1 - \frac{\omega_p^2}{\omega(\omega+\gamma_b)} \tag{5.5}$$

where ε_p and γ_b are the plasmonic frequency and the damping constant of metal NPs, respectively. These parameters are defined by the following equations:

$$\varepsilon_p^2 = \frac{Ne^2}{\varepsilon_0 m} \tag{5.6}$$

$$\gamma_b = \frac{\nu F}{l_m} \tag{5.7}$$

Thus, n is the density of electrons, e is the electron charge, m is the mass of the electron, and ε_0 is the permittivity of the free space. Therefore, the symbol γ_b refers to the damping constant, which is represented by the fermi velocity and mean free path of the electrons l_m [35].

5.2 Materials and methods

5.2.1 Materials

The chemicals used in the synthesis of Ni/Ag NCs were obtained from commercial sources and used as delivered. These are silver nitrate ($AgNO_3$), nickel nitrate ($Ni(NO_3)_2$) ($\geq$99.0%), and sodium hydroxide (99.98% NaBH4) are purchased from Merck. The photo-active layer in the BHJ absorber consisted of polymers such as poly(3-hexylthiophene) (P3HT) as the electron donor and (6-6)phenyl-C61-butyric acid methyl ester ($PC_{61}BM$) as the electron acceptor which was obtained from Ossila Ltd. (UK). The PEDOT:PSS and chloroform solvent were procured from Sigma-Aldrich.

5.2.2 Synthesis and characterizations of Nickel-doped silver NCs (Ni/Ag)

In this study, nickel-doped silver (Ni/Ag) was synthesized using a chemical reduction method that has been previously reported in the literature [36]. Initially, solutions of nickel nitrate (0.44 g), silver nitrate (0.13 g), and sodium borohydride (NaBH4) (0.57 g) were prepared by dissolving each compound in 50 mL of deionized water in separate flasks. The solutions were stirred for 10 min before the silver nitrate solution was added dropwise to the nickel nitrate solution under magnetic stirring. The resulting mixture was further stirred on a hot plate with a magnetic stirrer for 20 min, followed by the addition of NaBH4 solution. The mixture was then stirred continuously for 3 h at 40° C. The resulting solution was purified several times using deionized water to eliminate the sodium nitrate agent, and the precipitate was then dehydrated for 2 h at 70° C under vacuum. This resulted in the synthesis of nickel-doped silver powder.

To study morphology and photosensitive properties of the synthesized Ni/Ag NCs, we used ultraviolet-visible (UV–Vis) absorption spectra, high-resolution transmission and scanning electron microscopy (HRTEM and HRSEM), energy dispersive X-ray (EDX), and X-ray diffraction (XRD) measurements.

5.2.3 Device preparations

Thin-film organic solar cells were fabricated on transparent indium tin oxide (ITO)-coated glass substrates. The absorber layers are composed of polymers blend of P3HT:$PC_{61}BM$ with/without Ni/Ag NCs. Initially, the substrates were partially etched with a warm acid solution consisting of hydrochloric acid, water, and nitric acid (HCL:H2O:HNO_3) at a concentration of 48%:48%:4%) by volume. The substrates were then cleaned in an ultrasonic bath with deionized water, acetone, and isopropanol for 15 min, followed by drying in an oven at 100° C for 20 min. Next, a thin hole transport layer PEDOT:PSS was spin-coated onto the substrates, followed by annealing in an oven under an ambient atmosphere at 100° C for 20 min. The solar absorber medium comprising of P3HT and $PC_{61}BM$ polymers was prepared by dissolving them in chloroform solvent at a concentration of 20 mg/ml and using a 1:1 stoichiometric ratio by weight. The metal NCs are dispersed in the solution at the concentrations 1%, 2%, 3%, and 5% by weight relative to the weight of the polymer blend. The solutions were stirred on a hot plate at 40° C for 4 h to ensure proper miscibility of the polymers. The resulting blends were spin-coated on top of the dried PEDOT:PSS layer at 1200 rpm for 40 s, followed by dehydration under a nitrogen atmosphere for 10 min at 90° C. The samples were then transferred onto the vacuum deposition chamber for the thermal evaporation process for the electron transfer layer, lithium fluoride LiF and the aluminum (Al) electrode. Thin layers of LiF (0.5 nm) and Al (100 nm) were deposited on top of the samples. The resulting devices had the following structure: ITO/PEDOT: PSS/P3HT:$PC_{61}BM$:Ni/Ag NCs/LiF/Al. The devices were further annealed for 5 min. The performance of the devices was determined by measuring the electrical properties using a Keithley HP2420 source meter integrated with a solar simulator (model SS50AAA). The simulator is operating at AM1.5 and 100 mWcm^{-2} of light intensity. A schematic diagram for the conventional device structure with the combination of Ni/Ag NCs are displayed in see Figure. 5.2.

5.3 Results and discussion

5.3.1 Characterizations of Ni/Ag NCs

The optical properties of Ni/Ag NCs

The optical properties of the Ni/Ag NCs were examined through the use of a UV–Vis spectrometer in the range (300 - 900 nm). The measured UV–Vis spectra of the newly synthesized metal NPs taken

in a deionized water suspension are given in Figure. 5.3(a and b). As illustrated in Figure. 5.3(a), the absorbance of nickel-doped NC exhibited absorption in the range of 350–900 nm, with a peak located at 460 nm, and a tail extending into the near-infrared region of the electromagnetic spectrum. This significant broadening of the absorption spectra of the synthesized nano-composites indicates the presence of multiple sizes and shapes of metal nanoparticles, which is expected to enhance the optical extinction coefficients of the solar absorber through photon absorption in small volumes (LSPR modes) and light scattering in larger sizes to the surrounding medium [37]. Tauck's model is also employed to determine the energy band gap for NPs, Figure. 5.3(b). Tauc's model relies on the absorption coefficient of the materials α, which is related to the optical energy band gap, E_g. The relationship between α and E_g is described by equation shown below:

$$\alpha\beta = \gamma_f(h\nu - E_g)^n \tag{5.8}$$

Here β is the photon's energy and is defined by $\beta = hc/\lambda$, where h stands for Planck's constant, c is the speed of light, and λ is the wavelength of the photon. The constant parameter γ characterizes the optical frequency range, and the index n is used to describe the nature of the electronic transitions, taking on a value of 1/2 for direct transitions or 2 for indirect transitions. The absorption coefficient α is a crucial parameter in this model. By analyzing the plot ($\alpha h\nu$) vs ($h\nu$) and extrapolating a line tangent to the curve $(\alpha h\nu)^2 = 0$, it was possible to determine the optical energy gap to be 1.67 eV. This value of the optical band gap is anticipated to have a notable impact on the energy harvesting capabilities of the photoactive layer of solar cells, particularly for longer wavelength electromagnetic photons [38, 39].

Morphology of the Ag/Ni NCs

The morphology of the Ni/Ag NCs in powder form was investigated using high-resolution transmission and scanning electron microscopies (HRTEM and HRSEM), respectively. These spectrometers provide information such as shape, size, crystallinity, and elemental mapping of nanocomposite. The HRTEM images taken from nickel-doped silver NCs powders are presented in Figure. 5.4, where Figure. 5.4(a and c) illustrates the formations of various sizes and shapes of NCs. It has been noted that there is a nano-sphere-like structure as evidenced in Figure. 5.5(a), which exhibited various sizes in the medium. The size variations have a significant influence on the energy harvesting process through the occurrence of SPR and LSPR effects. The HRSEM elemental mapping is provided in Figure. 5.4(d) demonstrates an even distribution of nickel and silver elements within the medium, indicating the good participation of the elements in the formation of Ni/Ag NCs. Furthermore, the energy-dispersive X-ray (EDX) image in Figure. 5.4(d) reveals the nickel and silver concentrations in the metal NCs corresponding to 64.98%

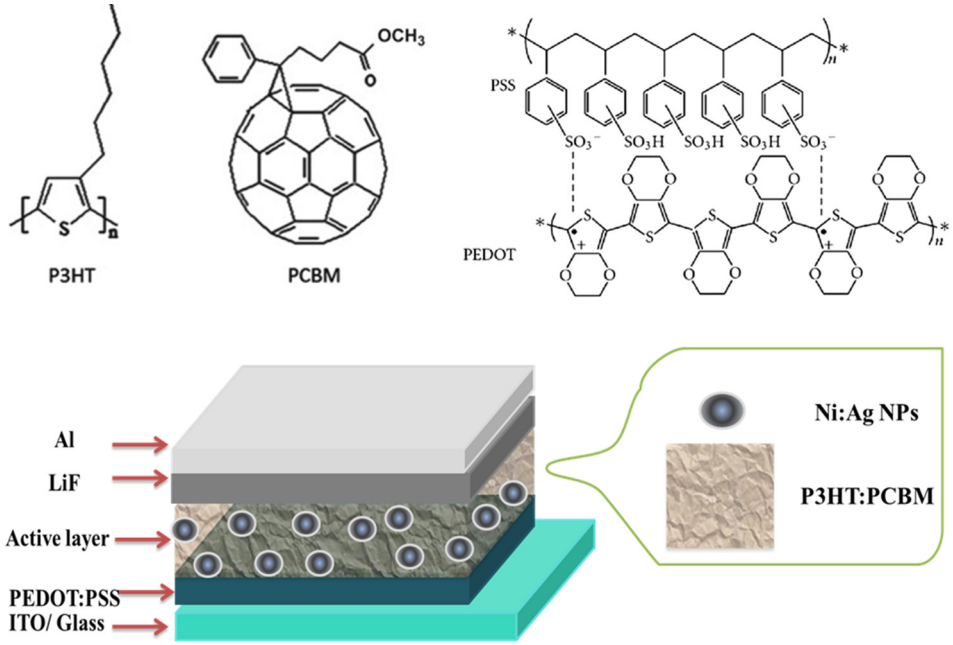

Figure 5.2: Fabricated solar cells device structure and the polymer materials used in this experiment.

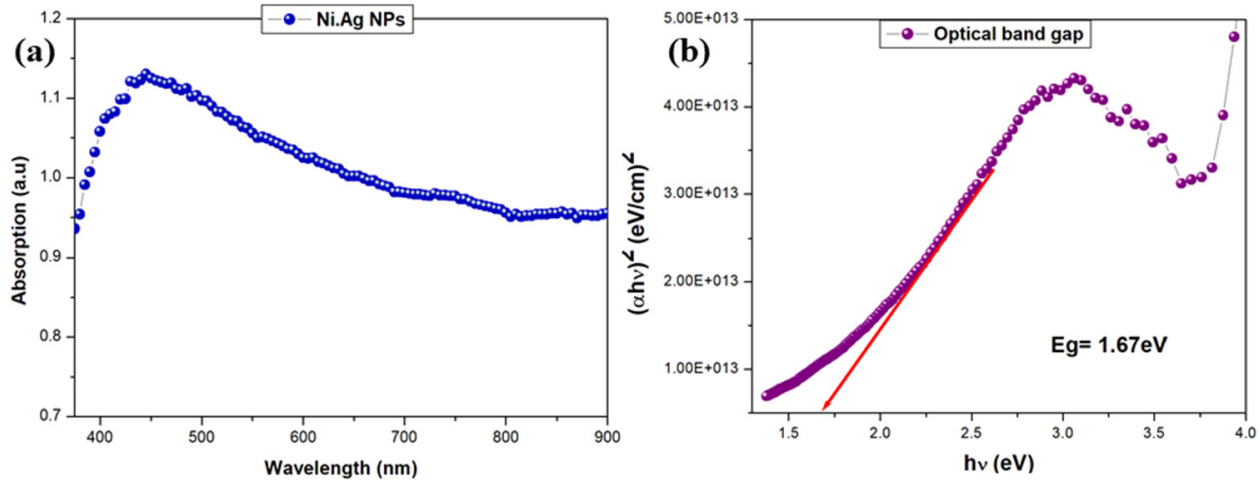

Figure 5.3: a The optical absorption for Ni/Ag NCs powder dispersed in deionized water and b the optical energy band gap for Ni/Ag NCs.

and 35.02%, respectively, at a 2:1 ratio. This finding confirms the purity of the synthesized metal NCs and their formation at the required ratio throughout the medium, which is beneficial for influencing molecular crystallinity and energy harvesting in solar cell devices. The crystalline fringes observed in HRTEM imaging are depicted in Figure. 5.4(b), which revealed an atomic lattice spacing of 0.226 nm, consistent with a cubic crystal structure of the metal NCs found using XRD measurements. According to XRD data, the d-spacing of the Ni/Ag NCs was calculated using the Bragg equation and found to be d = 0.229 nm, which is in good agreement with the values derived from HRTEM images of 0.226 nm, which corresponds to the (111) atomic plane of the Ni/Ag NCs [40].

XRD study of Ni/Ag

To examine the crystallographic structure and morphological characteristics of Ni/Ag NCs, X-ray diffraction (XRD) analysis was carried out. The measured XRD spectrum, depicted in Figure. 5.5, was obtained by scanning the sample from angles 20° to 90° at 2 theta degrees. The diffraction peaks observed at 2Θ angles indicated the presence of five prominent peaks at values of 38.29°, 44.42°, 64.56°, 77.56°, and 81.60°. These diffraction peaks corresponded to the reflections of the X-ray beam from planes (111), (200), (220), (311), and (222), respectively. Our findings indicated that Ni/Ag NCs exhibited a cubic crystal structure with cell parameters a = b = c = 4.0772 A^0 with alpha = beta = gamma = 90° [41].

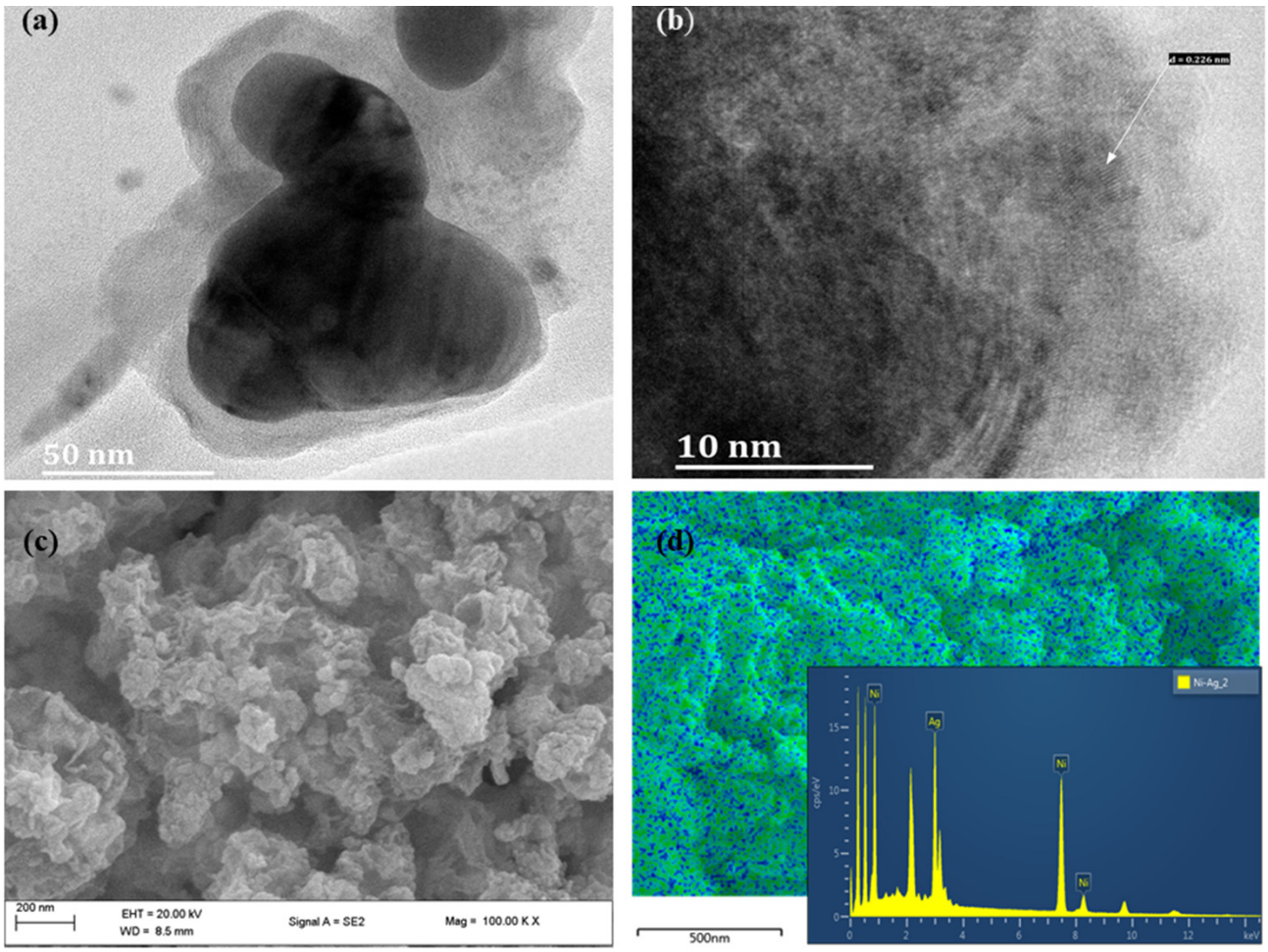

Figure 5.4: a High-resolution transmission electron microscopy image of Ni/Ag powder representing different shapes and sizes of the NCs, b the crystallite fringes have been taken from Ni/Ag powder indicating lattice spacing and crystallite of Ni/Ag NCs, scanning electron microscopy (SEM)image showing the morphology of Ni/Ag NCs in powder form, and d SEM image background and the energy-dispersive X-ray analysis taken from Ni/Ag powder indicating the elemental composition.

Using Debye–Scherer's following expression, the crystalline size D of the Ni/Ag NCs was calculated.

$$D = \frac{k\lambda}{\beta \cos\theta} \tag{5.9}$$

The Scherer constant (K) was determined to be 0.89, and the wavelength of the X-ray λ was 1.54 Angstroms. β and θ, the full width at half maximum (FWHM) of the diffraction peak measured in radians and their corresponding maximum peak angles determined by using Bragg's equation in degree, were also taken into consideration. The calculated average size for the powder crystals was 50.8 nm, indicating the significant light scattering effect of plasmonic Ni/Ag that influenced the energy harvesting of the photo-active layer. Table 5.1 summarizes the results obtained from the X-ray diffraction analysis of Ni/Ag NCs. In addition, the crystallographic structure of Ni/Ag NCs were evaluated by dislocation density (δ), micro-strain (ε) and stress (σ) were calculated by employing Hooke's law on the measured XRD data, can be determined by the following equations:

$$\delta = \frac{1}{D^2}, \varepsilon = \frac{\beta \cos\theta}{4} \tag{5.10}$$

$$\sigma = C\varepsilon \tag{5.11}$$

However, the micro-strain (ε) and stress (σ) of Ni/Ag NCs are linearly increasing with decreased crystal sizes (see Table 5.1). Furthermore, the crystallite sizes of Ni/Ag NCs are found to be between 26 nm and 70 nm, which are designed in smaller structures. This is suitable for photoactive layer polymer blend for improved charge transport processes. The stress can be determined from the ascribed micro-strain, and the value of C = 1.46 $\pm$ $10^1$0 Nm^{-2}taken from the bulk Young's modulus [42, 43].

5.3.2 Device characterizations

Optical properties of thin-film solar absorbers

Optical spectroscopy is a useful tool to investigate the mechanisms of photoabsorption in plasmonic embedded polymer thin films. The UV-Vis measurements were conducted on pristine - and Ni/Ag NPs incorporated - P3HT/PCBM layers in the range 300 - 900 nm. The measured UV–Vis spectra taken from the absorbers films with/without Ni/Ag NCs are presented in Figure. 5.6(a). The spectra are dominated by the absorption of PT3HT:PCBM blend centered around a 515-nm peak accompanied by vibronic shoulders. However, NCs doped films generally showed strong intensities compared to the reference film and were dependent on the concentration of metal NCs in the medium. According to

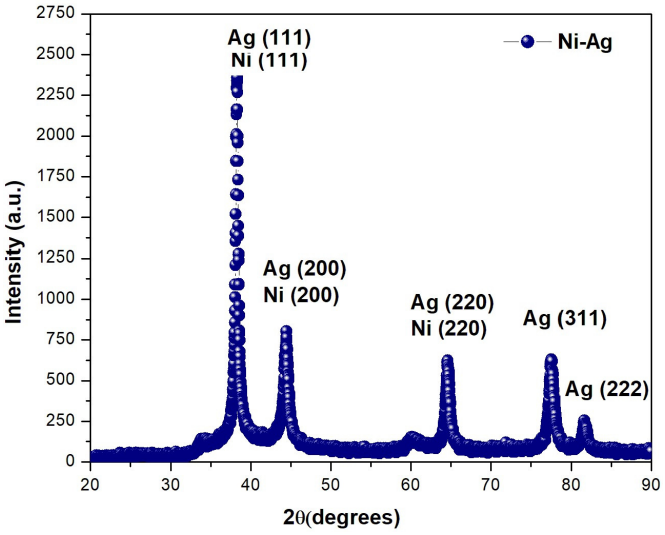

Figure 5.5: X-ray diffraction pattern of Ni/Ag NCs.

Table 5.1: The X-ray diffraction analysis for Ni/ Ag NCs

No	hkl	2θ	β	D	δ	ε	σ
		($\circ$)		(nm)	(10^{-4} nm^{-2})	(10^{-2})	(MPa)
1	38.29	(111)	0.1338	62.84	2.53	2.63	38398
2	44.42	(200)	0.1673	51.29	3.80	2.98	43508
3	64.56	(220)	0.1338	70.22	2.03	1.44	21024
4	77.56	(311)	0.2342	43.51	5.28	1.26	18396
5	81.60	(222)	0.4015	26.13	14.65	1.46	21316

the absorbancy of the Ag/Ni NC provided in Figure. 5.3(a) exhibited absorbency within the range of 350–650 nm, with a peak centered at 460 nm and a tail that extended to the near-infrared region of the electromagnetic spectrum. The broadened absorption of the synthesized NCs implies the existence of multiple sizes and shapes of metal NPs, which is expected to increase the optical extinction coefficient of the solar absorber via photon absorption for small volumes (LSPR modes) and light scattering to the surrounding medium for large sizes.

As expected, the incorporation of Ni/Ag NCs into P3HT:PCBM blends solar absorber significantly enhanced the absorbency and the intensity of the films as presented in Figure. 5.6(a). The spectra from the films clearly showed the signature of Ni/Ag NCs in terms of location and intensity absorption peaks. The absorption spectra of Ni/Ag NCs doped films exhibited changes in peak intensity and FWHM broadening, a blue shift, and damping, due to the occurrence of surface plasmon resonance. The extent of the changes is dependent on the proportion of nickel in the medium, which is in good

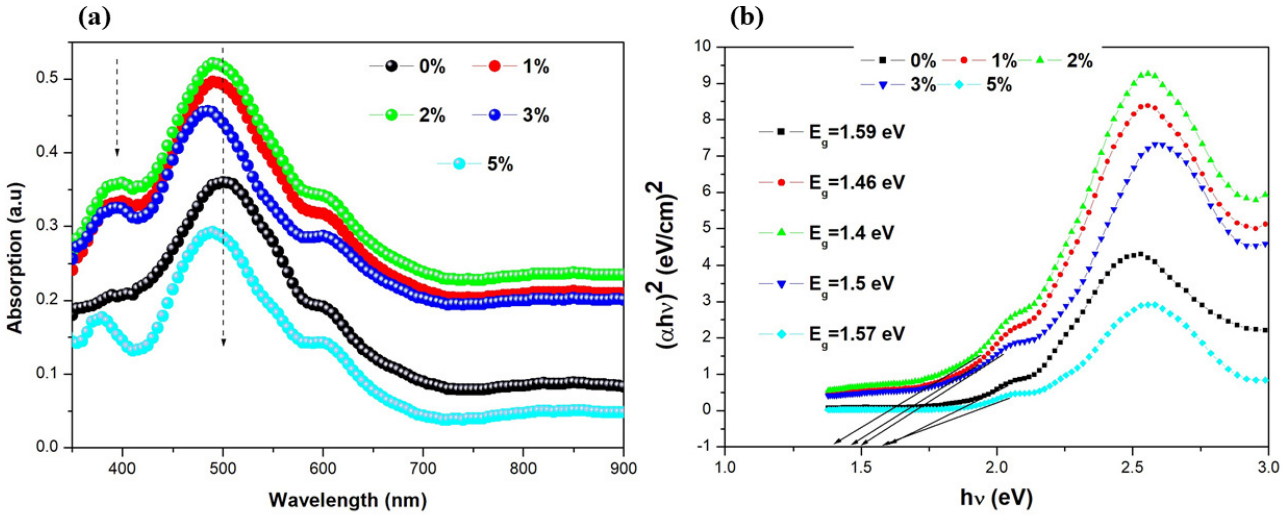

Figure 5.6: a UV-Vis optical absorption results for the pristine and Ni/Ag-doped TFOSCs absorber films. b The optical energy band gap for the reference and Ni/Ag NCs doped solar cells.

agreement with classical predictions, by assuming a Ni-core/Ag-shell geometry. These observations are similar to the findings of Gaudery and co-authors, in which they investigated the optical properties of mixed clusters focusing on the behavior of surface plasmon resonance of Ni/Ag NCs in a spectral range comparable to that of pure silver clusters. Notably, the surface plasmon resonance in Ni/Ag NCs was observed to be considerably broadened by increasing the silver concentration similar to our observations in the absorption spectra of doped samples. Their study also found that the absorption spectra of Ni/Ag NCs tend to be more blue-shifted as the concentration of nickel increases providing a relevant comparison to our study [44]. The new absorption peaks near 400 nm for Ni/Ag NCs solar cells are associated with band-to-band electron transition of silver [45]. Moreover, the presence of the vibronic shoulder of P3HT around 600 nm of wavelength for all doped concentrations of Ni/Ag NCs solar cells suggests that the amount of NCs used in this experiment did not alter the crystal structure of the donor polymer. It is to be noted that the near-field enhancement on the site of NCs is the most dominant effect for Ni/Ag NCs on the fabricated solar cells. This is attributed to the occurrence of LSPR, enhanced exciton dissociation, and light trapping via scattering processes, which collectively improve device performances.

Solar cell performances

The performance of solar cells in converting incident photons into electricity was investigated by analyzing the measured current density–voltage (J–V) characteristic curves using 0.04^2 active area. The J–V curves were taken from solar cells fabricated under different concentrations of NCs in the solar absorber

layer. According to the results presented in Figure. 5.7, it is evident that there is a surge of photocurrent under the influence of NCs in the device structure. The short current density (J_{sc}) significantly high at 1% and 2% of Ni/Ag NCs, but the J_{sc} was slightly decreased at 3%, and then further dropped when the concentration is increased to 5% by weight. These results suggest that the high dopant ratios of metal NCs in the medium have a negative impact on solar cell performance. This is evident in the reduction in PCE from 6.2% to 2.8%, which is accompanied by high series resistance (R_s). The maximum J_{sc} recorded in this experiment was 17.8 (mAm^{-2}) for the 2% Ni/Ag by weight, followed by 15.2 (mAm^{-2}) for both 1% and 3% concentrations. However, the lowest J_{sc} measured in this study was 10.7 (mAm^{-2}) for 5% concentration, which was higher than 10.2 (mAm^{-2}) for the reference solar cell. On the other hand, the fill factor (FF) of the solar cells with the incorporation of Ni/Ag was also increased from 51.2% for 0% to 58.5% and 58.3% for 1% and 2% concentration, respectively. However, the FF at 3% and 5% NC concentration dramatically dropped to 51.0% and 44.2%, respectively. The reduced FF, at 3% and 5% concentrations, would suggest that there must have been leakage currents and charge recombination enhancement in the devices. Thus, the high concentration of the metal NCs in the polymer medium might have caused several defect clusters that promote charge recombinations and prevent free charge collections. The summary of the J–V characteristic data is presented in Table 5.2. The optimum concentration of Ni/Ag NCs in this investigation was found to be 2%, which resulted in the best performance with a PCE = 6.2%. The open-circuit voltage (V_{oc}) measured for the solar cells was observed to increase from 0.62 V for pristine to 0.63 V for 1% and then suddenly dropped to 0.59 V for 2% Ni/Ag NCs concentration. This is due to the interaction of the polymers with the nanoparticles, which resulted in changes in the energy levels that affected the energy band gap. However, as the concentration increases, more Ag/Ni-related defect clusters could have formed that hindered the charge dissociations and transportations. Consequently, this has reduced the measured photocurrent beyond the 2% doping level in a polymer medium. Moreover, higher concentrations of NCs in the absorber layer would result from more metal particles at the interface between the active layer and electrodes causing leakage current [46, 47] and reducing the device FF. This is consistent with the measured data provided in Table 5.2. According to Ohm's law, shunt current increases as shunt resistance decreases, leading to a significant leakage and reduced V_{oc} and FF of the solar cell [48]. Equation12 defines:

$$J_{sh} = \frac{V - JR_s}{R_s h} \tag{5.12}$$

where V is the applied voltage, J is the current density, is the shunt current, and R_s and R_{sh} are the series and shunt resistances, respectively. Moreover, as shown in the result, Table 5.2, the collected series resistances from J–V measurements for 0%, 1%, 2%, 3%, and 5% of Ni/Ag dopant concentrations

Table 5.2: The parameters of P3HT: $PC_{61}BM$-based solar cells fabricated at various Ni doped with Ag NCs concentrations

Ni/Ag(%)	V_{oc}	E_g	E_{loss}(eV)	J_{sc}(mAm^{-2})	FF (%)	PCE%	$R_s(\Omega cm^2)$	$R_{sh}(\Omega cm^2)$
0	0.62	1.59	0.97	10.3	51.2	3.2	9.96	105.1
1	0.63	1.46	0.83	15.2	58.5	5.7	1.86	188.6
2	0.59	1.40	0.81	17.8	58.3	6.2	1.90	171.7
3	0.57	1.50	0.91	15.2	51.0	4.7	9.50	146.8
5	0.59	1.57	0.98	10.7	44.2	2.8	13.69	123.2

range from 1.86 ω cm^2 to 13.69 ω cm^2 , respectively. On the other hand, the values of R_{sh} vary from 105.1 ω cm^2 to 188.6 ω cm^2, in the chosen range of NC concentration. This outcome suggests that an increase in Ni/Ag NCs concentration is unfavorable for the solar cell performances. The effect of Ni/Ag NCs on charge recombination mechanisms was also investigated using the same calculations based on Tauc's model as mentioned in the previous section. The study was based on the general energy losses definition of the solar cells in the form of E_{loss} = E_g - qV_{oc}, where E_g is the optical energy gap of the active thin films, and q is the elementary charge.

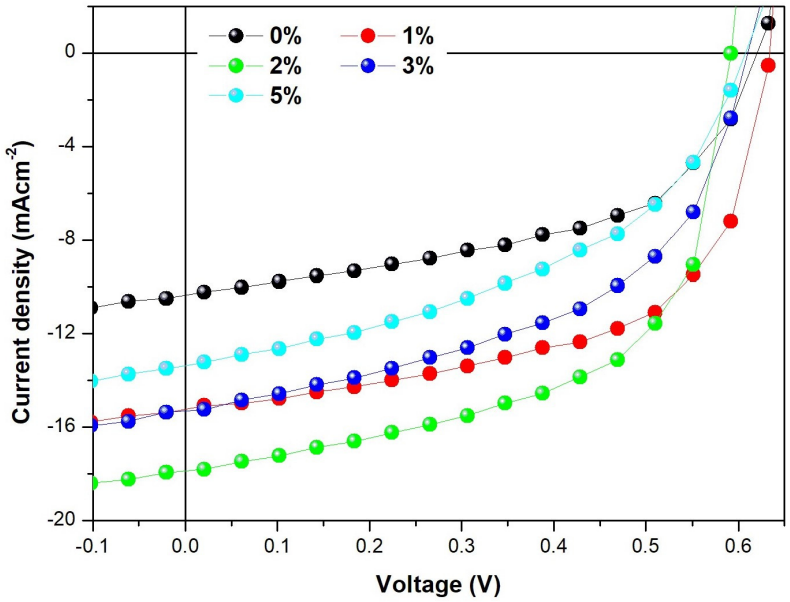

Figure 5.7: J–V characteristics of TFOSC devices at different concentrations of Ni/Ag NCs.

The measured energy gap values for the solar cells with and without Ni/Ag NCs are presented in Figure. 5.6(b). The incorporation of synthesized Ni/Ag NCs was found to be significantly reduced the optical band gap of the fabricated thin films from 1.59 eV to 1.40 eV (see Table 5.2). The energy losses calculated based on these values were found to be ranging from 0.98 eV for the reference to 0.81 eV

2% doping concentrations, respectively. As per the existing literature, solar cells exhibiting low-energy losses tend to perform better, resulting in improved J_{sc}, FF, and higher PCE due to a reduction in charge recombination.

Charge transport properties of the conventional solar cells

The charge transport properties in Ag/Ni-doped polymer solar absorbers were investigated based on the measured space charge limited current (SCLC) under dark conditions. The dark current is an ideal environment by reducing the impact of illumination on the charge transport processes and understanding the true nature of the polymer medium. Figure. 5.8(a) shows lnJ versus V curves taken from newly fabricated solar cell devices, which clearly show high current in dark conditions for NC-doped solar cells. Figure. 5.8(b) displays the SCLC data collected from the forward bias side of the dark current, which started from the injection limited region (1.4 V) of the device and ended at the point where the current reaches saturation. Then, the mobilities of the solar cells were determined via the current density of the devices using Mott–Gurney's law, as provided below (13):

$$J = \frac{9}{8}\varepsilon\varepsilon_0\mu\frac{V^2}{L^3} \tag{5.13}$$

where ε_0 is the permittivity of the free space = 8.85 $\times$ 10^{-12}F/m, ε is the relative permittivity of the medium, μ is the mobility, L is the active layer thickness = 100 nm, V is the voltage drop across the sample which is corrected from the deference between the applied V_{apl}, and build-in voltage V_{bi} [49, 50].

$$V = V_{apl} - V_{bi} \tag{5.14}$$

It is also important to mention that, the mobility μ of the solar cell in Poole–Frenkel's equation [51] is strongly correlated with the electric field across the device as follows:

$$\mu = \mu_0 \exp(\gamma\sqrt{E}) \tag{5.15}$$

where γ is the field activation factor, and μ_0 is the zerofield mobility. The trap-free field-dependent SCLC was then calculated by combining Eqs. (C.15) and (C.13), as given in Eq. (C.16).

$$J_{SCLC} = \frac{9}{8}\varepsilon\varepsilon_0\mu\frac{V^2}{d^3}\exp\left(0.89\gamma\sqrt{\frac{V}{L}}\right) \tag{5.16}$$

The model of Mott–Gurney's assumes constant charge mobility in the medium, free of traps, with an ideal ohmic contact at the cathode and anode. For the pristine solar cell, the resultant zero-field mobility

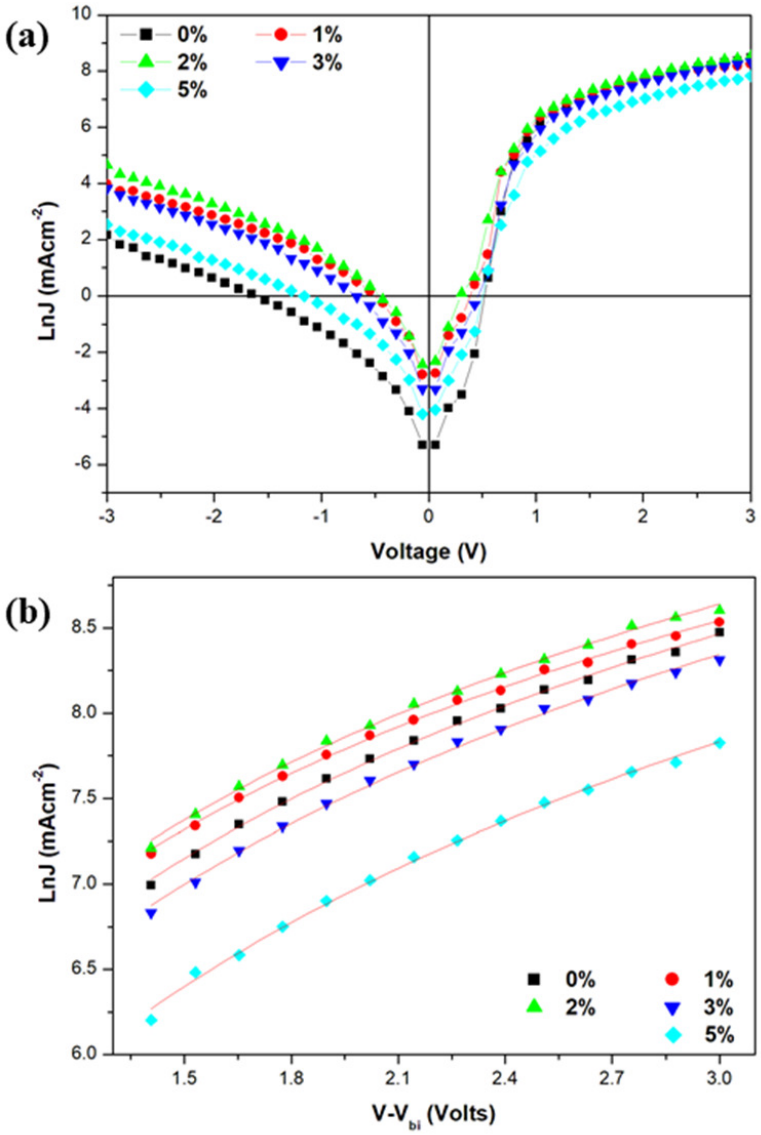

Figure 5.8: a J–V characteristic curve measured under dark conditions at different concentrations and b the space charge limited current (SCLC) of the fabricated devices with/without Ni/Ag NCs.

measured was 1.17×10^{-2} (cm^2 S^{-1} V^{-1}) (see Table 5.3), which is effectively enhanced to 1.67×10^{-3} (cm^2 S^{-1} V^{-1}) and 1.73×10^{-3} (cm^2 S^{-1} V^{-1}) for 1% and 2% NC doping levels, respectively. However, as the concentration of Ni/Ag NC increases to 3%, then the zero-field mobility decreases to 9.32×10^{-4} (cm^2 S^{-1} V^{-1}) and further drops to 4.13×10^{-4} (cm^2 S^{-1} V^{-1}) at 5% NC by weight. It has to be noted here that the higher zero-field mobility leads to better efficiency of the solar cell while lower mobility reduces charge collections as evidenced by the drop in PCE to 2.8% at 5% doping level. Furthermore, the zero-field mobility decreases as the concentration of the metal NCs increases; this suggests that more defect cluster could be formed that prevents the charge transport as the concentration of NC increases beyond the optimum limit. In the case of the reference P3HT:$PC_{61}BM$ photoactive layer,

the effective charge transport process originated from the polymer film morphology. Better polymer morphology would lead to enhanced collection of photocurrent because of good molecular miscibility and large acceptor/donor interfacial area throughout the medium [52]. Thermal annealing is one of the mechanisms to improve polymer crystallization and promote charge transfer between molecules. The discrepancy in mobility between electrons and holes can lead to an imbalance in charge transport, which can increase non-geminate charge recombination in polymer solar cells [53, 54]. The use of plasmonic metal NPs, in a polymer photo-active layer, increases not only the optical absorption of the polymer film but also has a great impact on the charge mobility in the medium. Omrani et al. have reported that plasmonic metal NPs can introduce hopping sites for holes by creating dopant states in the polymer bandgap space and increasing mobility [55, 43]. The solar cell's field activation factor (γ) provided in Table 5.3, is a mathematical parameter utilized to approximate the ratio of charge recombination to that charge generation before collection by the electrodes. A lower value of the γ implies greater mobility of charge carriers, which consequently lowers the probability of non-geminate energy losses inside the polymer medium [43].

Table 5.3: The charge transport parameters for solar cells fabricated at different concentration levels of Ni/Ag NCs

Ni:Ag(wt%)	μ**(cm^2 S^{-1} V^{-1})**	γ**(cm^2 V^{-1})**
0	1.17×10^{-3}	¬ 6.18×10^{-5}
1	1.67×10^{-3}	¬ 8.78×10^{-5}
2	1.73×10^{-3}	¬ 9.18×10^{-5}
3	9.32×10^{-4}	¬ 4.94×10^{-5}
5	4.13×10^{-4}	¬ 2.19×10^{-5}

Table 5.3 summarizes the values of zero-field mobility and field activation factors derived from space charge limited current. The best value of charge mobility recorded in this investigation was 1.73×10^{-3} (cm^2 S^{-1} V^{-1}) at 2% NC concentration in the medium, which corresponds to the best PCE. This clearly indicates the substantial influence of Ni/Ag NCs on the charge transport process, which ultimately boosted the PCE of the solar cells. On the other hand, the left flank of Figure. 5.8(a) representing the reverse saturation current can originate from electrode charge injection or/and thermal generation from the polymer medium, under dark conditions. The current in reverse bias increases till the optimum concentration of Ag/Ni in the solar absorber and then drops at higher doping levels, suggesting that the amount of current even in reverse bias is dependent on improved charge transport processes in the medium. More charges are collected at the optimum doping level, which is consistent with the charge

transport parameters derived from space charge limited current measured in the forward bias and dark condition.

5.4 Conclusion

In conclusion, the incorporation of Ni/Ag NCs in the absorber layer of bulk-BHJ thin-film organic solar cells was found to impact significantly on the optical and electrical properties of the polymer films. Our experimental data demonstrated that the concentration of Ni/Ag NCs played a crucial role in the performance of the solar cells. The highest recorded PCE in this investigation is 6.2% achieved at a 2% weight concentration of Ni/Ag NCs. This is a very good increment in PCE given the nature of the polymer blends used in this investigation. The improvement in solar cell performance is attributed to Ni/Ag NCs local surface plasmon resonance effect that influences both light trapping and charge transport processes. The findings of this study provide valuable insights for future research in the field of organic solar cells and the design of more efficient and cost-effective solar cell devices. Further studies are required to optimize the concentration of Ni/Ag NCs by employing the NCs in different functional layers of the solar cell. It is to be noted that this experiment was conducted under ambient laboratory conditions which is an important development in the realization of TFOSC. Finally, the Ag/Ni is environmentally stable and suitable for roll-to-roll large-scale device fabrication.

References

[1] Hoven C. V., Dang X.-D., Coffin R. C., Peet J., Nguyen T.-Q., Bazan G. C. Improved performance of polymer bulk heterojunction solar cells through the reduction of phase separation via solvent additives. *Advanced Materials*, 2010, **22**(8), E63-E66. Wiley Online Library.

[2] Brabec C. J., Durrant J. R. Solution-processed organic solar cells. *MRS Bulletin*, 2008, **33**(7), 670-675. Springer.

[3] Coakley K. M., McGehee M. D. Conjugated polymer photovoltaic cells. *Chemistry of Materials*, 2004, **16**(23), pp 4533-4542.

[4] Scharber M. C., Mühlbacher D., Koppe M., Denk P., Waldauf C., Heeger A. J., Brabec C. J. Design rules for donors in bulk-heterojunction solar cells—Towards 10% energy-conversion efficiency. *Advanced Materials*, 2006, **18**(6), 789-794. Wiley Online Library.

[5] Dlamini M. W., Mola G. T. Near-field enhanced performance of organic photovoltaic cells. *Physica B: Condensed Matter*, 2019, **552**, 78-83. Elsevier.

[6] Fleetham T., Choi J. Y., Choi H. W., Alford T., Jeong D. S., Lee T. S., Lee K. S., Li J., Kim I. Photocurrent enhancements of organic solar cells by altering dewetting of plasmonic Ag nanoparticles. *Scientific Reports*, 2015, **5**(1), 14250.

[7] Jo J., Na S.I., Kim S.S., Lee T.W., Chung Y., Kang S.J., Vak D., Kim D.Y. Three-dimensional bulk heterojunction morphology for achieving high internal quantum efficiency in polymer solar cells. *Advanced Functional Materials*, 2009, **19**(15), 2398-2406. Wiley Online Library.

[8] Ye L., Zhang S., Ma W., Fan B., Guo X., Huang Y., Ade H., Hou J. From binary to ternary solvent: morphology fine-tuning of D/A blends in PDPP3T-based polymer solar cells. *Advanced Materials*, 2012, **24**(47), 6335-6341. Wiley Online Library.

[9] Wang J., Jia S., Cao Y., Wang W., Yu P. Design principles for nanoparticle plasmon-enhanced organic solar cells. *Nanoscale Research Letters*, 2018, **13**(1), 1-6. Springer.

[10] Kalfagiannis N., Karagiannidis P. G., Pitsalidis C., Panagiotopoulos N. T., Gravalidis C., Kassavetis S., Patsalas P., Logothetidis S. Plasmonic silver nanoparticles for improved organic solar cells. *Solar Energy Materials and Solar Cells*, 2012, **104**, 165-174. Elsevier.

[11] Mandal P., Sharma S. Progress in plasmonic solar cell efficiency improvement: A status review. *Renewable and Sustainable Energy Reviews*, 2016, **65**, 537-552. Elsevier.

[12] Enrichi F., Quandt A., Righini G. C. Plasmonic enhanced solar cells: Summary of possible strategies and recent results. *Renewable and Sustainable Energy Reviews*, 2018, **82**, 2433-2439. Elsevier.

[13] Lee J. M., Kim S. O. Enhancing organic solar cells with plasmonic nanomaterials. *ChemNanoMat*, 2016, **2**(1), 19-27. Wiley Online Library.

[14] Tang M., Sun B., Zhou D., Gu Z., Chen K., Guo J., Feng L., Zhou Y. Broad-band plasmonic Cu-Au bimetallic nanoparticles for organic bulk heterojunction solar cells. *Organic Electronics*, 2016, **38**, 213-221. Elsevier.

[15] Oseni S. O., Mola G. T. Bimetallic nanocomposites and the performance of inverted organic solar cell. *Composites Part B: Engineering*, 2019, **172**, 660-665. Elsevier.

[16] Hamed M. S. G., Adedeji M. A., Zhang Y., Mola G. T. Silver sulphide nano-particles enhanced photo-current in polymer solar cells. *Applied Physics A*, 2020, **126**(3), 207. Springer.

[17] Hamed M. S. G., Mola G. T. Copper sulphide as a mechanism to improve energy harvesting in thin film solar cells. *Journal of Alloys and Compounds*, 2019, **802**, 252-258. Elsevier.

[18] Wang C. C. D., Choy W. C. H., Duan C., Fung D. D. S., Wei E. I., Xie F.X., Huang F., Cao Y. Optical and electrical effects of gold nanoparticles in the active layer of polymer solar cells. *Journal of Materials Chemistry*, 2012, **22**(3), 1206-1211. Royal Society of Chemistry.

[19] Hamdan K. S., Abdullah S. M., Sulaiman K., Zakaria R. Effects of silver nanoparticles towards the efficiency of organic solar cells. *Applied Physics A*, 2014, **115**, 63-68. Springer.

[20] Kaçuş H., Biber M., Aydoğan Ş. Role of the Au and Ag nanoparticles on organic solar cells based on P3HT: PCBM active layer. *Applied Physics A*, 2020, **126**(10), 817. Springer.

[21] Stratakis E., Kymakis E. Nanoparticle-based plasmonic organic photovoltaic devices. *Materials Today*, 2013, **16**(4), 133-146. Elsevier.

[22] Zhong Y., Malagari S. D., Hamilton T., Wasserman D. Review of mid-infrared plasmonic materials. *Journal of Nanophotonics*, 2015, **9**(1), 093791. Society of Photo-Optical Instrumentation Engineers.

[23] Holliday S., Ashraf R. S., Wadsworth A., Baran D., Yousaf S. A., Nielsen C. B., Tan C.H., Dimitrov S. D., Shang Z., Gasparini N., et al. High-efficiency and air-stable P3HT-based polymer solar cells with a new non-fullerene acceptor. *Nature Communications*, 2016, **7**(1), 1-11. Nature Publishing Group.

[24] Cheng C.E., Pei Z., Hsu C.C., Chang C.S., Chien F. S.S. Hole transit in P3HT: PCBM solar cells with embedded gold nanoparticles. *Solar Energy Materials and Solar Cells*, 2014, **121**, 80-84. Elsevier.

[25] Xie F.X., Choy W. C. H., Wang C. C. D., Sha W. E. I., Fung D. D. S. Improving the efficiency of polymer solar cells by incorporating gold nanoparticles into all polymer layers. *Applied Physics Letters*, 2011, **99**(15). AIP Publishing.

[26] Gao H., Meng J., Sun J., Deng J. Enhanced performance of polymer solar cells based on P3HT: PCBM via incorporating Au nanoparticles prepared by the micellar method. *Journal of Materials Science: Materials in Electronics*, 2020, **31**(13), 10760-10767. Springer.

[27] Gollu S. R., Sharma R., Srinivas G., Kundu S., Gupta D. Effects of incorporation of copper sulfide nanocrystals on the performance of P3HT: PCBM based inverted solar cells. *Organic Electronics*, 2014, **15**(10), 2518-2525. Elsevier.

[28] Barnes W. L., Dereux A., Ebbesen T. W. Surface plasmon subwavelength optics. *Nature*, 2003, **424**(6950), 824-830. Nature Publishing Group.

[29] DR B. C. F., Huffman L. Absorption and scattering of light by small particles. Wiley, New York, 1983.

[30] Wang L., Hasanzadeh Kafshgari M., Meunier M. Optical properties and applications of plasmonic-metal nanoparticles. *Advanced Functional Materials*, 2020, **30**(51), 2005400. Wiley Online Library.

[31] Olson J., Dominguez-Medina S., Hoggard A., Wang L.-Y., Chang W.-S., Link S. Optical characterization of single plasmonic nanoparticles. *Chemical Society Reviews*, 2015, **44**(1), 40-57. Royal Society of Chemistry.

[32] Espinosa A., Reguera J., Curcio A., Muñoz-Noval Á., Kuttner C., Van de Walle A., Liz-Marzán L. M., Wilhelm C. Janus magnetic-plasmonic nanoparticles for magnetically guided

and thermally activated cancer therapy. *Small*, 2020, **16**(11), 1904960. Wiley Online Library.

[33] Zhao J., Nguyen S. C., Ye R., Ye B., Weller H., Somorjai G. A., Alivisatos A. P., Toste F. D. A comparison of photocatalytic activities of gold nanoparticles following plasmonic and interband excitation and a strategy for harnessing interband hot carriers for solution phase photocatalysis. *ACS Central Science*, 2017, **3**(5), 482-488. ACS Publications.

[34] Khurana K., Jaggi N. Localized surface plasmonic properties of Au and Ag nanoparticles for sensors: A review. *Plasmonics*, 2021, **16**(4), 981-999. Springer.

[35] Murray W. A., Barnes W. L. Plasmonic materials. *Advanced Materials*, 2007, **19**(22), 3771-3782. Wiley Online Library.

[36] Ahmed A. Y., Ike J. N., Hamed M. S. G., Mola G. T. Silver decorated magnesium doped photoactive layer for improved collection of photo-generated current in polymer solar cell. *Journal of Applied Polymer Science*, 2023, **140**(14), e53697. Wiley Online Library.

[37] Bhatia P., Verma S. S., Sinha M. M. Tunable optical properties of Ni-Ag and Ni-Au nanoparticles in magneto-plasmonic nanostructures. *Optical and Quantum Electronics*, 2020, **52**, 1-12. Springer.

[38] Makuła P., Pacia M., Macyk W. How to correctly determine the band gap energy of modified semiconductor photocatalysts based on UV-Vis spectra. *The Journal of Physical Chemistry Letters*, 2018, **9**(23), 6814-6817. ACS Publications.

[39] Aziz S. B., Abdullah O. G., Rasheed M. A. A novel polymer composite with a small optical band gap: New approaches for photonics and optoelectronics. *Journal of Applied Polymer Science*, 2017, **134**(21). Wiley Online Library.

[40] Mbuyise X. G., Mola G. T. Polycrystal metals nano-composite assisted photons harvesting in thin film organic solar cell. *Solar Energy*, 2020, **208**, 930-936. Elsevier.

[41] Owen E. A., Roberts E. W. Factors affecting the limit of solubility of elements in copper and silver. *The London, Edinburgh, and Dublin Philosophical Magazine and Journal of Science*, 1939, **27**(182), 294-327. Taylor & Francis.

[42] Wang X., Shi L., Zhang J., Cheng J., Wang X. In situ formation of surface-functionalized ionic calcium carbonate nanoparticles with liquid-like behaviours and their electrical properties. *Royal Society Open Science*, 2018, **5**(1), 170732. The Royal Society Publishing.

[43] Mola G. T., Mthethwa M. C., Hamed M. S. G., Adedeji M. A., Mbuyise X. G., Kumar A., Sharma G., Zang Y. Local surface plasmon resonance assisted energy harvesting in thin

film organic solar cells. *Journal of Alloys and Compounds*, 2021, **856**, 158172. Elsevier.

[44] Gaudry M., Cottancin E., Pellarin M., Lermé J., Arnaud L., Huntzinger J. R., Vialle J. L., Broyer M., Rousset J. L., Treilleux M., et al. Size and composition dependence in the optical properties of mixed (transition metal/noble metal) embedded clusters. *Physical Review B*, 2003, **67**(15), 155409. APS.

[45] Hamed M. S. G., Ahmed A. Y., Mola G. T. Suppressing charge recombination in disordered polymers blend medium. *Journal of Physics D: Applied Physics*, 2023, **56**(40), 405101. IOP Publishing.

[46] Qi B., Wang J. Fill factor in organic solar cells. *Physical Chemistry Chemical Physics*, 2013, **15**(23), 8972-8982.

[47] Dhass A. D., Natarajan E., Ponnusamy L. Influence of shunt resistance on the performance of solar photovoltaic cell. In: *2012 International conference on emerging trends in electrical engineering and energy management (ICETEEEM)*, 2012, 382-386. IEEE.

[48] Proctor C. M., Nguyen T.Q. Effect of leakage current and shunt resistance on the light intensity dependence of organic solar cells. *Applied Physics Letters*, 2015, **106**(8). AIP Publishing.

[49] Tessema G. Charge transport across bulk heterojunction organic thin film. *Applied Physics A*, 2012, **106**, 53-57. Springer.

[50] Nardes A. M., Kemerink M., De Kok M. M., Vinken E., Maturova K., Janssen R. A. J. Conductivity, work function, and environmental stability of PEDOT: PSS thin films treated with sorbitol. *Organic Electronics*, 2008, **9**(5), 727-734. Elsevier.

[51] Brütting W., Berleb S., Mückl A. G. Device physics of organic light-emitting diodes based on molecular materials. *Organic Electronics*, 2001, **2**(1), 1-36. Elsevier.

[52] Vanlaeke P., Vanhoyland G., Aernouts T., Cheyns D., Deibel C., Manca J., Heremans P., Poortmans J. Polythiophene based bulk heterojunction solar cells: Morphology and its implications. *Thin Solid Films*, 2006, **511**, 358-361. Elsevier.

[53] Sha W. E. I., Li X., Choy W. C. H. Breaking the space charge limit in organic solar cells by a novel plasmonic-electrical concept. *Scientific Reports*, 2014, **4**(1), 6236. Nature Publishing Group UK London.

[54] Bartelt J. A., Lam D., Burke T. M., Sweetnam S. M., McGehee M. D. Charge-carrier mobility requirements for bulk heterojunction solar cells with high fill factor and external

quantum efficiency¿ 90%. *Advanced Energy Materials*, 2015, **5**(15), 1500577. Wiley Online Library.

[55] Omrani M. K., Fallah H., Choy K.L., Abdi-Jalebi M. Impact of hybrid plasmonic nanoparticles on the charge carrier mobility of P3HT: PCBM polymer solar cells. *Scientific Reports*, 2021, **11**(1), 19774. Nature Publishing Group UK London.

Chapter 6

Application of cobalt-sulphide to suppress charge recombinations in polymer solar cell

Materials Science in Semiconductor Processing 185 (2025) 108917

Contents lists available at ScienceDirect

Materials Science in Semiconductor Processing

journal homepage: www.elsevier.com/locate/mssp

Application of cobalt-sulphide to suppress charge recombinations in polymer solar cell

Abdallah Y.A. Ahmed [a], Abiodun Kazeem Ogundele [a], Mohammed S.G. Hamed [a,b], Newayemedhin A. Tegegne [c], Amit Kumar [d,e], Gaurav Sharma [d,e], Genene Tessema Mola [a,*]

[a] School of Chemistry & Physics, University of KwaZulu-Natal, Pietermaritzburg Campus, Private Bag X01, Scottsville 3209, South Africa
[b] Department of Physics, Faculty of Education, University of Kordofan, El-Obeid 10533, Sudan
[c] Department of Physics, Addis Ababa University, 1176 Addis Ababa, Ethiopia
[d] International Research Centre of Nanotechnology for Himalayan Sustainability (IRCNHS), Shoolini University, Solan, Himachal Pradesh, 173229, India
[e] College of Materials Science and Engineering, Shenzhen Key Laboratory of Polymer Science and Technology, Guangdong Research Center for Interfacial Engineering of Functional Materials, Nanshan District Key Laboratory for Biopolymers and Safety Evaluation, Shenzhen University, Shenzhen 518055, PR China

ARTICLE INFO

Keywords:
Organic solar cell
Bulk-heterojunction
Inverted structure
Active layer
CoS nano-particles

ABSTRACT

Cobalt-sulphide nano-particles were synthesized and employed in absorber layer of thin film organic solar cells (TFOSCs). The incorporation of nano-particles was designed to assist exciton dissociation processes and boost the collection photo-generated currents in TFOSC. Solar cells were fabricated from polymers blend photo-active layer consisting of Poly[[4,8- bis[(2-ethylhexyl) oxy] benzo[1,2-b:4,5-b] dithiophene2,6-diyl] [3 -fluoro-2-[(2- ethylhexyl)carbonyl]thieno[3,4- b] thiophenediyl]] (PTB7)and [6,6]-phenyl C_{71}-butyric acid methyl ester ($PC_{71}BM$) with/without the incorporation CoS. The optical and electrical properties of the active layers are found to be highly impacted by the inclusion of CoS NPs in the medium. Consequently, significant improvement on the collection of photo-currents was recorded that led to high power conversion efficiency of the devices compared to the reference cell. The influence of CoS nano-particles is found to be dependent on its concentration in the medium where the best solar cell performance recorded, in this experiment, was at 1wt% CoS, which brings about an increase in efficiency by 37%.

Chapter 6

Application of cobalt-sulphide to suppress charge recombinations in polymer solar cell

Abstract

Cobalt-sulphide nano-particles were synthesized and employed in absorber layer of thin film organic solar cells (TFOSCs). The incorporation of nano-particles was designed to assist exciton dissociation processes and boost the collection photo-generated currents in TFOSC. Solar cells were fabricated from polymers blend photo-active layer consisting of Poly[[4,8- bis[(2-ethylhexyl) oxy] benzo[1,2-b:4,5-b] dithiophene2,6-diyl] [3 -fluoro-2-[(2- ethylhexyl)carbonyl]thieno[3,4- b] thiophenediyl]] (PTB7)and [6,6]-phenyl C_{71}-butyric acid methyl ester ($PC_{71}BM$) with/without the incorporation CoS. The optical and electrical properties of the active layers are found to be highly impacted by the inclusion of CoS NPs in the medium. Consequently, significant improvement on the collection of photo-currents was recorded that led to high power conversion efficiency of the devices compared to the reference cell. The influence of CoS nano-particles is found to be dependent on it's concentration in the medium where the best solar cell performance recorded, in this experiment, was at 1wt% CoS, which brings about an increase in efficiency by 37%.

Keywords: *organic solar cell, bulk-heterojunction, inverted structure, active layer, CoS nano-particles.*

6.1 Introduction

Organic semiconductor-based solar cells are gaining attention due to their low material usage, simple device fabrication processes, light weight and large-area solar panel production [1]. In the last three decades, several conjugated polymers have been synthesised and tested for different functional layers of TFOSC. Conjugated polymers are macro-molecules with molecular weight exceeding 10,000 atomic mass units [2]. However, the ideal material is yet to be developed due to challenges such as inherent high exciton binding energy in polymer and environmental instability. For instance, the exciton binding energy for organic semiconductors is approximately one order of magnitude higher than those of inorganic semiconductors like silicon. Consequently, the photo-excitations in silicon solar cell can easily produce free charge carriers at room temperature. However, there are insufficient free charge carriers available in an organic semiconductor medium at room temperature ($\sim$ 25 meV), through exciton dissociation, even under typical internal electric fields ($\sim$ 10^6 - 10^7 V/m) [3]. The quest to solve these challenges led to the development of new solar absorber design through the discovery of bulk heterojunction (BHJ) solar cell. BHJ offers a key benefit by forming a large donor/acceptor inter-facial network, serving as centres for exciton dissociation into free-charge carriers [4]. In a BHJ design, the conversion of solar energy to photocurrent involves a series of complex processes, starting with the generation of excitons upon light absorption. This is followed by migration of exciton towards interfacial region, where they are dissociated into free electron-hole pairs. The resulting free charge carriers are then extracted and transported toward their respective electrodes [5, 6]. Several parameters play critical factor for the success of BHJ design such as morphology of the photo-active film, the stoichiometric ratio of donor/acceptor molecules and the selection of transport buffer layers in reducing charge recombination. Optimization of these parameters is still not sufficient enough to harvest all the incident photons because of the required thin polymer absorber layer ($\leq$ 200nm) to minimize charge recombinations. Increasing the active layer thickness can lead to enhanced light absorption consequently generate more excitons [7], however, this resulted in an increase in the bulk resistance which in turn promotes charge recombination losses [8] as well as reduce the hole mobility [9, 10]. Thus, enhancing optical absorption in thin polymer films becomes crucially important using alternative options to improve energy harvesting. To address the challenge, researchers have explored various ways to incorporate light-trapping mechanisms to enhance optical absorption. These methods include but not limited to the use of photonic crystals [11], optical spacer layers [12], diffraction gratings [13], and more recently, the incorporation of metal nano-particles [14]. As such, various metal/semiconductor sulfide nano-particles, such as nickel sulfide [15], zinc sulfide [16], copper sulfide [17], and potassium sulfide [18], have been reported to have positive impacts on device performances (see Table 6.1). For example, copper sulfide and nickel sulfide are frequently

Table 6.1: The summary of previous research on metal NPs and their corresponding efficiency progresses in organic solar cells.

Device architecture:	**NPs**	**NPs Location**	**PCE(%) without NPs**	**PCE(%) with NPs**	**Ref**
ITO/PEDOT: PSS/P3HT:PCBM:NPs/LiF/Al	Ag:Mg	P3HT:PCBM	2.29	4.11	[31]
ITO/ZnO/PTB_7:PCBM/MoO3/Ag	Ag	ZnO	6.53	7.25	[33]
ITO/PEDOT:PSS/QD/P3HT:PCBM/LiF/Al	CdTeSe	PEDOT:PSS	2.30	4.87	[34]
ITO/ZnO/P3HT:PC61BM-LaPO4: Ag/MoO3/Al	LaPO4: Ag	P3HT:PCBM	2.33	5.23	[35]
ITO/ PEDOT: PSS-NiS/P3HT:PCBM/LiF/Al	NiS	PEDOT: PSS	3.09	6.03	[15]
ITO/PEDOT/PSS:Ag/Co/ P3HT:PC61BM/LIF/Al	Ag:Co	PEDOT: PSS	2.53	4.21	[36]
ITO/PEDOT:PSS/P3HT:PCBMNP/LiF/Al	ZnS	P3HT:PCBM	1.90	4.00	[37]
ITO/PEDOT:PSS:CuS/P3HT:PC61BM/LiF/Al	CuS	PEDOT: PSS	2.01	4.51	[38]
ITO/PEDOT:PSS/P3HT:PCBM-ZnO: Cd/LiF/Al	ZnO:Cd	P3HT:PCBM	2.54	4.67	[39]
ITO/PEDOT:PSS:Au/PTB_7:$PC_{71}BM$/Ca	Au	PEDOT: PSS	7.50	8.10	[40]
ITO/Au@PDA/ZnO/PTB_7:$PC_{71}BM$/MoO3/Al	Au@PDA	ZnO	4.64	6.03	[41]
ITO/ZnO/Y2O3/PTB_7:$PC_{71}BM$/MoO3/Ag	ZnO/Y2O3	ZnO	5.77	6.22	[42]
ITO/PEDOT:PSS/PTB_7:$PC_{71}BM$/Ca/Al	Au@Ag@SiO2	PEDOT:PSS	7.72	9.04	[43]
ITO/PEDOT:PSS/PTB_7:$PC_{71}BM$/Ca/Al	Au@Ag@SiO2	PTB_7:$PC_{71}BM$	7.72	9.56	[43]

employed as p-type hole transport layers in TFOSCs, and as dopants in perovskite solar cells [19].

Furthermore, metal chalcogenides compounds often exhibit an interesting optical and electrical properties [20, 21, 22, 23, 24], which are important for the development of photonic devices, and energy storage amongst others. Some of these materials have low energy bandgap ($\sim$ 1.7 eV for CdSe) with enhanced light-harvesting coefficient exceeding 10^4 cm^{-1} making them an attractive materials in thin film polymer solar cells [25]. Cobalt sulphide is a II-VI semiconductor material often used as photocatalyst as reported in literatures [26, 27]. However, the nano-scale (1 to 10 nm) size of CoS NPs exhibits quantum confinement effect, which is highly relevant to solar energy harvesting [28]. CoS NP has gained intensive research as light absorber material for solar cell applications, as anode in lithium-ion batteries, catalysts, and ultra-high density magnetic recording [29]. Furthermore, CoS is an easily accessible material, low-cost with an excellent work function that matches very well to PEDOT:PSS, making it a promising hole-collecting material [30]. In this study, CoS NPs have been employed for the first time in PTB7:$PC_{71}BM$ polymers blend active layer to improve the solar cells efficiency. The inclusion of the CoS in a polymer blend solar absorber has positively influenced the optical absorption of the absorber

film and consequently enhanced the device parameters as discussed in the following sections.

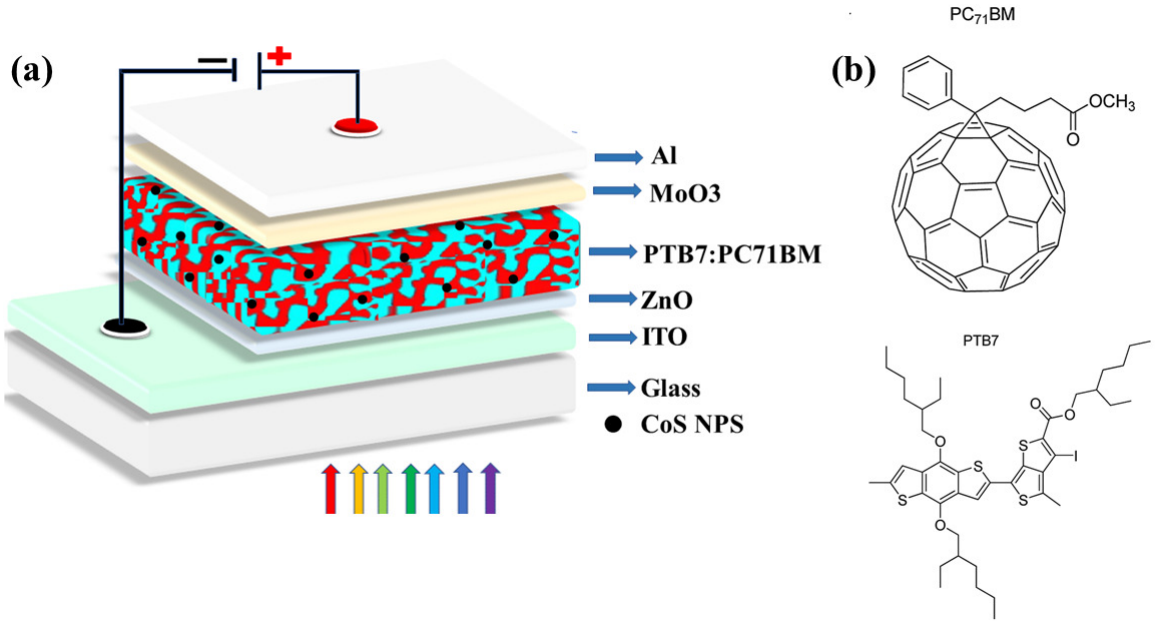

Figure 6.1: (a) Inverted solar cells device structures used in this experiment, and (b) the structure of the fabricated polymer materials [32].

6.2 Materials and methods

6.2.1 Materials

The materials for the synthesis of CoS NPs were sourced from the chemical suppliers listed. Cobalt (II) nitrate hexahydrate $(Co(NO_3)_2).6H_2O$, thiourea (99.0%), and Polyvinylpyrrolidone (PVP) were purchased from Sigma Aldrich used as received. The polymers used are Poly[[4,8-bis[(2-ethylhexyl) oxy] benzo[1,2-b:4,5-b] dithiophene-2,6-diyl] [3-fluoro-2-[(2- ethylhexyl)carbonyl]thieno[3,4-b] thiophenediyl]] (PTB_7) as an electron donor and [6,6]-phenyl C_{71}-butyric acid methyl ester ($PC_{71}BM$) as an electron acceptor, all were purchased from Ossila Ltd (UK). Chlorobenzene, 1,8-diiodooctane (98.0%) solvent, and zinc oxide were also procured from Sigma Aldrich.

6.2.2 Synthesis of Cobalt sulphide NPs (CoS)

The synthesis of CoS NPs was carried out using wet chemistry as reported in the literature [37]. First, 0.5 M cobalt nitrate hexahydrate was dissolved in 50 mL of deionized water in a glass beaker, with stirring maintained until the compound was completely dissolved. The second precursor was prepared by dissolving 0.5 M (CH_4N_2S) in 50 mL of deionized water, followed by the addition of 3.0 g of PVP in a separate beaker. The mixture was stirred until all the solute components are dissolved. Subsequently,

the thiourea solution was slowly added drop wise into the cobalt nitrate solution while stirring at room temperature. The resulting precipitate was filtered under reduced pressure and washed multiple times with distilled water and ethanol to eliminate any residual of sodium ions. Finally, the resulting CoS NPs were dried in an oven at 100°C for 2 hours.

6.2.3 Solar cells fabrication

The solar cell fabrication started by partially etching the unpatterned ITO-coated glass substrates using acid solution composed of a mixture of HCl, H_2O, and HNO_3. The substrates were sequentially cleaned in ultrasonication bath, using deionized water, isopropanol, and acetone, each for a duration of 10 minutes. Thereafter, the cleaned substrates were dried at 90°C in an oven before layering of the electron transport layer (ETL) through spin coating of ZnO ink suspension at 4000 rpm. After drying the ETL at 100°C for 20 minutes in a nitrogen environment, the samples were coated with solar absorber layer at 1200 rpm. The active layer solution composed of PTB7:PC_{71}BM blend dispersed in chlorobenzene solvent at a 1:1.5 ratio by weight with/without CoS NPs. The CoS NPs were doped into active layer at different concentrations (0%, 1%, 3%, and 5%) by weight of the polymers blend. The mixture was sonicated overnight at room temperature and spin coated on the substrates at 1200rpm. The samples were further dried in the furnace at 60°C for 30 minutes under a nitrogen atmosphere. Finally, the hole transport layer (MoO_3(0.4 nm) and the top (Al) electrode (80 nm)) were deposited onto the dried active layers at atmospheric pressure of (10^{-6} mbar), using an Edward 306 vacuum deposition unit. An inverted BHJ architecture consisting of various layers of materials, such as Glass/ITO/ZnO/PTB_7:PC_{71}BM:CoS-NPs/MoO_3/Al was fabricated (see Figure. 6.1 left). The UV-Vis absorption spectra analysis was conducted using a photo-spectrometer (Rayleigh 1601) to study the optical properties of the absorber layers. Finally, the current density-voltage (J-V) data were collected using a computer-controlled Keithley HP2420 source meter and a solar simulator (model SS50AAA) operating under AM1.5 conditions at an intensity of 100 mW/cm^2.

6.3 Results and discussion

6.3.1 Optical Properties of CoS NPs and Absorber films

The optical and morphological properties of the newly synthesized CoS nano-particles and absorber films were studied using UV-Vis spectrometer, transmission and scanning electron microscopies (TEM & SEM), and energy-dispersive X-ray analysis (EDX).

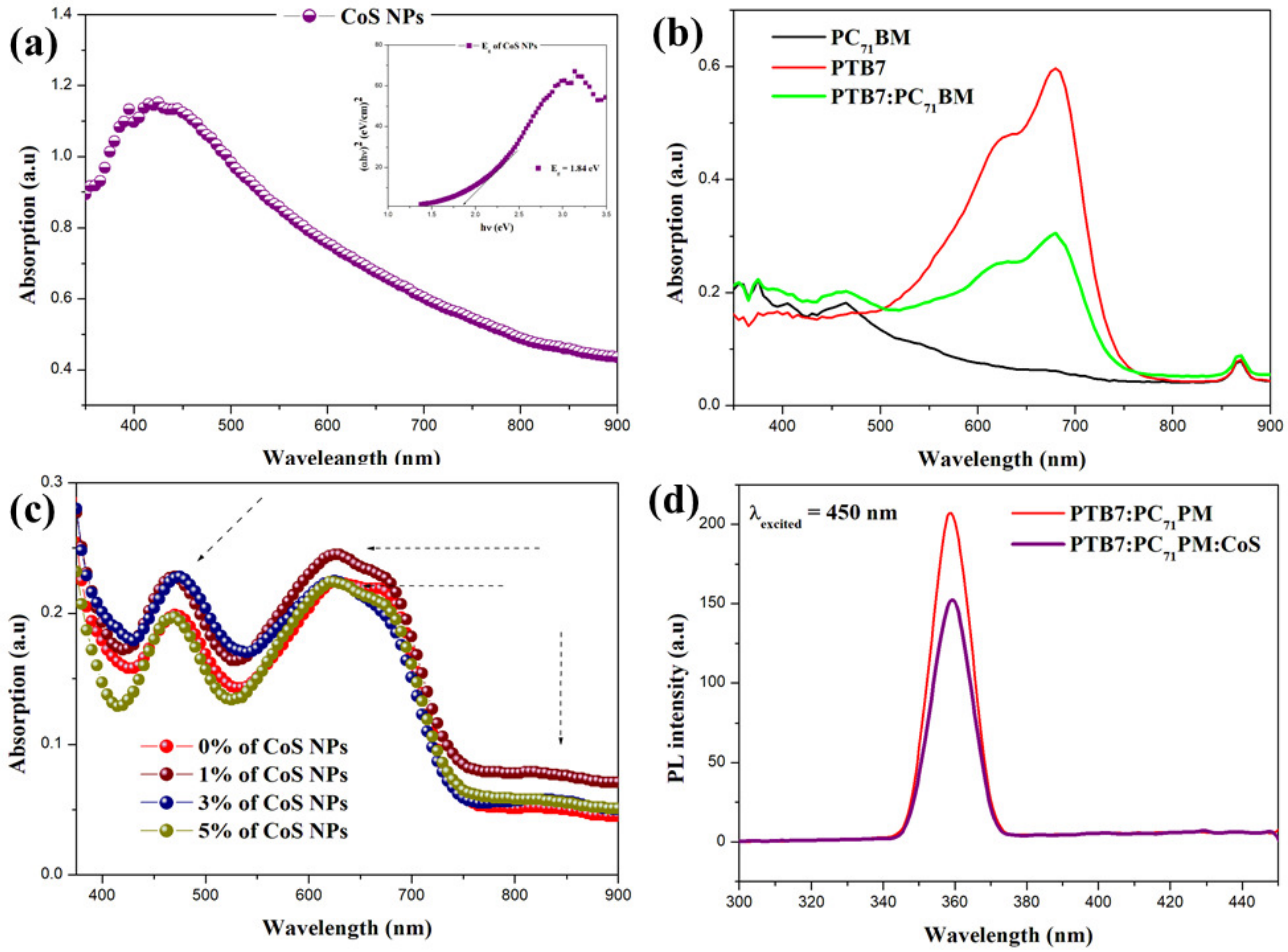

Figure 6.2: (a) Optical absorption and energy band gap (inset) for CoS NPs powder dispersed in deionized water, (b) UV-bis absorption spectra of polymers PTB7, $PC_{71}BM$, and PTB7:$PC_{71}BM$ solutions, (c) UV-bis absorption taken from pristine and CoS NPs doped absorber films, and (d) Photoluminescence (PL) spectrum of PTB7:$PC_{71}BM$ with and without CoS doped films after photoexcitation at 450 nm.

CoS Nanoparticles

The optical absorbancies measured from CoS NPs powder in deionized water, is shown in Figure 6.2(a). The absorbency of CoS fall within the range of 350 – 700 nm, with a peak centred around 450 nm. Furthermore, a tail extending to the near-infrared region of the electromagnetic spectrum was observed. This notable broadening of optical absorption of the synthesized NPs is due to light scattering in the water medium, which is a positive indication of possible light trapping in PTB7:$PC_{71}BM$ solar absorber medium. Moreover, the absorption coefficient peak at about 425 nm NP indicates its capability to harvest high energy photons due to inherent quantum confinement effect. Tauc's plot was employed to determine the energy band gap using the measured absorbencies, as shown in the inset of the Figure 6.2(a). Tauc's equation, as presented in eq.(7.1), depends on the absorption coefficient (α) and, energy

band gap (E_g) of the material under investigation.

$$\alpha\beta = \gamma(h\upsilon - E_g)^n \tag{6.1}$$

where β denotes the photon's energy, calculated as $\beta = hc/\lambda$, where h is a Planck's constant, c is the speed of light, and λ is the wavelength of the photon. The parameter γ is a constant characterizing the optical frequency range, the index n which follows the indirect transition in our analysis, is generally used describes the electronic transition conditions with a value of 1/2 for direct band to band transitions or 2 for indirect transitions. By analysing the plot of ($\alpha h\upsilon$) versus ($h\upsilon$) and extrapolating a tangent line to the horizontal axis where $(\alpha h\upsilon)^2 = 0$, the optical energy gap was determined to be 1.84 eV. This value of the optical band gap suggest the material is indeed semiconductors and expected to have a positive influence on the solar energy harvesting capabilities of the modified photo-active layers.

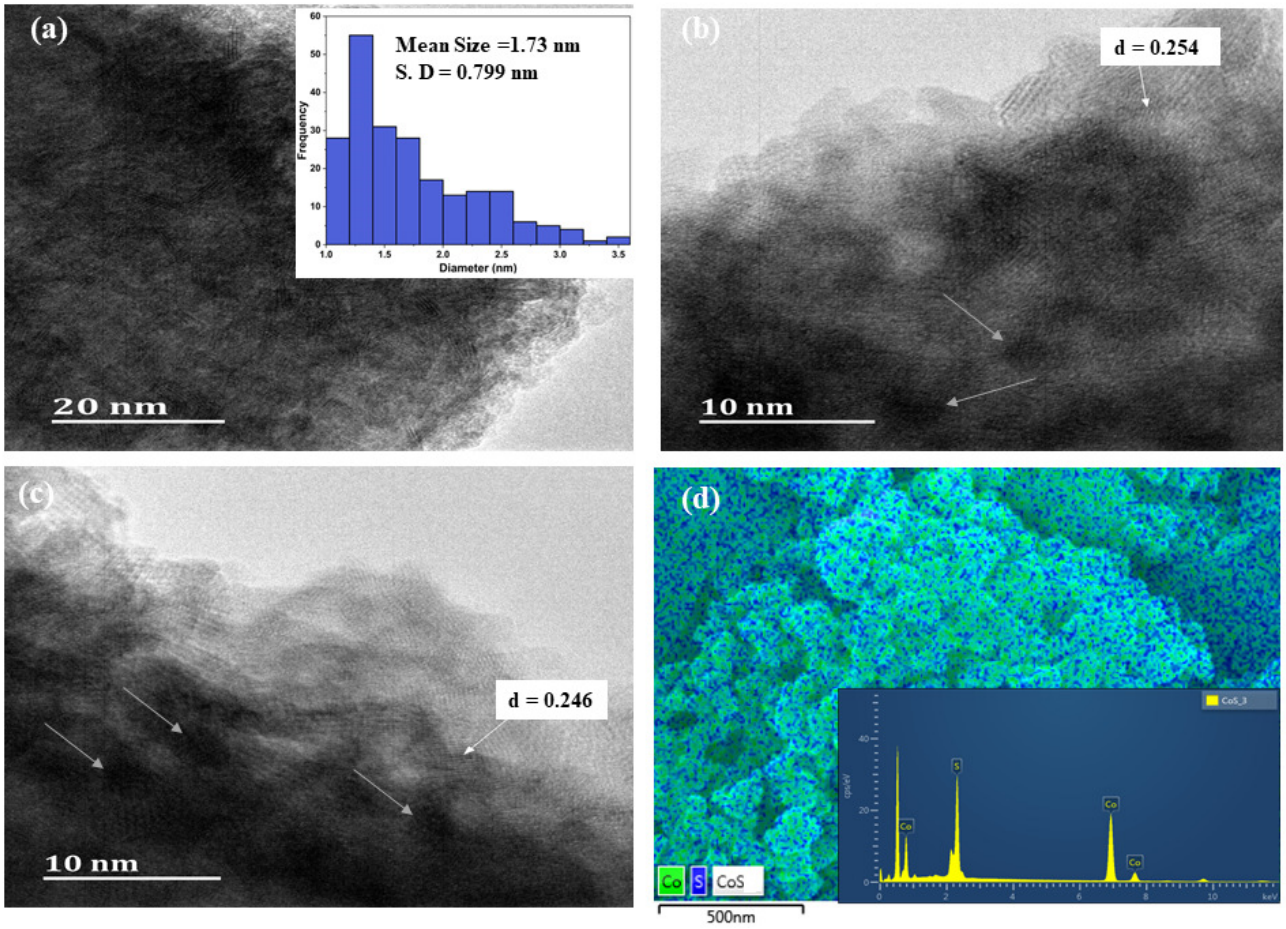

Figure 6.3: (a) and (b) Scanning electron microscopy, (c) Scanning electron microscopy with energy dispersive X-ray (inst), and(d) Transmission electron microscopy images for CoS NPs powder.

Solar absorbers films with/without CoS NPs

The optical properties of the polymers blend films under study were investigated both in liquid and solid phases. The absorption spectra given in Figure 6.2(b) represents the absorbencies of the polymers in the solution form while the spectra taken from the films are provided in Figure 6.2(c). According to the spectra in Figure 6.2(b), the PTB7 polymer has absorbency ranging from 500 nm to 700 nm, which contains two prominent absorption shoulders centred at 624 nm and 676 nm, respectively. These peaks are characterized by 0-1 and 0-0 electron transitions in the PTB7 polymer molecules, respectively. The 0-1 corresponds to the transition from the ground state to the first vibrational excited state energy level, while the 0-0 stands for the electron transition from the ground state to the lowest excited state of the polymer molecule [44, 45]. Moreover, the intensity of the 0-1 vibronic shoulder is linked to the inflexibility and co-planarity of the π-conjugated backbone of the PTB7 polymer. Whereas the 0-0 transition peak intensity reflects the strength of π-π stacking interactions and the degree of polymer aggregation. Thus, the 0-0 transition is more pronounced in solution compared to 0-1 suggesting more aggregation in solution, which remain the same even in PTB7:$PC_{71}BM$ blend solution. However, the peak intensity of the vibronic shoulder appear to be more pronounced in the films contrary to the spectra taken from solution. This suggest that there is more co-planarity and crystallity of PTB7 in the film than in the solution [46].

The absorber layers containing CoS NPs also showed a notable alteration in absorption patterns, including red shift of peak and enhanced absorption after 800 nm. These observations are in good agreement with the behaviour of CoS NPs dispersed in deionized water due to light scattering, as provided in Figure 6.2(a). There is a prominent absorption peak of CoS NPs which ranges between 350 nm and 500 nm, along with extended absorption beyond 850 nm into the infra-red region. According to the information presented in the Figure 6.2(c), the absorption spectra of the films consists of two broad peaks centred near 470 nm and 625 nm, respectively. The peak close to 470 nm is attributed to the presence of CoS in polymer film medium, which is absent in the absorbency of the polymer blend in a solution. This trait exhibited by CoS NP can be linked to the size-dependent emission of quantum dot. The absorption range from $600-700$ nm is coming from PTB7 as it is evident from discussion of the absorbency the polymer solution (see Figure 6.2(b)). The modified polymers blend films containing CoS NPs their molecular packing order enhanced at the 0-1 vibronic transition compared to the pure PTB7 film, which can assist in the charge transport processes. On the other hand, the 0-0 vibronic transition intensity for the film with a 1% concentration of CoS NPs was slightly increased compared to the pristine film. However, the 0-0 vibronic transition intensities for the rest of the films remained below that of the reference film indicating the low π-π stacking interactions for higher concentrations

of CoS NPs. The combined effects of these changes in optical absorption contribute to the enhanced photocurrent generation in CoS-doped devices, thereby, improving overall device performance.

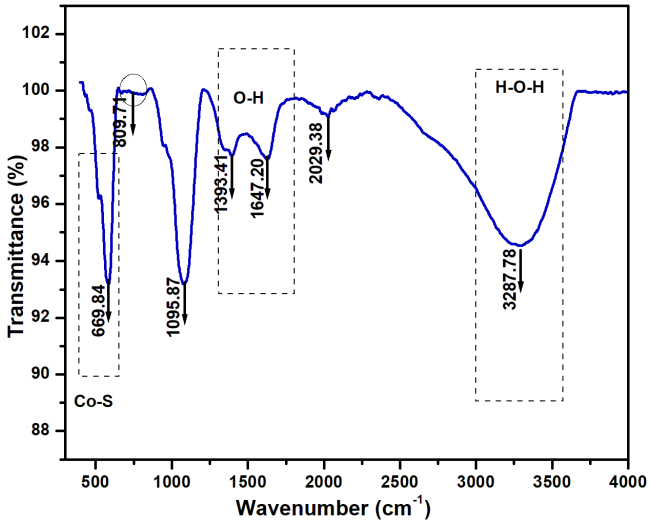

Figure 6.4: FTIR spectrum of CoS NPs.

Furthermore, photo-luminescence (PL) measurements were conducted on the recently fabricated absorber films consisting of PTB7:$PC_{71}BM$ polymers blend with and without CoS NPs. The PL spectra were measured at room temperature as provided in Figure 6.2(d). The films were exited by the illumination of radiation at a wavelength of 450 nm, (see Figure 6.2d). The PL emission was observed at pronounced peaks of 360 nm for both pristine and CoS doped films. According to the figure provided in Figure 6.2(d) photoluminescence intensity quenching was observed from the film doped with CoS NPs. This reduction in the emission intensity is due to the enhanced charge separation at the interface due to the presence of the NPs [47]. The PL intensity of the pristine PTB7:$PC_{71}BM$ film is much stronger than the doped film under the same excitation condition. However, the pristine film displays strong PL emission with an emission peak at 380 nm. The photo-luminescence data taken from PTB7:$PC_{71}BM$ with/without CoS films clearly showed better charge dissociations with CoS NPs as evidenced by quenching of the PL intensity compared to the film without NPs [48].

6.3.2 Morphological properties of CoS NPs

The surface morphology and micro structures of CoS NPs were studied using scanning and transmission electron microscopies (SEM & TEM), respectively. The TEM images depicted in Figure 6.3(a-c) reveals that the NPs exhibited a relatively uniform distribution in terms of size and shape, with elliptical and quasi-spherical geometries being prominent. The images also suggest possible formation of core-shell structure. This is evident from the TEM images provided in Figure 6.3(a-c) indicating a dark core surrounded by light coloured regions. Also, the size of NPs range from 1 to 4 nm as analysed and

observed from the HRTEM images (see inset of Figure 6.3(a)). According to literatures based on the study of CoS, these structures are often described as nano-cages [49, 50, 51], which are reported to have significant impact on the performance of dye-sensitized solar cells by enhancing catalytic activity, electrical conductivity, and the surface morphology of the film for a tiny-sized nano-cage. Such enhanced performance of the solar cell was attributed to the crystalinity and the large surface area of CoS nano-cages [52]. The elemental analysis conducted using the SEM and energy dispersive X-ray (EDX) data provided in Figure 6.3(d), indicates a uniform distribution of sulfur and cobalt throughout the medium, supporting the formation of the CoS phase-composite. Moreso, the crystalline nature of the NPs is also visible from the well-aligned fringes observed in the TEM images in Figure 6.3(b and c) with lattice spacing, d = 0.254 and 0.246 nm (2.54 Å, and 2.46 Å). These d-spacings are typical of CoS phase with hexagonal shape as previously reported [53, 54]. The variations in size and shapes of the synthesized CoS NPs are expected to display multiple functions by improving the optical, and electrical properties as well as the surface morphology of the thin film. For instance, the smaller sizes of CoS NPs are expected to have great influence on the device performance by capturing high energy photons, while the relative larger sizes harvest photons in the visible and near infrared regions. According to Sibokoza et al. the optical absorption properties of CoS NPs are significantly influenced by their size and morphological characteristics [29]. Our experiment is consistent with the findings when the CoS NPs dispersed in deionized water (Figure 6.2(a)) showed different sizes as derived from TEM images (Figure 6.3(a) inset). This ultimately enhances energy harvesting through the size-dependent quantum confinement effect [55, 56]. Fourier Transform Infrared (FTIR) spectra provided in Figure 6.4) was obtained from CoS NPs powder suspension. The spectrum revealed the molecular compositions and structure of the NPs powder. For instance, a band centered around 810 cm^{-1} is attributed to the vibrational mode of the Co-S bond [59]. Whereas the range of absorption is from 1300 to 1500 cm^{-1} [60] depicts the stretching of C-H and bending of C-O-H bonds. The bending and stretching vibrations of the O-H group led to the resultant peaks at 1095.87 and 3287.78 cm^{-1} [61]. This data is indeed another confirmation of the formation of CoS NPs.

6.3.3 Device characterizations

J-V characteristics of devices with/without CoS NPs

The current-voltage characteristics (J-V) of the solar cells, provided in Figure 6.5, shows the electrical behaviour of devices fabricated with and without the incorporation of CoS in the PTB7:$PC_{71}BM$ solar absorber. Generally, solar cells containing NPs in the absorber layer exhibited significant enhancements in PCE due to increased measured photo-currents. According to Figure 6.5, a notable increase in the short circuit current density of the doped film are clearly observed, which are attributed to the presence

of metal NPs in the PTB7:$PC_{71}BM$ blend compared to pristine devices as detailed in Table 6.2. It is evident that the improved performance was found to be dependent on CoS NPs concentrations in the medium.

Table 6.2: The parameters of PTB7:$PC_{71}BM$-based solar cells fabricated at various CoS concentrations.

	As Fabricated					After 24 Hours				
CoS NPs (%)	**V_{oc}** (V)	**J_{sc}** ($mAcm^2$)	**FF** (%)	**PCE** (%)	**R_s** (Ω)	**V_{oc}** (V)	**J_{sc}** ($mAcm^2$)	**FF** (%)	**PCE** (%)	**R_s** (Ω)
0 wt%	0.63	16.50	43.30	4.53	381.00	0.56	15.90	40.40	3.55	1115.45
1 wt%	0.72	19.10	46.00	6.20	100.00	0.66	16.60	45.80	5.02	110.32
3 wt%	0.71	18.10	45.00	5.20	307.00	0.68	16.50	43.90	4.94	501.02
5 wt%	0.68	15.80	44.47	4.64	501.00	0.58	13.50	43.30	3.41	981.27

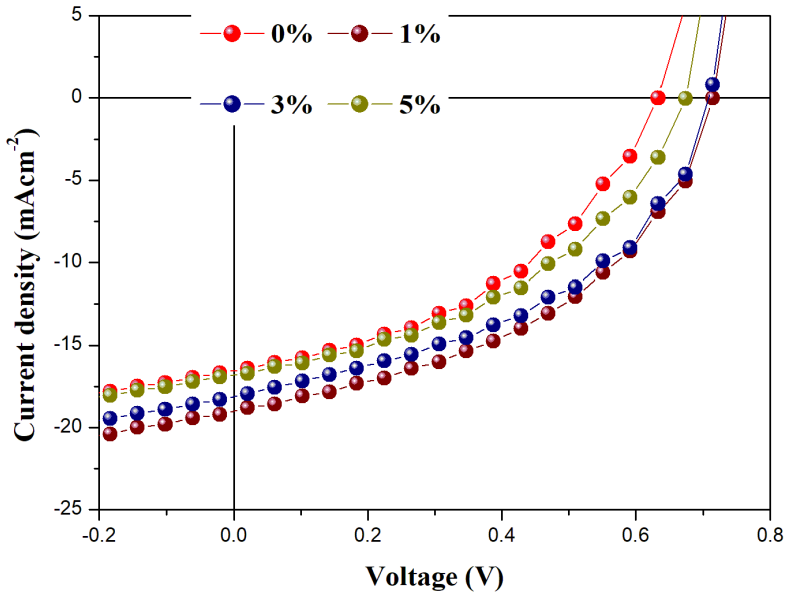

Figure 6.5: *J-V* characteristics of TFOSC devices at different concentrations of CoS NPs.

Notably, there are changes on the magnitude of the open circuit voltage (V_{oc}), where maximum of 0.72 volts was measured from a device containing an optimum 1% CoS NPs while it was 0.63 volts for the reference solar cell. This enhancement in V_{oc} of PTB7:$PC_{71}BM$ based solar cell suggest that the incorporation of CoS NPs not only enhances the optical absorption of the thin films but also improves inter-facial conditions between active layers and electrodes. According to the current experiment a maximum J_{sc} of 19.1 $mAcm^{-2}$ was measured at 1% NPs concentration, which dropped to 15.8 $mAcm^{-2}$ at 5% NPs. Despite the visible enhancements of the observed short-circuit current, the recorded FF for

all the solar cells are generally low relative to the values of other device parameters. This influence could be attributed to the slightly increased active layer thickness ($\simeq$ 180 nm) of the photo-active layer and low crystalline behviour of PTB7 in BHJ. According to some reports, an active layer thickness close to 100 nm can lead to high FF provided there are good morphology control mechanisms in PTB7:$PC_{71}BM$ based solar cells [62]. This is due to the fact that PTB7 is widely known for not crystallizing in BHJ film in contrast to P3HT, which leads to PTB7-rich and $PC_{71}BM$-rich phase segregation [63]. In general, several techniques can be used in the fabrication of polymer solar cells to improve FF including controlling morphology, active layer thickness, select suitable transport buffer layer materials to prevent leakage current, or contact resistance [64, 65, 62]. The best device performance recorded in the current investigation is (1 wt% CoS NPs)concentration with PCE of 6.20%. However, higher concentration of NPs in absorber layer led to reduced device performance as evident in 5 wt% doping level where the efficiency dropped to 4.64%. High concentration NPs in polymer medium could result in the formation of large CoS nano-clusters impeding current flow in the medium and reducing the fill factor of the devices. This is conspicuous from the measured high series resistance of 5% CoS NPs doped solar cells (see Table 6.2).

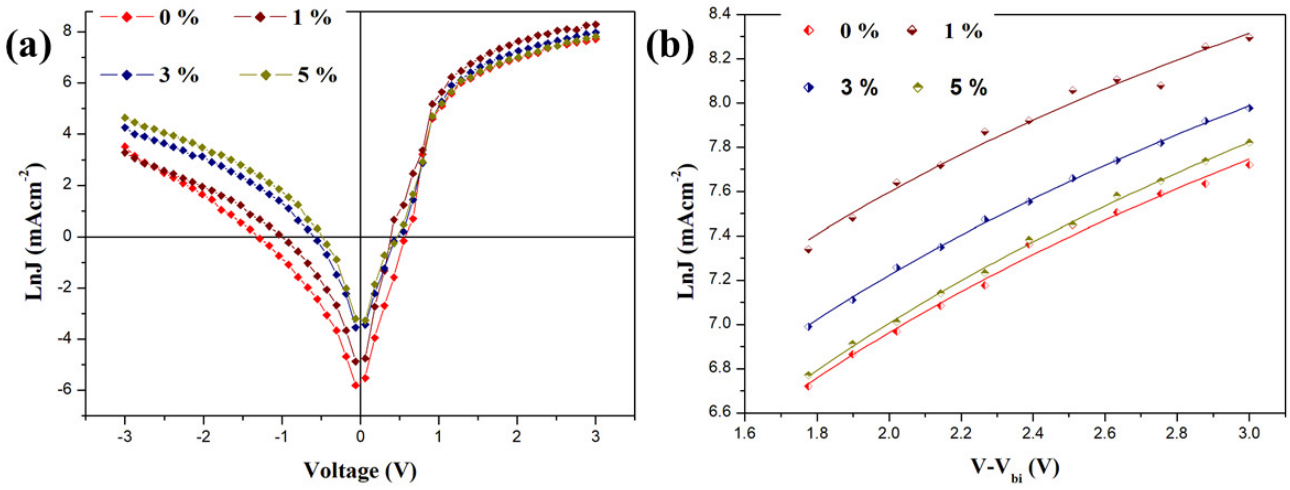

Figure 6.6: (a) J-V characteristic curve measured under dark condition at different concentrations, and (b)The space charge limited current (SCLC) of the fabricated devices with/without CoS NPs.

Charge transport properties

The current-voltage characteristics of TFOSC measured without illumination of light were analysed to investigate the charge transport properties in the medium (Figure 6.6). The space charge limited current (SCLC) data were selected and compared to Mott-Gurney model [66] to derive the necessary charge transport parameters as represented in Figure 6.6(b). The SCLC behaviour in this model is

commonly described by using the field-dependent mobility equation given below:

$$J_{SCLC} = \frac{9}{8}\varepsilon\varepsilon_0\mu_0\frac{V^2}{d^3}\exp(0.89\gamma\sqrt{\frac{V}{L}}) \tag{6.2}$$

where ε_0 and ε are the permittivity of free space and the relative dielectric permittivity of the material respectively, L is the thickness of the active layer, γ is the field activation factor, V is the voltage drop across the device, which can be corrected by the built-in voltage where in this experiment V_{bi} = 1.77 V, and lastly μ_0 is the zero-field mobility. According to the results presented in Table 6.3, the recorded zero-field mobility of the solar cell without incorporation of CoS NPs exhibited 5.23×10^{-4} cm^2 S^{-1} V^{-1}. Interestingly, after the incorporation of CoS NPs into the PTB7:$PC_{71}BM$ polymers, the zero-field mobility of the devices were clearly improved as recorded by 1% NPs doped solar cell 1.31×10^{-3} cm^2 S^{-1} V^{-1}, which is one order of magnitude higher than the reference cell followed by 3% at 7.36×10^{-4} cm^2 S^{-1} V^{-1}. The quantum confinement effect could have influenced the carrier mobility of the modified devices, since the reduced dimension changes the scattering mechanism and effective masses of carriers. However, at dopant concentration of 5%, the zero-field mobility was slightly decreased to 4.68×10^{-4} cm^2 S^{-1} V^{-1} suggesting that the higher concentrations of CoS NPs have a negative impact on the mobility of charges. This is in agreement with the measured series resistances provided in Table 6.2. Furthermore, it's worth mentioning that, the higher zero-field mobility values always correlates to better charge transport medium with improved collection of photo-current. It is noteworthy to mention that the magnitude of dark currents in forward bias as shown in Figure 6.6(a) indicates improved conductivities for all the modified devices and good quality of contact between the active layer and electrodes. The drop in the mobility value of 5% device is also evident in its large reverse bias current apparently due imperfection at high NPs concentration. Consequently, PCE of solar cells containing a 5% of CoS NPs dropped to 4.64% indicating the sensitivity of charge mobility to the high concentrations of CoS NPs in the photo-active layer. On the other hand, the values of the field activation factor (γ) given in Table 6.3, provides insight about the correlation between charge separation and built-in potential in the solar cell. It is a measure of the effectiveness of the in-built potential required to separate charges in the medium. A low γ value suggest higher mobility of photo-generated currents indicating the low non-geminate charge recombination and energy losses within the device.

Thus, the measured low field activation factor at an optimum doping (1 wt%) level is in very good agreement with the recorded high mobility leading to superior device performance. The remaining γ values presented in Table 3 are higher than 1 wt%, and resulted in lower device performances. The observed correlation between μ_0 and γ highlight the positive influence of CoS NPs on the charge transport process, ultimately enhancing the PCE of the solar cells. Generally, the increased charge

Table 6.3: The charge transport parameters for solar cells fabricated at different concentration levels of CoS NPs.

CoS NPs(wt%)	μ_0**(cm^{2}S^{-1}**V^{-1}**)**	γ**(cmV^{-1})**
0	5.23×10^{-4}	-5.41×10^{-5}
1	1.31×10^{-3}	-1.36×10^{-4}
3	7.36×10^{-4}	-6.63×10^{-5}
5	4.68×10^{-4}	-4.85×10^{-5}

transport process observed in devices containing CoS NPs may be attributed to the presence of CoS nano-cages, size effects and multiple carrier generation. As indicated earlier, the nano-cages improve molecular domains connectivity and create more continuous pathways for charge transport by enhancing crystallinity, molecular packing, and surface area of the film [52]. Moreover, the improvement could also be traced to the enhanced molecular packing order at the 0-1 vibronic transition (see Fig. 2c) for the polymer blend films containing CoS NPs compared to the pure PTB7 film. In addition, the quantum confinement effect of CoS could have enhanced the probability of impact ionisation that leads to multiple carrier generation and increase in carrier mobility. The preliminary investigation on the stability of the devices suggest that solar cells with optimum concentrations of CoS appears to have more stable than undoped device (see Table 2). According to test for 24 hours shelf time devices with CoS NPs (1% and 3%) exhibited better stability in PCE compared to the pristine device.

6.4 Conclusion

In summary, CoS NPs have been synthesized and effectively integrated into the solar absorber layer of solution-processed thin film organic solar cells. The experimental results highlight a substantial enhancement in the performance of the solar cells containing CoS NPs within the PTB7:$PC_{71}BM$ active layer of the devices. This improvement in device performance is linked to enhanced optical absorption and efficient charge generation and dissociation as confirmed by optical measurements. The maximum PCE achieved in this study is 6.20% at a concentration of 1% NPs by weight, representing a significant improvement compared to the reference cell. This is an encouraging result and can be further maximized if the experiments procedures are carried out in nitrogen environment. The use of CoS NPs is compatible with roll-to-roll solar cell fabrication, marking a crucial advancement in mass production and cost-effective device manufacturing.

References

[1] Kim G. W., Lee G. Y., Moon B. J., Kim H. I., Park T. Composition tuning of a mixture of thienothiophene-based polymer (PTB7) and PC70BM using a novel additive, tetrabromothiophene (Br-ADD). *Organic Electronics*, 2014, **15**(11), 3268-3273.

[2] Kietzke T. Recent advances in organic solar cells. *Advances in OptoElectronics*, 2007.

[3] Gregg B. A., Hanna M. C. Comparing organic to inorganic photovoltaic cells: Theory, experiment, and simulation. *Journal of Applied Physics*, 2003, **93**(6), 3605-3614.

[4] Mola G. T., Mthethwa M. C., Hamed M. S., Adedeji M. A., Mbuyise X. G., Kumar A., Sharma G., Zang Y. Local surface plasmon resonance assisted energy harvesting in thin film organic solar cells. *Journal of Alloys and Compounds*, 2021, **856**, 158172.

[5] Cheng Y. J., Yang S. H., Hsu C. S. Synthesis of conjugated polymers for organic solar cell applications. *Chemical Reviews*, 2009, **109**(11), 5868-5923.

[6] Im M. J., Son S. Y., Moon B. J., Lee G. Y., Kim J. H., Park T. Improved photovoltaic performance by enhanced crystallinity of poly (3-hexyl) thiophene. *Organic Electronics*, 2013, **14**(11), 3046-3051.

[7] Apaydın D. H., Yıldız D. E., Cirpan A., Toppare L. Optimizing the organic solar cell efficiency: role of the active layer thickness. *Solar Energy Materials and Solar Cells*, 2013, **113**, 100-105.

[8] Namkoong G., Kong J., Samson M., Hwang I. W., Lee K. Active layer thickness effect on the recombination process of PCDTBT: PC71BM organic solar cells. *Organic Electronics*, 2013, **14**(1), 74-79.

[9] Rafique S., Abdullah S. M., Sulaiman K., Iwamoto M. Fundamentals of bulk heterojunction organic solar cells: An overview of stability/degradation issues and strategies for improvement. *Renewable and Sustainable Energy Reviews*, 2018, **84**, 43-53.

[10] Qiao Q. ed. Organic solar cells: materials, devices, interfaces, and modeling. CRC Press, 2017.

[11] Ko D. H., Tumbleston J. R., Zhang L., Williams S., DeSimone J. M., Lopez R., Samulski E. T. Photonic crystal geometry for organic solar cells. *Nano Letters*, 2009, **9**(7), 2742-2746.

[12] Kim J. Y., Kim S. H., Lee H. H., Lee K., Ma W., Gong X., Heeger A. J. New architecture for high-efficiency polymer photovoltaic cells using solution-based titanium oxide as an optical spacer. *Advanced Materials*, 2006, **18**(5), 572-576.

[13] Cocoyer C., Rocha L., Sicot L., Geffroy B., De Bettignies R., Sentein C., Fiorini-Debuisschert C., Raimond P. Implementation of submicrometric periodic surface structures toward improvement of organic-solar-cell performances. *Applied Physics Letters*, 2006, **88**(13).

[14] Fan Z., Wang D., Yuan Y., Wang Y., Cheng Z., Liu Y., Xie Z. A lightweight and conductive MXene/graphene hybrid foam for superior electromagnetic interference shielding. *Chemical Engineering Journal*, 2020, **381**, 122696.

[15] Hamed M. S., Oseni S. O., Kumar A., Sharma G., Mola G. T. Nickel sulphide nanocomposite assisted hole transport in thin film polymer solar cells. *Solar Energy*, 2020, **195**, 310-317.

[16] Cardozo O., Farooq S., Farias P. M., Fraidenraich N., Stingl A., Araujo R. E. D. Zinc oxide nanodiffusers to enhance P3HT: PCBM organic solar cells performance. *Journal of Materials Science: Materials in Electronics*, 2022, **33**(6), 3225-3236.

[17] Gollu S. R., Sharma R., Srinivas G., Kundu S., Gupta D. Effects of incorporation of copper sulfide nanocrystals on the performance of P3HT: PCBM based inverted solar cells. *Organic Electronics*, 2014, **15**(10), 2518-2525.

[18] Ashagre S., Ogundele A. K., Ike J. N., Gebremichael B., Bekele M., Sharma G. D., Mola G. T. Synergistic contribution of potassium sulfide doped with silver nanoparticles on the performance of thin film organic solar cells. *Journal of Physics and Chemistry of Solids*, 2023, **177**, 111290.

[19] Yadav S., Shrivas K., Bajpai P. K. Role of precursors in controlling the size, shape and morphology in the synthesis of copper sulfide nanoparticles and their application for fluorescence detection. *Journal of Alloys and Compounds*, 2019, **772**, 579-592.

[20] Akhatova Z. Z., Alekseev A. M., Aimukhanov A. K., Zeinidenov A. K., Zhakanova A.

M., Ilyassov B. R. Enhanced performance of organic solar cells through incorporation of MoS2 nanoparticles in bulk heterojunction layer. *Physica B: Condensed Matter*, 2023, **668**, 415252.

[21] Li W., Yan X., Xu W. L., Long J., Aberle A. G., Venkataraj S. Efficiency improvement of CIGS solar cells by a modified rear contact. *Solar Energy*, 2017, **157**, 486-495.

[22] Khalate S. A., Kate R. S., Deokate R. J. A review on energy economics and the recent research and development in energy and the Cu2ZnSnS4 (CZTS) solar cells: A focus towards efficiency. *Solar Energy*, 2018, **169**, 616-633.

[23] Manivannan R., Victoria S. N. Preparation of chalcogenide thin films using electrodeposition method for solar cell applications–A review. *Solar Energy*, 2018, **173**, 1144-1157.

[24] Lin Y., Shao Y., Dai J., Li T., Liu Y., Dai X., Xiao X., Deng Y., Gruverman A., Zeng X. C., Huang J. Metallic surface doping of metal halide perovskites. *Nature Communications*, 2021, **12**(1), 7.

[25] Khalil M. I., Atici O., Lucotti A., Binetti S., Le Donne A., Magagnin L. CZTS absorber layer for thin film solar cells from electrodeposited metallic stacked precursors (Zn/Cu-Sn). *Applied Surface Science*, 2016, **379**, 91-97.

[26] Chibueze T. C., Okoye C. M. I. First principles study of the structural, electronic and magnetic properties of w-CoS. *Physica B: Condensed Matter*, 2019, **554**, 165-172.

[27] Chen H. Q., Hao J. G., Wei Y., Huang W. Y., Zhang J. L., Deng T., Yang K., Lu K. Q. Recent developments and perspectives of cobalt sulfide-based composite materials in photocatalysis. *Catalysts*, 2023, **13**(3), 544.

[28] Yang J., Wang Q., Xing T., Wang X., Li G., Shang Z., Wu J., Chen W., Ou T. Engineered exosome-mediated cobalt sulfide quantum dot targeted delivery for photothermal and chemodynamic anticancer therapy. *Journal of Drug Delivery Science and Technology*, 2023, **83**, 104441.

[29] Sibokoza S. B., Moloto M. J., Moloto N., Sibiya P. N. The effect of temperature and precursor concentration on the synthesis of cobalt sulphide nanoparticles using cobalt diethyldithiocarbamate complex. *Chalcogenide Letters*, 2017, **14**(2).

[30] Zampetti A., De Rossi F., Brunetti F., Reale A., Di Carlo A., Brown T. M. Electrodeposited cobalt sulfide hole collecting layer for polymer solar cells. *Applied Physics Letters*, 2014, **105**(6).

[31] Hamed M. S. G., Mola G. T. Copper sulphide as a mechanism to improve energy harvesting in thin film solar cells. *Journal of Alloys and Compounds*, 2019, **802**, 252-258.

[32] Srinivasan M. V., Tsuda N., Shin P. K., Ochiai S. Performance evaluation of PTB7: PC71BM based organic solar cells fabricated by spray coating method using chlorine free solvent. *RSC Advances*, 2015, **5**(69), 56262-56269.

[33] Nair A. T., Anoop C. S., Vinod G. A., Reddy V. S. Efficiency enhancement in polymer solar cells using combined plasmonic effects of multi-positional silver nanostructures. *Organic Electronics*, 2020, **86**, 105872.

[34] Ogundele A. K., Mola G. T. Ternary atoms alloy quantum dot assisted hole transport in thin film polymer solar cells. *Journal of Physics and Chemistry of Solids*, 2022, **171**, 110999.

[35] Hamed M. S., Mola G. T. Highly stable thin film organic solar cells using polycrystallized silver doped LaPO4. *Solar Energy*, 2020, **207**, 157-164.

[36] Ike J. N., Jili N., Kumar A., Sharma G., Mola G. T. The impact of Ag/Co nanocomposite on organic charge transport medium for improved photocurrent in polymer solar cell. *Journal of Polymer Science* (in press).

[37] Dlamini M. W., Hamed M. S., Mbuyise X. G., Mola G. T. Improved energy harvesting using well-aligned ZnS nanoparticles in bulk-heterojunction organic solar cell. *Journal of Materials Science: Materials in Electronics*, 2020, **31**, 9415-9422.

[38] Adedeji M. A., Hamed M. S., Mola G. T. Light trapping using copper decorated nanocomposite in the hole transport layer of organic solar cell. *Solar Energy*, 2020, **203**, 83-90.

[39] Hamed M. S., Ike J. N., Mola G. T. Plasmonic nano-particles mediated energy harvesting in thin-film organic solar cells. *Journal of Physics D: Applied Physics*, 2021, **55**(1), 015102.

[40] Ng A., Yiu W. K., Foo Y., Shen Q., Bejaoui A., Zhao Y., Gokkaya H. C., Djurisic A. B., Zapien J. A., Chan W. K., Surya C. Enhanced performance of PTB7: PC71BM solar cells via different morphologies of gold nanoparticles. *ACS Applied Materials and Interfaces*, 2014, **6**(23), 20676-20684.

[41] Xu M., Yan L., Zhu Y., Li Y., Song X., Yin L. Polydopamine-coated gold nanoparticles used as modifier of the electron transport layer for PTB7: PC71BM polymer solar cells. *Journal of Materials Science: Materials in Electronics*, 2020, **31**, 6698-6705.

[42] Mahajan P., Singh A., Datt R., Gupta V., Arya S. Realization of inverted organic solar cells by using sol-gel synthesized ZnO/Y2O3 core/shell nanoparticles as electron transport

layer. *IEEE Journal of Photovoltaics*, 2020, **10**(6), 1744-1749.

[43] Liu S., Jiang R., You P., Zhu X., Wang J., Yan F. Au/Ag core-shell nanocuboids for high-efficiency organic solar cells with broadband plasmonic enhancement. *Energy and Environmental Science*, 2016, **9**(3), 898-905.

[44] Su X., Hu R., Wen G., Zou X., Qing M., Peng J., He X., Zhang W. Understanding of photophysical processes in DIO additive-treated PTB7: PC71BM solar cells. *Crystals*, 2021, **11**(9), 1139.

[45] Fatima B., David D., Jean-Jacques S., Ludovic E. Study of optical properties and molecular aggregation of conjugated low band gap copolymers: PTB7 and PTB7-Th. (No journal information provided)

[46] Sharma N., Gupta S. K., Negi C. M. S. New insights into the impact of graphene oxide incorporation on molecular ordering and photophysical properties of PTB7: C70 blends. *Journal of Materials Science: Materials in Electronics*, 2020, **31**(24), 22274-22283.

[47] Oseni S. O., Mola G. T. Bimetallic nanocomposites and the performance of inverted organic solar cell. *Composites Part B: Engineering*, 2019, **172**, 660-665.

[48] Huang C., Yu H., Chen J., Zhang J., Wu Z., Hou C. Improved performance of polymer solar cells by doping with Bi2O2S nanocrystals. *Solar Energy Materials and Solar Cells*, 2019, **200**, 110030.

[49] Cui X., Xie Z., Wang Y. Novel CoS2 embedded carbon nanocages by direct sulfurizing metal–organic frameworks for dye-sensitized solar cells. *Nanoscale*, 2016, **8**(23), 11984-11992.

[50] Pandey A., Yadav P., Biswal R., Fahad A., Khan B., Kumar P., Singh M. K. Structural, morphological and electrical properties of hydrothermally synthesized cobalt disulfide (CoS2) nanoparticles. *Ferroelectrics*, 2024, **618**(2), 451-463.

[51] Gao R., Zhang Q., Soyekwo F., Lin C., Lv R., Qu Y., Chen M., Zhu A., Liu Q. Novel amorphous nickel sulfide@ CoS double-shelled polyhedral nanocages for supercapacitor electrode materials with superior electrochemical properties. *Electrochimica Acta*, 2017, **237**, 94-101.

[52] Niu Y., Qian X., Zhang J., Wu W., Liu H., Xu C., Hou L. Stepwise synthesis of CoS2–C@ CoS2 yolk–shell nanocages with much enhanced electrocatalytic performances both in solar cells and hydrogen evolution reactions. *Journal of Materials Chemistry A*, 2018, **6**(25), 12056-12065.

[53] Kushwaha V., Mondal R., Mandal K. D., Singh P., Gupta A. H2S Mediated One-Pot Synthesis of Single Phase Hexagonal CoS Nano-Spheres: A Pseudocapacitive Electrode for Hybrid Supercapacitors. *ChemistrySelect*, 2023, **8**(34), e202301349.

[54] Guo Y., Shang C., Wang E. An efficient CoS2/CoSe2 hybrid catalyst for electrocatalytic hydrogen evolution. *Journal of Materials Chemistry A*, 2017, **5**(6), 2504-2507.

[55] Voigt D., Sarpong L., Bredol M. Tuning the optical band gap of semiconductor nanocomposites—a case study with ZnS/carbon. *Materials*, 2020, **13**(18), 4162.

[56] Manchwari S., Khatter J., Chauhan R. P. Modifications in structural, morphological and optical properties of TiO2 nanoparticles: effect of pH. *Chemical Papers*, 2022, **76**(12), 7545-7551.

[57] Kristl M., Dojer B., Gyergyek S., Kristl J. Synthesis of nickel and cobalt sulfide nanoparticles using a low cost sonochemical method. *Heliyon*, 2017, **3**(3).

[58] Vijayakumar E., Subramania A., Fei Z., Dyson P. J. High-performance dye-sensitized solar cell based on an electrospun poly (vinylidene fluoride-co-hexafluoropropylene)/cobalt sulfide nanocomposite membrane electrolyte. *RSC Advances*, 2015, **5**(64), 52026-52032.

[59] He H. Y. Efficient interface-induced effect of novel reduced graphene oxide-CoS heteronanostructures in enhancing photocatalytic activities. *Applied Surface Science*, 2017, **421**, 260-267.

[60] Abza T., Dadi D. G., Hone F. G., Meharu T. C., Tekle G., Abebe E. B., Ahmed K. S. Characterization of cobalt sulfide thin films synthesized from acidic chemical baths. *Advances in Materials Science and Engineering*, 2020, **2020**(1), 2628706.

[61] Rani P., Alegaonkar A. P., Alegaonkar P. S., Saka A. Evaluation of electrochemical performance of cobalt sulphide on various current collectors. *Material Science Research India (Online)*, 2022, **19**(3), 134-141.

[62] Martínez-Otero A., Liu Q., Mantilla-Perez P., Bajo M. M., Martorell J. An extremely thin and robust interconnecting layer providing 76% fill factor in a tandem polymer solar cell architecture. *Journal of Materials Chemistry A*, 2015, **3**(20), 10681-10686.

[63] To C. H., Ng A., Dong Q., Djurisic A. B., Zapien J. A., Chan W. K., Surya C. Effect of PTB7 properties on the performance of PTB7: PC71BM solar cells. *ACS Applied Materials & Interfaces*, 2015, **7**(24), 13198-13207.

[64] Collins B. A., Li Z., Tumbleston J. R., Gann E., McNeill C. R., Ade H. Absolute measure-

ment of domain composition and nanoscale size distribution explains performance in PTB7: PC71BM solar cells. *Advanced Energy Materials*, 2013, **3**(1), 65-74.

[65] Oseni S. O., Mola G. T. The effect of uni-and binary solvent additives in PTB7:PC61BM based solar cells. *Solar Energy*, 2017, **150**, 66-72.

[66] Hamed M. S., Ahmed A. Y., Mola G. T. Suppressing charge recombination in disordered polymers blend medium. *Journal of Physics D: Applied Physics*, 2023, **56**(40), 405101.

Chapter 7

Conclusion

7.1 Summary of The Thesis

The thesis has explored the incorporation of plasmonic metals and metal sulfide NPs into the active layers of polymer thin-film solar cells to enhance their performance. The study investigated the introduction of plasmonic NPs with different compositions and morphologies such as including Ag:Mg bimetallic BMNPs, and Ni/Ag NCs into the P3HT: $PC_{61}BM$ blend. The investigations also studied about the integration of CoS quantum dot into the PTB7:$PC_{71}BM$ polymer active layer blend. The collected results showed some significant improvements in light absorption, charge transport, and PCE of thin film solar cells. Moreover, the observed enhancements in the NPs Incorporated into P3HT: $PC_{61}BM$ were associated with the localized surface plasmon resonance (LSPR) effect as a major factor in increasing light harvesting, improving exciton dissociation, and facilitating charge transport processes. For example, Ag:Mg BMNPs increased the PCE by 79% compared to the un-doped device, with the maximum PCE reaching 4.11% at the optimized 1.5 wt% doping level. Similarly, the Ni/Ag NCs recorded the highest enhancement among the plasmonic materials, increasing the PCE by 144%, reaching 6.20% at a 2 wt% concentration ratio. The enhancement in performance through all plasmonic NPs combined devices originated from the attribution of the LSPR effect, which supported better photon absorption and minimized charge recombination losses. On the other hand, by integrating CoS NPs into the PTB7:$PC_{71}BM$ active layer thin film solar cells, the quantum confinement effect was utilized. The role of the quantum confinement effect resulted in enhanced optical absorption and all the device's parameters. The improvement resulted in a 37% PCE enhancement compared to the pristine device, with the maximum efficiency recorded at 6.20% for a 1 wt% concentration of CoS NPs. The experimental outcomes highlight that CoS NPs not only improved the optoelectronic properties of the active layer but also compatible with large-scale, cost-effective manufacturing processes. Generally, the thesis studied

the effect of plasmonic metals and metal sulfide NPs to improve the performance of polymer thin film solar cells. The experimental results demonstrate the impact of the LSPR effect of plasmonic NPs and the quantum confinement effect of metal-sulfide NPs can lead to significant advancements in solar cell efficiency. Our investigations open new areas for further research such as optimizing NP concentrations, synthesis techniques, and exploring their application in different solar cell architectures. The outcomes of this research highlight the potential of these NPs to advance the efficiency and development of organic thin-film solar technologies.

7.2 Future Outlook

By the rational selection of their bulk materials besides finely tuning the morphology and interfaces, the future work focuses on combining the highly promising plasmonic NPs with quantum dots (QDs) in polymer thin films solar cells. The combined NPs are expected to demonstrate great performance in the PTB7 blend and also in high-performance non-fullerene acceptors such as PM6:Y6. This strategy would be achieved by optimizing the Interfaces and Morphology of NPs including:

A. The synthesis of NPs will focus on controlling their structure and interfacial properties to prevent aggregation and enhance uniform distribution within the polymer matrix. Additionally, the morphology and geometrical aspect ratios of these NPs will be correlated with theoretical modeling of their scattering and absorption cross-sections. Furthermore, the stoichiometry of bimetallic layers plays a critical role in tuning the plasmonic resonance effect by modifying the dielectric function, charge distribution, and coupling between different metallic components, thereby influencing resonance wavelength and field enhancement.

B. This controlled morphology will also reduce energy losses during charge transfer.

C. The interface control strategies will focus on synthesizing NPs in different designs, such as a core-shell and half-shell (Janus-Type NPs). The Janus or half-coated NPs, where only one side of a plasmonic NP is coated with a quantum dot, leaving the other side exposed to directly interact with the polymer matrix. This allows each one of the NP to directly deliver its associated properties to the thin film.